CRANFIELD UNIVERSITY

CONSTANTINOS FRANCESKIDES

SUBJECT-SPECIFIC FUNCTIONAL MODEL OF HARD AND SOFT TISSUES; SKULL AND SPINE

CRANFIELD DEFENCE AND SECURITY
CRANFIELD FORENSIC INSTITUTE

PhD
Academic Year: 2014 - 2018

Supervisor: PROF. P. ZIOUPOS
Associate Supervisor: DR. M. C. GIBSON
JULY 2018

CRANFIELD UNIVERSITY

CRANFIELD DEFENCE AND SECURITY
CRANFIELD FORENSIC INSTITUTE

PhD

Academic Year 2014 - 2018

CONSTANTINOS FRANCESKIDES

SUBJECT-SPECIFIC FUNCTIONAL MODEL OF HARD AND SOFT TISSUES; SKULL AND SPINE

Supervisor: PROF. P ZIOUPOS
Associate Supervisor: DR. M. C. GIBSON
JULY 2018

This thesis is submitted in partial fulfilment of the requirements for the degree of PhD

ABSTRACT

There is a strong demand for mechanically and morphologically accurate models of the human musculoskeletal system, particularly of the spine. Such models would have multiple applications, including surgical guides, the analysis of implant fitment and design, as well as individual strength evaluation.

Current standards such as the ASTM F1717 (devised for the static and dynamic testing of implants) represent complex spine morphologies using simplified blocks of homogeneous material generally constructed from ultra-high-molecular-weight polyethylene (UHMWPE). These do not attempt to replicate morphological characteristics, and therefore do not reproduce mechanical loading properties, especially when considering the complexity of vertebral bodies and their facets.

The work described in this thesis investigated the creation of a compressively accurate and validated model of a lumbar motion segment, specifically the validity of technologies such as computed tomography (CT) scanning, computer-aided scan reconstruction, rapid prototyping, digital image correlation (DIC) and finite element analysis (FEA) modelling. In particular, DIC (an optical measurement method) allowed full-field measurements of the displacements and strains. This was used to determine loading paths and magnitudes during the testing procedure. To complement this approach, FEA modelling identified the location and severity of maximum strains for subsequent comparison to the DIC and mechanical testing data. All FEA models were based on CT scan datasets of the modelled cadaveric material, and were validated against the *ex vivo* mechanical test measurements. The research followed a number of core stages:

1. First, the applicable technologies were tested and verified, with all channels indicating closely related data. This was achieved by the compressive loading of two types of analogue skulls, allowing the validation of DIC as a data acquisition technique in complex structures. Validation against FEA models demonstrated their potential to provide further insight into the experimental results. The initial testing identified a well-defined pathway for a sample manufacturing and preparation process, making it much easier to produce reliable analogues for subsequent experiments.

2. In the second stage, analogue motion segments (AMss) were created using the CT scan datasets obtained from the cadaveric porcine specimens. Motion analysis provided a better understanding of the loading paths again by using DIC as an appropriate data acquisition system. Following the creation of the AMS, different materials were considered for the creation of intervertebral discs (IVDs). The mechanically most biofidelic material was selected.
3. Finally, a sensitivity study was carried out to determine a relationship between the scanning resolution and model accuracy for both the mechanical analogue and the FEA model.

The use of 3D printing was found to be an effective, efficient and economical strategy for the creation of accurate biomechanical analogues. Furthermore, DIC was a useful tool when looking at individual component strains and displacements. Finally, when considering a motion segment, the majority of the elastic loading – and thus its behaviour on the whole – was governed by the material properties of the IVD simulant.

This research demonstrated a clear path towards the creation of a reliable, biofidelic motion segment, or even a partial lumbar spine analogue, that would comply in dynamic and static loading scenarios as well as conformity in compression. The capability of the techniques and the compliance and accuracy of the resulting models was confirmed by developing both analogue mechanical models and FE simulations. Given their potential advantages, it is only a matter of time before mechanical analogues and their corresponding digital models replace the outdated and inaccurate testing standards in our current medical facilities and research centres.

Keywords: *Biomechanics, micro-computed tomography, 3D printing, rapid prototyping, skull impact, spine analogue, digital image correlation, finite element analysis*

ACKNOWLEDGEMENTS

Like many studies of this nature, acknowledgments are due not just to the immediate family of the author, but also to numerous other individuals who have helped shape and form the work to its final stage.

To this extent, I would like to thank Professor Peter Zioupos, who has thrown me in at the deep end yet assisted me in times of dire need, as well as Mr. Karl Norris and all the members of staff at the Cranfield University workshops for allowing me to use their 3D printing facilities. Further thanks are due to Professor Ian Horsfall and Dr. Gianluca Tozzi, who guided me through the non-trivial world of impact testing and digital image correlation. My navigational compass during the FEA modelling work was the late Dr. Michael Gibson, my assisting supervisor but also a dear friend, now sorely missed. He piloted me through the intricate workings of complex computational systems with unfailing resolve.

I would also like to thank Sebastian Wirth, a friend and a fellow PhD candidate, and Emily Arnold, Tobias-Akash Shanker and Adams George, who all stood next to me during my studies. In addition, data collection would have been impossible without the generosity of Mr. Jolyon Cleaves of Amatek UK, and for that I would like to express my gratitude.

Throughout my research I have attended conferences hosted by the Computational Methods in Biomechanics and Biomedical Engineering (CMBBE), European Society of Biomechanics (ESB), and Survival and Flight Equipment Association (SAFE), which provided me with the opportunity to present my findings, discover the latest work in the field, and discus ideas with the leaders. This would not have been possible without funding from the Cranfield Students Association, the ESB travel grant, and funding from the Institute of Engineering and Physics in Medicine.

Of course, I want to thank my parents for supporting me in more ways than one, and for always encouraging me to push myself.

Lastly, I would like to thank my son and wife, Orestis and Foula, as well as my dog, Hera, who have put up with and supported me throughout this Odyssey. This is for them.

CONFERENCE PRESENTATIONS – Main Author

1. Franceskides C[ǂ*^], Shanker T, Gibson M, Clasper J & Zioupos P (2015)
   Input optimisation for FEA of trabecular bone anisotropy in human thoracic-lumbar vertebrae.
   13th International Symposium on Computer Methods in Biomechanics and Biomedical Engineering (CMBBE), Montreal, Canada, 01-05 September 2015

2. Franceskides C[ǂ*^], Leger T, Horsfall I, Shanker T, Adams GJ , Clasper J & Zioupos P (2016) Evaluation of bone excision on occipital area of simulated human skull.
   22nd Congress of the European Society of Biomechanics (ESB2016), Lyon, France, 10-13 July 2016.

3. Franceskides C[ǂ*^], Arnold E, Horsfall I, Clasper J, Tozzi G & Zioupos P (2017)
   3D printing, the future of cost effective biomechanical testing.
   25th SAFE Europe Symposium 2017, Amsterdam, 03-06 April 2017.

4. Franceskides C[ǂ*^], Arnold E, Horsfall I, Tozzi G & Zioupos P (2017)
   A subject-specific analogue model for spinal motion segments.
   23rd Congress of the European Society of Biomechanics, Seville, Spain, 02-05 July 2017.

5. Franceskides C[ǂ*^], Arnold E, Horsfall I, Clasper J, Tozzi G & Zioupos P (2017)
   3D printing, the future of cost effective biomechanical testing.
   55th SAFE International Symposium 2017, Florida USA, 31-02 November 2017.

6. Franceskides C[ǂ], Michael Gibson, Peter Zioupos[*^] (2018)
   Evaluation of bone excision effects on a human skull model – mechanical tests and FEA.
   5th SIMBIO-M Conference 2018, Stratford-Upon-Avon, UK, 18-19 June 2018

[*] - Submitting author
ǂ - Lead author
[^] - Presenting author

CONFERENCE PRESENTATIONS – Associated Author

1. Shanker T[ǂ*^], Franceskides C, Gibson M, Clasper J, Adams G & Zioupos P (2015)
   Effects of µCT and FE resolution in expressing anisotropic properties in vertebral cancellous bone.

   13th International Symposium on Computer Methods in Biomechanics and Biomedical Engineering (CMBBE), Montreal, Canada, 01-05 September 2015

2. Gibson M[ǂ*], Franceskides C, Shanker T[^], & Zioupos P (2016)
   Simulated impact response of a 3-D printed skull, with an ellipsoidal excision, using finite element analysis.

   22nd Congress of the European Society of Biomechanics (ESB2016), Lyon, France, 10-13 July 2016.

3. Wood D[ǂ*], Appleby-Thomas G, Fitzmaurice B, Franceskides C, Shanker T[^], Zioupos P & Samra A (2016)
   On the shock behaviour and response of *Ovis Aries* vertebrae.

   22nd Congress of the European Society of Biomechanics (ESB2016), Lyon, France, 10-13 July 2016.

4. Shanker T[ǂ*^], Franceskides C, Gibson M, Clasper J, Adams G & Zioupos P (2016)
   Effects of µCT and FE resolution in expressing anisotropic properties in vertebral cancellous bone.

   51st UK Conference on Human Responses to Vibration (HRV2016), Gosport, 14 15 September 2016

5. Adams G[ǂ*], Franceskides C[^] & Zioupos P (2017)
   Chemical and structural properties of cancellous bone in relation to its fracture toughness.

   23rd Congress of the European Society of Biomechanics, Seville, Spain, 02-05 July 2017.

[*] - Submitting author
ǂ - Lead author
[^] - Presenting author

JOURNAL SUBMISSIONS/PUBLICATIONS

Title	Status	Journal
EVALUATION OF BONE EXCISION EFFECTS ON A HUMAN SKULL MODEL – I: MECHANICAL TESTING AND DIGITAL IMAGE CORRELATION	03 Aug 2018	Proceedings of the Institution of Mechanical Engineers, Part H: Journal of Engineering in Medicine
EVALUATION OF BONE EXCISION EFFECTS ON A HUMAN SKULL MODEL – II: FINITE ELEMENT ANALYSIS	03 Aug 2018	Proceedings of the Institution of Mechanical Engineers, Part H: Journal of Engineering in Medicine
SPINAL MOTION SEGMENTS: CONCEPT FOR A SUBJECT-SPECIFIC ANALOGUE MODEL	24 Sep 2018	Journal of Bionic Engineering
SPINAL MOTION SEGMENTS: TUNING AND OPTIMISATION OF BIOFIDELIC PERFORMANCE	24 Sep 2018	Journal of Bionic Engineering
MULTISCALE MODELLING AND TESTING OF A PORCINE LUMBAR SPINE MOTION SEGMENT ANALOGUE	Pending Submission	Computer Methods in Biomechanics and Biomedical Engineering Engineers, Part H: Journal of Engineering in Medicine

TABLE OF CONTENTS

LIST OF FIGURES

LIST OF TABLES

LIST OF EQUATIONS

LIST OF ABBREVIATIONS

AF	Annulus fibrosus
ALL	Anterior longitudinal ligament
AMS	Artificial/analogue motion segment
ASM	Analogue spine model
ASTM	American Society for Testing and Materials
BV/TV	Bone volume/tissue volume
CL	Capsular ligament
CT	Computer/computed tomography
CVB	Cadaveric vertebral body
DA	Degree of anisotropy
D_{app}	Apparent density (g/cm^3)
DD	Disc degeneration
DDD	Degenerative disc disease
FDA	Food and Drug Administration
FEA	Finite element analysis
ISL	Interspinous ligament
IVD	Intervertebral disc
k	Stiffness (N/mm)
LBP	Low back pain
LF	Ligamentum flavum
m	Mass (g)
MS	Motion segment
NP	Nucleus pulposus
PLL	Posterior longitudinal ligament
SSL	Supraspinous ligament
TL	Traverse ligament
VB	Vertebral body
WHO	World Health Organization
Y	Young’s modulus, also shown as E (MPa)
ε	Strain (dimensionless)
σ	Stress (MPa)

1 INTRODUCTION

Technology, the application of scientific knowledge for practical purposes, evolves at a dizzying rate. In the last decade, scientists have progressed from using bytes to terabytes, from looking at millimetre to nanometre scales, and from performing calculations using teraflops to petaflops of data.

Although in the examples above there is a commendable rate of progress, some things have not changed. The ability and rate of the human body to evolve is a prime example that comes to mind. Although the human body has not changed dramatically over centuries, the way we analyse and interpret it has, reflecting the technological “boom” described above. The research described in this thesis seeks to make use of this “boom” by bridging different technologies in an effective and efficient way, ultimately to create a morphologically and biomechanically accurate, patient-specific spinal motion segment analogue. The thesis initially provides background information about the spine itself and existing approaches to simulate its elements, and then focuses on experimental and numerical investigations carried out by the author to demonstrate the production of an accurate spinal element analogue by 3D printing with the potential for medical applications.

1.1 Significance

Humans are bipeds, so most of the forces acting on the human skeleton during everyday life pass through the spine, particularly the lumbar region. Low back pain (LBP) is a modern-day epidemic in our mechanised and motorised environment. However, certain sectors and professions are more prone to suffering than others. Military personnel, for example, are frequently exposed to vibration and repeated impacts when in transit through land, sea and air environments during training or in active service. As a result, in recent years, there has been growing interest in understanding and defining the working envelope of the human body, and particularly the spine. A recent review of the US Navy Special Boat Operators noted that injuries to the knees and neck are common, but the most common injury site of all was the lower back (Ensign, et al., 2000). This is consistent with Royal Navy reports citing a 58% incidence of LBP over the last 4 years. These injuries have not only been reported in service personnel but also in civilians (Marine Accident Investigation, 2009).

Current directives and standards fall short of providing a conclusive safe loading window, e.g. EU Directive 2002/44/EC and the international standards ISO 2631 and BSI 1987 (International Organization for Standardization, 1997). An understanding of the human musculoskeletal system is necessary to address this gap in knowledge.

The latest reports from the World Health Organization (WHO) state that LBP is currently the leading cause of work absence and movement limitation globally. The resulting economic burden on individuals, families, communities, industry, governments and health systems needs to be tackled [(Taimela, et al., 1997); (Konstantinou & Dunn, 2008)].

In the United Kingdom, more than 100 million workdays are lost per year due to LBP, and this is historically the most common cause of disability in young adults (Croft, et al., 1993). The aforementioned factors highlight once again the need for more research in a number of areas, not only focusing on biological and biomechanical aspects but also the operational side of this multifaceted problem.

1.2 The spine

1.2.1 Anatomy – an overview

The spinal motion segment has evolved over millions of years into a complex, yet extremely efficient biomechanical structure. To understand why and how it functions, the sub-assemblies need to be broken down. The spine has several integral parts, but for the research described herein, two major components are considered: the vertebrae and discs (when excluding the muscles attached to and surrounding the spine).

The human spine consists of vertebrae that are stacked with interspersed intervertebral discs (IVDs). The 33 vertebrae, although stacked, have distinct shapes and sizes, thus providing different degrees of curvature.

This curvature, when viewed from the side, has a distinct S-shape, but this is only true in the case of an adult, fully-formed spine. There are abnormalities such as lordosis, kyphosis and scoliosis, which all affect the characteristics of this S-shape (Domann, 2011).

1.2.1.1 Overall structure

The spine is the longest and most complex bone array within the musculoskeletal system, and accordingly it serves a multitude of functions. The first and foremost is to provide support from the head to the pelvis, with all the extremities connected through its entire length. These extremities could not function without commands coming from the brain. This is where the spine comes in again as the supporting structure for the "super-highway" of stimuli and commands, i.e. the spinal cord. In addition to this, the spine is the body's central loading 'damper', allowing shocks and load to travel along the length of the spine while providing a dampening response though the IVDs. Finally, it allows movement while restricting excessive motion of the trunk and all the extremities of the body (Özkaya, et al., 2017).

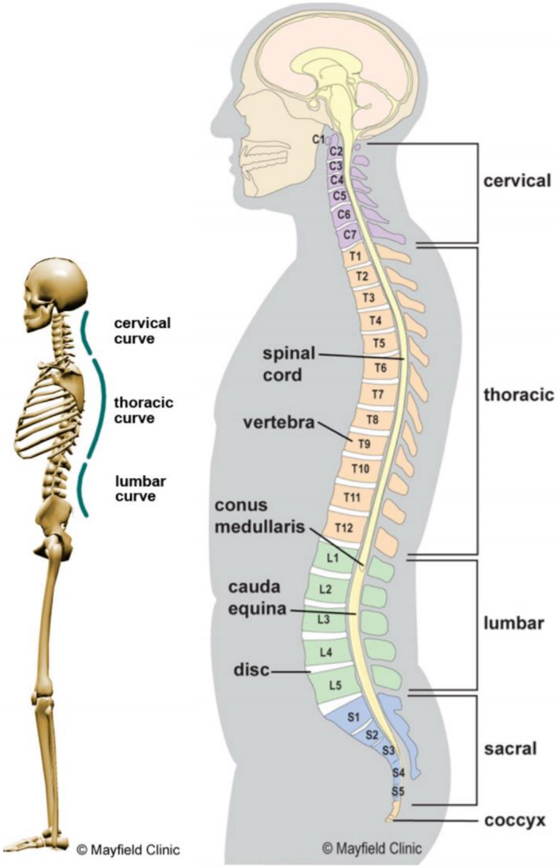

Figure 1-1 The spine, showing the five sections that make up the spinal column: cervical, thoracic, lumbar, sacral and coccyx (Ref. Mayfield Clinic)

As shown Figure 1-1 above, the human spine is considered to comprise five regions: cervical (seven vertebrae), thoracic (twelve vertebrae), lumbar (five vertebrae), sacral (five fused vertebrae) and coccygeal (four fused vertebrae).

In the sagittal plane, the spine has four main curvatures. The cervical and lumbar regions are lordotic (concave), whereas the thoracic and sacral regions are kyphotic (convex). The key features of the morphological vertebral bones are the main body (larger central area), which is the main weight-bearing surface, the arch (middle part of the vertebrae), where a hollow tube is formed for the spinal column, and the star-shaped outriggers that form the facets and the muscle attachment points (Figure 1-2).

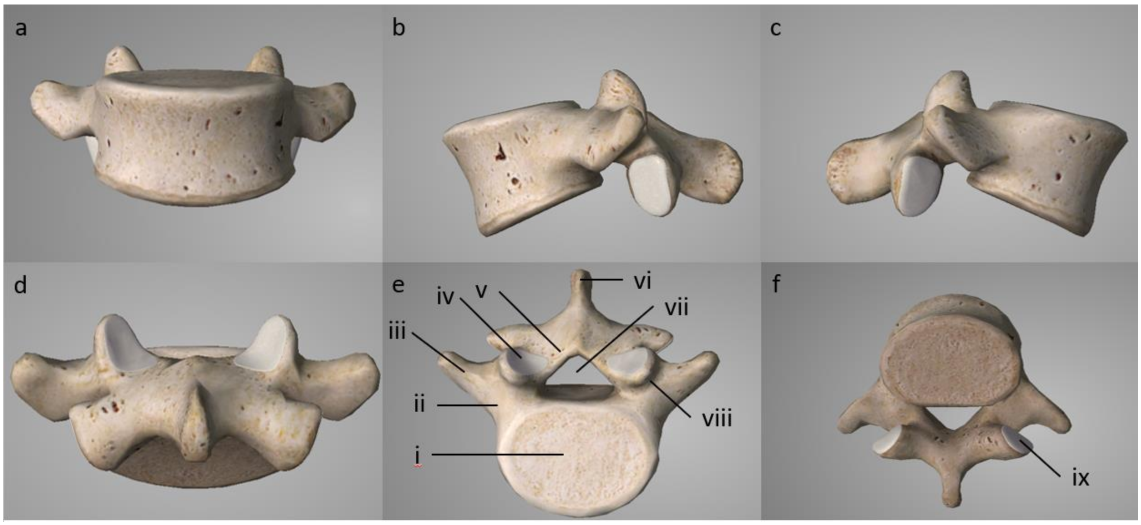

Figure 1-2 A lumbar vertebra. Panels a–f show different views: a. anterior, b. left lateral, c. right lateral, d. posterior, e. superior, f. inferior. Panels i–ix show different anatomical parts: i. vertebral body, ii. pedicle, iii. transverse process, iv. superior articular facet, v. lamina, vi. spinous process, vii. vertebral foramen, viii. superior articular process and ix. inferior articular facet.

Seven processes (bony, arm-like structures) arise from the vertebral arch: the spinous process, two transverse processes, two superior facets, and two inferior facets.

Moving further out towards the extremities of the vertebrae, we observe the facets. These are the joints that allow the flexion/extension of the spine, while retaining the vertical rigidity. Each vertebra has a total of four facets, the superior and inferior facets.

Moving along the vertical axis we come to the IVDs, the soft cushioning between the vertebral bodies, which prevent the vertebrae from making contact with each other (bone–bone contact). The IVDs form a criss-cross weave of fibrous bands. These are attached to both bodies above and below. The disc comprises different materials at each depth, with a fluid core that facilitates the dampening of spinal loading.

Another integral part to the spine is the ligaments, which maintain stiffness and posture. These strong fibrous bands stabilise the system, while protecting the IVDs. The three major ligaments are the anterior longitudinal ligament (ALL), the ligamentum flavum (LF), and posterior longitudinal ligament (PLL). The ALL and PLL are continuous bands that run from the top to the bottom of the spinal column along the vertebral bodies and prevent excessive movement of the bones, whereas the ligamentum flavum attaches the lamina of each vertebra.

Any damage to the spine may affect the spinal cord, resulting in a loss of motion and sensory functions. The cord is ~460 mm long and traverses from the first lumbar vertebra all the way to the brainstem. The upper motor neurons make up the spinal cord itself, whereas the lower motor neurons form nerves branching off the back and neck, exiting through each vertebra. Thirty-one pairs of spinal nerves branch off the spinal cord, each pair associated with a specific area of the body. This allows doctors to diagnose the approximate location of potential spinal problems. This nerve-to-body map is known as the dermatome.

Finally, the spinal cord is protected by three sheaths or layers. These are the same membrane layers as found within the brain (the meninges) and comprise the tough outer dura, the arachnoid, and the pia matter [(Taimela, et al., 1997), (Özkaya, et al., 2017), (Mayfield Clinic, 2018)].

1.2.1.2 Lumbar spine

The lumbar spine is the focus of the work in this thesis due to the elevated loading this area tends to experience (external loading as well as upper, torso loading). As previously stated, the lumbar spine comprises five distinct vertebrae sections and their associated soft tissue ligaments: IVDs, tendons and muscles.

The lumbar spine is easily identified by its lordotic curvature and the relatively large size of the vertebrae (L1–L5). This is an evolutionary adaptation evident in bipeds, because their upright stance requires the lower spine to withstand greater loads and consequently a larger portion of the upper body (Özkaya, et al., 2017). Another unique feature is the facet joint orientations, which transition from superior to inferior vertebrae. This adaptation provides greater resistance to axial rotation but less resistance to extension and translation.

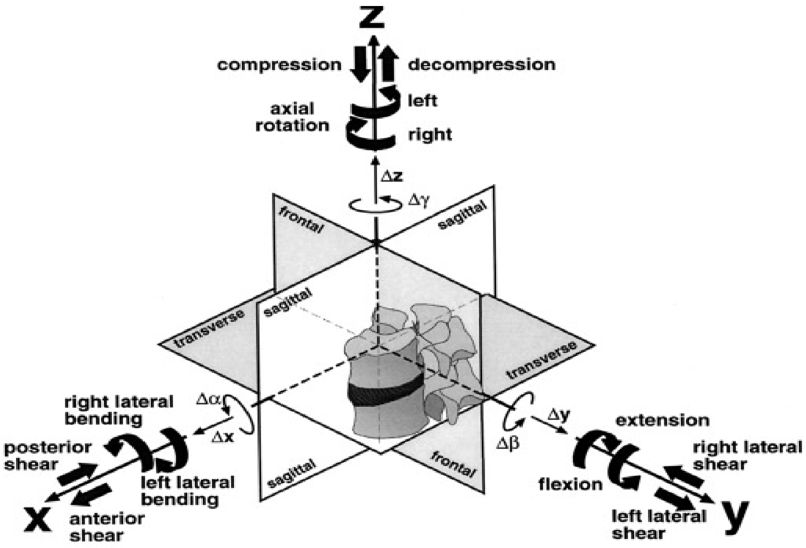

Figure 1-3 Three-dimensional coordinate system of the spine, demonstrating clinically relevant translations and rotations [Ref. (Wilke, et al., 1998)].

The lumbar spine has a wide range of motion, including flexion and extension, lateral bending, and axial rotation. The research in this thesis focuses on uniaxial compression and translation because this is a simple yet solid starting point while limiting any other compound movement of the motion segment. Figure 1-3 above highlights the degrees of motion (DOM) and mobility envelope of the lumbar spine.

In an effort to further deconstruct a spinal motion segment, we have to consider the major subsystems, and as mentioned earlier these are the hard and soft tissues, i.e. the components made of bone and the components made of cartilage, fibrous material, synovial fluid and muscles.

Hard tissue

Due to its volumetric proportion, the main hard tissue body within a spinal motion segment is the vertebral body (VB), which is in turn the main load-bearing surface. Like many other bones, the VB has a sandwich structure predominantly comprising the outer cortical shell (typically ~4 mm thick) and the inner cancellous bone filling the rest of the VB (Silva, et al., 1994).

The VB has top and bottom surfaces known as endplates. These outermost structures form an intermediary surface between the cancellous bone and the IVD. Their thickness is variable, but the mean value is ~5 mm. The endplates hold the disc in place and resist slippage and herniation (Resnick, et al., 1997).

For every VB there is an associated superior and inferior facet which is another connective strand to the vertebral bodies above and below. These facet-joints sandwich a synovial fluid capsule that acts as a frictionless boundary. The connective part from the facets to the VB is the neural arch, which is of great importance because it forms the protective “cage” holding the spinal cord. Finally, the posterior and transverse processes provide the attachment points for ligaments and muscles (Ferguson & Steffen, 2003).

The bone tissue in the spine can also be characterised at different structural levels, specifically the macro, micro and nano levels, as discussed below.

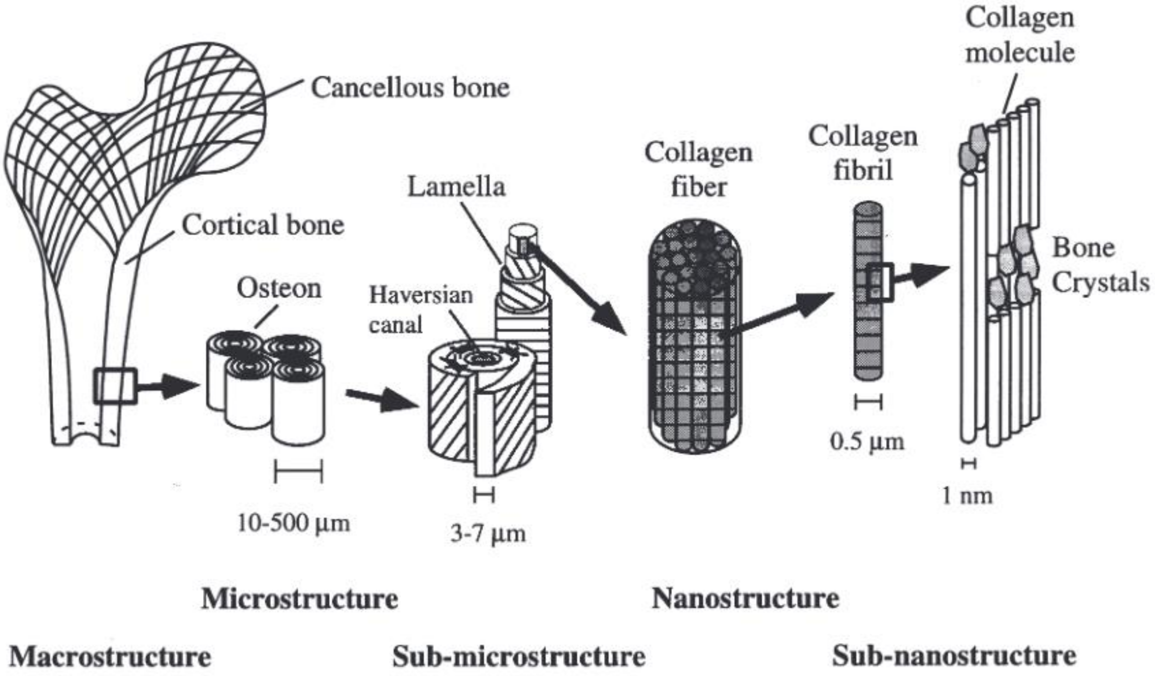

Figure 1-4 Hierarchical structural organisation of bone (J.-Y Rho et al. 1998).

Bone macro-structure

The macro-structure of bone refers to the structural properties that can be discerned with the naked eye, and as discussed above the two discrete forms are the cortical and cancellous bone tissues (Figure 1-4).

Cortical and cancellous bone tissues exist on a porosity spectrum ranging from near 0% to more than 99%, reflecting the bone volume to total tissue volume ratio (BV/TV). This represents the void volume per unit volume of whole bone structure, typically measured at the scale of microns.

Cortical bone tends to have a porosity of less than 15%, which is equivalent to densities of 1.7–2.1 g/cm^3 at the material level, and apparent densities of ~1.8 g/cm^3 (Zioupos, et al., 2008). In comparison, cancellous bone typically has a porosity of greater than 50%. At the transition points, e.g. at the ends of long bones, the bone tissue often has an intermediate porosity.

Bone micro-structure

The micro-structure bone is often described as either primary or secondary, although four types of organisation are apparent: secondary osteons, fibro-lamellar bone, lamellar bone and woven bone (Figure 1-4).

- Secondary osteons are highly-organised secondary bone structures that were formed through remodelling [(Currey, 2002), (Martin & Burr, 1989)].
- Fibro-lamellar bone consists of woven and lamellar bone and is classed as a primary structure.
- Lamellar bone is organised similarly to secondary osteons but can exist both in primary and secondary form.
- Woven bone is primary bone tissues found in young bones, and it displays more isotropic properties than the more mature bone types.

Bone nano-structure

The nano-structure of bone describes the organic rather than the mineralised portion, and it consists of the collagenous and non-collagenous proteins (NCPs). Both groups of proteins play key roles in the overall structure and are necessary for bone strength. The collagen in the bone matrix accounts for 85–90% of the total bone protein and is primarily structural (Knott & Bailey, 1998), whereas the NCPs provide both structural support and oversee the chemical and biological process involved in bone metabolism and formation.

Multiple types of collagen are found in bone, but type I collagen is the most abundant, accompanied by smaller amounts of types III, V and VI al (Knott & Bailey, 1998). In turn, helical structures formed by collagen are called fibrils and are characterised by a 67-nm periodicity and 40-nm gaps between the ends of the molecules, with overlaps of 27 nm (Viquet-Carrin, et al., 2006).

When the collagen matrix undergoes mineralisation in young bone, any abnormality within the structure of the collagen matrix can affect the cross-linking profile, resulting in the irregular deposition of mineral sheets and compromised mechanical properties (Landis, 1995).

The research in this thesis focuses on the macro and micro levels of bone structure, primarily because these are easier to monitor with readily-available imaging techniques. This approach also applies to the manufacturing processes, with an exponential rise in the costs of 3D printing when moving from micro-scale to nano-scale resolution.

Soft tissue

Although there is a singular hard tissue matrix in the lumbar spine, there are several different soft tissues with diverse levels of complexity, functional roles and importance. Consequently, a truly representative model needs to incorporate key facets of these tissues and their contributions to the behaviour and responses of the musculoskeletal system.

Ligaments

There are seven ligaments that influence each motion segment (MS), i.e. the anterior longitudinal ligament (ALL), capsular ligament (CL), inter-spinous ligament (ISL), ligamentum flavum (LF), posterior longitudinal ligament (PLL), supra-spinous ligament (SSL) and transverse ligament (TL).

They each exhibit non-linear behaviour, with a low initial stiffness that increases gradually (Sharma, et al., 1995). These ligaments play a key role in the rigidness and stability of the lumbar spine, and they are by far the most difficult components to recreate as mechanical and *in silico* models. Addressing each in turn:

- The ALL attaches anteriorly to the vertebral surface, meshing with the IVD and margins of the endplates.
- The CL, one of the smallest ligaments, connects the inferior and superior facets of adjacent vertebrae. As the name suggests, it is a capsule of synovial fluid that provides stability during flexion and torsion (Sharma, et al., 1995).
- The ISL attaches to the spinous process but makes only a small contribution to the stability of an adult spine. It is a thin membrane that typically degenerates in a similar manner to the IVD (Rissanen, 1964).
- The LF is the connective ligament between the laminae of adjacent vertebrae. Its broad and thick structure maintains vertebral alignment and it plays a primary role in lateral bending and flexion.
- Like the ALL, the PLL meshes the IVD and the endplate and helps to prevent IVD barrelling (swelling) while providing stiffness in extension. Its predominant role is resistance to flexion and extension and it is embedded within the collagenous fibres of the posterior annulus.
- The SSL is attached to the spinous process and is integral to the structure of the ISL, providing further stability to the VB.
- Finally, the TL is the transverse process connecting adjacent vertebrae, providing torsional rigidity in the lumbar region.

Intervertebral discs

The IVD is an important component of the motion segment because it achieves the almost uniform distribution of load to the tangential endplates (Adams, 2004). Its main function is to provide a dampened, evenly-distributed load while allowing the dissipation and absorption of shocks. The IVD therefore facilitates the mobility of the spine while preventing excessive range of motion (Ferguson & Steffen, 2003). The IVD consists of two distinct parts: the annulus fibrosus (AF) and the nucleus pulposus (NP).

The AF is anisotropic in nature, comprising concentric annular fibres with alternating orientations differing by 30° to the adjacent layers. The NP is a gel-like, amorphous liquid with a high concentration of hydrophilic proteoglycans, enabling it to retain water (Leone, 2007). The NP is enclosed within the AF, and when the hydrostatic pressure increases the pressure is transferred to the walls of the AF causing hoop stress (Figure 1-5).

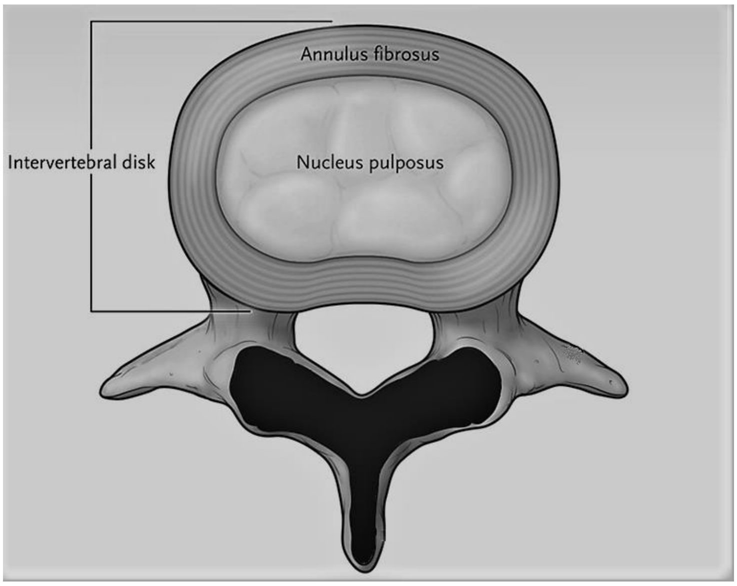

Figure 1-5 Cross section of the intervertebral disc and vertebra, highlighting the annulus fibrosus and nucleus pulposus (Adams, 2004).

1.3 Causation of LBP

The causes of LBP are still not fully understood due to the complex structure and function of the spine. Pain could arise from any of the subcomponents of a motion segment, including the facet joints, spinal ligaments, nerve roots and endings, periosteum, fascia and even the annulus fibrosus. The lack of proper diagnostics combined with the uncertain contributing factors means that in some cases a precise patho-anatomical diagnosis cannot be achieved, although the most common source of LBP may reflect musculo-ligamentous injuries (Deyo & Weinstein, 2001). Table 1-1 below shows some forms of LBP and potential contributing factors.

Table 1-1 LBP diseases and potential contributing factors.

Disease	Contributing Factors
Facet joint instability	Disc herniation and degeneration (Lorenz, et al., 1983), (Shirazi-Adi & Drouin, 1987)
Spinal stenosis	Tumour, genetic (Deyo & Weinstein, 2001), (Hangai, et al., 2008)
Vertebral fracture	Osteoporosis, osteogenesis imperfecta, lytic lesions from metastatic or primary tumours, or infection (Buckens, et al., 2014)
Disc herniation	Smoking, high cholesterol (Hangai, et al., 2008), (Jhawar, et al., 2006)
Disc degeneration	Smoking/lifestyle (Hangai, et al., 2008), (Vogt, et al., 2002)

1.4 Treatment

In order to understand why more representative spinal element models are required, it is important to understand the scope of treatments for LBP. Importantly, as the models become more representative, the better our understanding of the intricate assemblies and interactions between soft and hard tissues.

Although it is difficult to pinpoint the origin of LBP, treatments have been developed for the more prominent and detectable spinal ailments. Generally, there are two types of surgery, one focusing on decompression, and the other aiming to stabilise the spine. Key examples of both types are provided below.

1.4.1 Decompression operations

These types of operations usually involve the removal of materials to reduce pressure on nerves, which can often cause pain and numbness.

Laminotomy or laminectomy is used to reduce or eliminate pressure on the spinal cord and nerves. The lamina is the outer structure running down the length of the spine (Figure 1-2). During surgery, it is typical for the surgeon to remove a small portion of the lamina, and this does not have an adverse effect on the biomechanical response of the entire structure (Eidelson, 2018).

Facetectomy is usually needed when bone spurs develop around the contact faces of the vertebrae, or the actual joints become enlarged. This can cause nerve compression and thus pain. A small portion of the facet is usually removed to obtain access to the IVD. If a significant portion of the facet is removed, the resulting stability issues may require further surgery.

Foraminotomy removes excess bone from the foramen, i.e. the passageway from which the nerves exit the spinal canal. If this starts constricting the nerves, surgery is required to remove bone tissue in order to relieve the pressure.

Discectomy involves the removal of part of an IVD. This is required if the IVD herniates, because the exposed portion of the herniated disc can apply pressure to the nerves. A portion of the disc is excised in order to relieve this pressure. This surgery is usually combined with laminectomy or facetectomy to reach the affected area.

1.4.2 Stabilisation operations

Stabilisation surgery is usually required after spinal damage, including damage caused by the removal of tissue for decompression. Stability can also be compromised by the herniation of multiple discs or due to degenerative disc disease (DDD).

Vertebroplasty is usually carried out to align the spinal column following compression fractures or in patients suffering from osteoporosis (Abitpol, 2018). This is minimally invasive surgery usually performed under local anaesthesia, which involves cementing the bone to regain stability, posture, height and function, and to relieve pain.

Spinal fusion is a highly invasive surgery with a long recovery period. It is usually carried out on patients with vertebral tumours and fractures, DDD, or spinal column deformities such as scoliosis (Dehn & Boeree, 2007). Spinal fusion is the traditional method used to stabilise the spine. During fusion, a surgeon removes the disc and the facet joints, packs the space with a bone graft and inserts spacers, screws, and rods into the bones to temporarily fix them. The graft eventually fuses, restricting and connecting the affected vertebrae. This of course means one or more joints are now immobilised, reducing the patient’s range of motion. This surgery carries a higher risk of complications than vertebroplasty and is more expensive (Croft, et al., 1993).

Disc replacement is usually offered as an alternative to spinal fusion. The advantage of this approach is that it addresses predominantly soft tissue damage, which is harder to identify, therefore reducing the risk that spinal fusion might not cure the underlying issue causing LBP. During this procedure, the IVD is removed and replaced with an artificial one (Dehn & Boeree, 2007). This usually restores the height of the disc to its original value and helps to prevent the degradation of the adjacent joint, while maintaining mobility.

1.4.3 Current models of the spine

As stated above, our understanding of the function and behaviour of the human spine can be improved by testing models. Several such models are already available, and three main types can be identified: biological (derived from real spines), physical (artificial analogues) and computational (digital analogues). These three types of model are compared in Table 1-2.

Table 1-2 Different types of models of the spine and spinal motion segments.

Models				
Biological		Physical		Computational
Human	Animal	Anatomical	Mechanical	FEA

1.4.3.1 Biological

1.4.3.1.1 Human cadaveric spines

Human cadaveric spines are the gold standard for any biomechanical applications because they are clearly both mechanically and anatomically correct. However, like most cadaveric material, human cadaveric spines vary in quality and relevance due to demographic and medical factors, as well as parameters such as age and gender. It is difficult to determine where a cadaveric specimen lies in relation to the rest of the population without a large sample size [(Zengin, et al., 2016), (Gerace, et al., 1994)]. The costs of obtaining, storing and disposing of cadaveric materials are high, and the need for large numbers of samples would compound these costs (Busscher, et al., 2010). Furthermore, with the rare exception of twins, a cadaveric spine could never be used as a patient-specific analogue.

In addition, cadaveric material can only be used within a specific time window, because rigor mortis influences the mechanical response of biological materials [(Wilke, et al., 1998), (Anderson, et al., 2009)]. Freeze-thaw cycles associated with the storage of cadaveric materials have adverse effects on hard and soft tissues alike, and must therefore be kept to a minimum [(Wilke, et al., 1998), (Hongo, et al., 2008)]. Logistical issues include the attachment of any sensory equipment such as markers and transducers without adversely affecting the structure and function of the specimen, e.g. the placement of a pressure gauge within a facet joint.

Due to these factors, as well as the ethical complications surrounding the use of human cadavers, there is a significant need for a more suitable model.

1.4.3.1.2 Animal cadaveric spines

Animal cadavers are increasing in popularity as models, partly due to the less stringent ethical restrictions compared to human cadaveric material. In addition, animal cadavers are less variable, especially when the provenance, medical history and other relevant parameters can be closely monitored while the animal is alive, which is usually the case for animals intended for the food supply chain.

Animals that have been used to provide human spinal analogues include sheep (Wilke, et al., 1997), dogs (McAfee, et al., 1988), cattle (Wilke, et al., 1997) and pigs (Dath, et al., 2007). The porcine spine is the closest anatomically to the human spine, even though pigs are a quadruped species (McLain, et al., 2002). Some of the issues that affect the use of human cadavers, such as storage costs, the effect of freeze-thaw cycles, and time-of-use restraints due to material deterioration, also inevitably affect animal carcases.

Some of the work in this thesis involves porcine spine segments. Their performance in loading experiments is only an approximation of the human spine, but the methods developed using this material provides a useful basis for future modelling.

1.4.3.2 Physical Models

1.4.3.2.1 Anatomically-correct models

Anatomically-correct models are intended for guidance and training purposes. They accurately represent the morphology of the biological structure but no attempt is usually made to replicate its mechanical properties, making them unsuitable for biomechanical testing. Such models tend to be constructed from materials that are inexpensive and long-lasting but bear little resemblance to the properties of the modelled structure.

1.4.3.2.2 Mechanically-correct models

Mechanically-correct models are widely used in the medical device manufacturing industry. They are mechanically correct within a given tolerance and accurately represent the population for which they were designed. These models are suitable for biomechanical testing (e.g. to determine fatigue) and are standardised by the American Society for Testing and Materials (ASTM).

The drawback of these models is the lack of any anthropomorphic characteristics. Their sole purpose is accurate mechanical representation and they tend to be machine-like assemblies rather than resembling real biological joints. The manufacturing process is highly reproducible so there is little variation among models of the same type, ruling out their use as patient-specific analogues. However, such models are readily available, and tend to have a very long shelf life, depending on the elastomeric properties and degradation characteristic of the corresponding materials.

1.4.3.3 Computational models

The power of computers has increased exponentially over the last few decades. For example, the processing power of current smart phones is thousands of times greater than the state-of-the-art computers installed in the Apollo spacecraft in the 1960s. This means that digital or *in silico* models of spinal motion segments can now achieve an unprecedented degree of accuracy. The available models are used to provide guidance for custom and generic implant manufacturing. They are used in the early stages of testing and provide a good reference point for mechanical interactions, while also allowing developers to introduce new properties and variables.

One of the greatest advantages of digital models is their indefinite shelf life (licences and updates permitting). However, like the other models described in this section, computer models also suffer inherent limitations. No such models are yet commercially available, and commissioning even a single model requires a large investment in equipment and operator time. In addition, there are no set protocols for the creation of such models, so programming is heavily user dependent, resulting in great variations between institutes, research laboratories and companies. This also limits the comparison of results between similar studies based on different models. Finally, as is the case for all computational models, assumptions must be made during their development and implementation, thus limiting their accuracy and applicability.

1.5 Solution – the current study

The research described in this thesis involves the use of current technologies to create a series of patient-specific analogues of single and multiple spinal motion segments which are both anatomically and mechanically accurate. This means that the analogues must incorporate both VBs and IVDs. Before this is possible, it is necessary to develop IVD analogues with a more realistic response to normal loading parameters, which in turn depends on more detailed information about the role of the facet joints.

Any analogue considered for biomechanical testing must satisfy some basic criteria, the importance of which varies depending on the application. The nine factors set out below are particularly relevant for analogue development:

1. Morphological accuracy – to ensure relevance and utility

2. Mechanical accuracy – to provide an accurate representation of the biological specimen
3. Low model variance – to achieve consistency during testing
4. Model (patient) specificity – to overcome the limitations associated, for example, with anatomically-correct models
5. Mechanical property adjustability – allowing the adjustment of key variables
6. Manufacturing cost – to facilitate uptake and dissemination
7. Shelf and test life – to maximise testing and storage time
8. Environmental sustainability – to minimise any environmental hazards
9. Lead time – minimised to allow the deployment of patient-specific models within a medically-relevant time frame

In light of the above, this study focuses on the creation of a mechanical model based on the porcine lumbar spine, which closely resembles the human spine. This model will develop and evolve, from a single component to a multiscale assembly based on the CT scans of individual patients. These will be analysed, and then physical models will be created and validated against original cadaveric samples. A corresponding *in silico* model will also be developed to reinforce the validation loop of the physical model.

This will lead to a better understanding of the methodologies and techniques involved in creating a cost-effective, accurate and patient-specific motion segment replica. The development of such a model will have a substantial impact on the design, development, manufacturing and validation of such models to follow.

1.6 Aims and Objectives

The overall aim of this research is to understand the fundamental issues involved when developing and validating an analogue for a patient-specific spinal motion segment, while overcoming other current hurdles such as storage issues, lead time and most certainly cost.

Three objectives have been defined to achieve the overall aim set out above. These allow the work described herein to be divided into several independent packages with specific deliverables.

- **Objective 1:** Investigate and conduct mechanical testing and data acquisition by DIC on single-component 3D-printed samples derived from CT data
- **Objective 2:** Develop multicomponent 3D-printed analogues derived from CT data, validated by DIC and compressive mechanical testing
- **Objective 3:** Develop an FEA model validated against mechanical tests on both single-component and multi-component 3D-printed analogues, all of which are again derived from patient CT data.

1.7 Thesis plan

This thesis is written in the paper-style format, where each chapter is presented as a standalone document in the form of a journal paper.

The research and writing were undertaken solely by the author unless otherwise stated, with editing and feedback input from other collaborators as defined in the additional author listings and acknowledgements.

The initial part of this thesis outlines the requirement for the research, highlighting the inadequacy of the current standard models, and provides some background on the biomechanical relationships among the spine components to be modelled. Finally, it outlines the steps followed during the research as well as the objectives to be met, as shown in Table 1-3 and outlined in the corresponding flow-chart (Figure 1-6). The key chapters are summarised below:

- Chapter 2 (Paper 1) describes the development of methods for the creation of 3D-printed components derived from the CT scans of individual patients. The printing capabilities are assessed, the post scanning analysis workflow is defined, and a protocol is established for data collection by DIC. This body of work was performed using scans of a human skull, and lessons from this application formed the basis for the rest of the experiments described in this thesis. Although it acted as a “proof of concept”, it nevertheless achieved meaningful scientific advances with important direct applications.

- Chapter 3 (Paper 2) introduces an FEA model based on the mechanical and morphological properties of the skull analogue. The objective was used to improve our ability to apply FEA using the least complex approach while demonstrating its ability to predict the behaviour of the mechanical analogue. This work was carried out under the guidance of the late Dr. M. C. Gibson, my associate supervisor at the time.
- Chapter 4 (Paper 3) is a direct evolution of Chapter 2, in the sense that the methodology (including data acquisition, development and manufacturing) was derived from Chapter 2. The main difference concerns the introduction of a multi-component assembly for a spine motion and the use of in-house CT scanning. This facilitated the control of further variables and the characterisation of their associated effects.
- Chapter 5 (Paper 4) describes how the composition of the analogue IVD was altered to provide a better representation of the cadaveric sample. Different variables were critically assessed (scanning resolution, post-scanning thresholding and DIC fine-tuning) to identify their effect. In addition, the facet joint response was also introduced in order to understand and quantify the role of facets under compressive loading.
- Chapter 6 (Paper 5) takes the results from Chapter 5 and the previous methods developed in Chapter 3 and creates a more complex parametric study of a more complicated and more representative FEA model of a spine motion segment. This model was created using a multiscale approach, and the work described in this chapter identifies the major factors affecting its accuracy.
- Chapter 7 draws together the results and conclusions from the previous chapters, providing a central discussion of the work undertaken during this PhD.

- The concluding chapter (Chapter 8) summarises the work while highlighting the outcomes and how these have helped meet the objectives. In addition, it identifies areas of limitation and further work needed to add to the current body of research.

The work described herein would not been possible without the help and drive of the Thesis Committee and Supervisory Team. This research developed a critical assessment of the capabilities and methods needed to create a patient-specific analogue of a spinal motion segment.

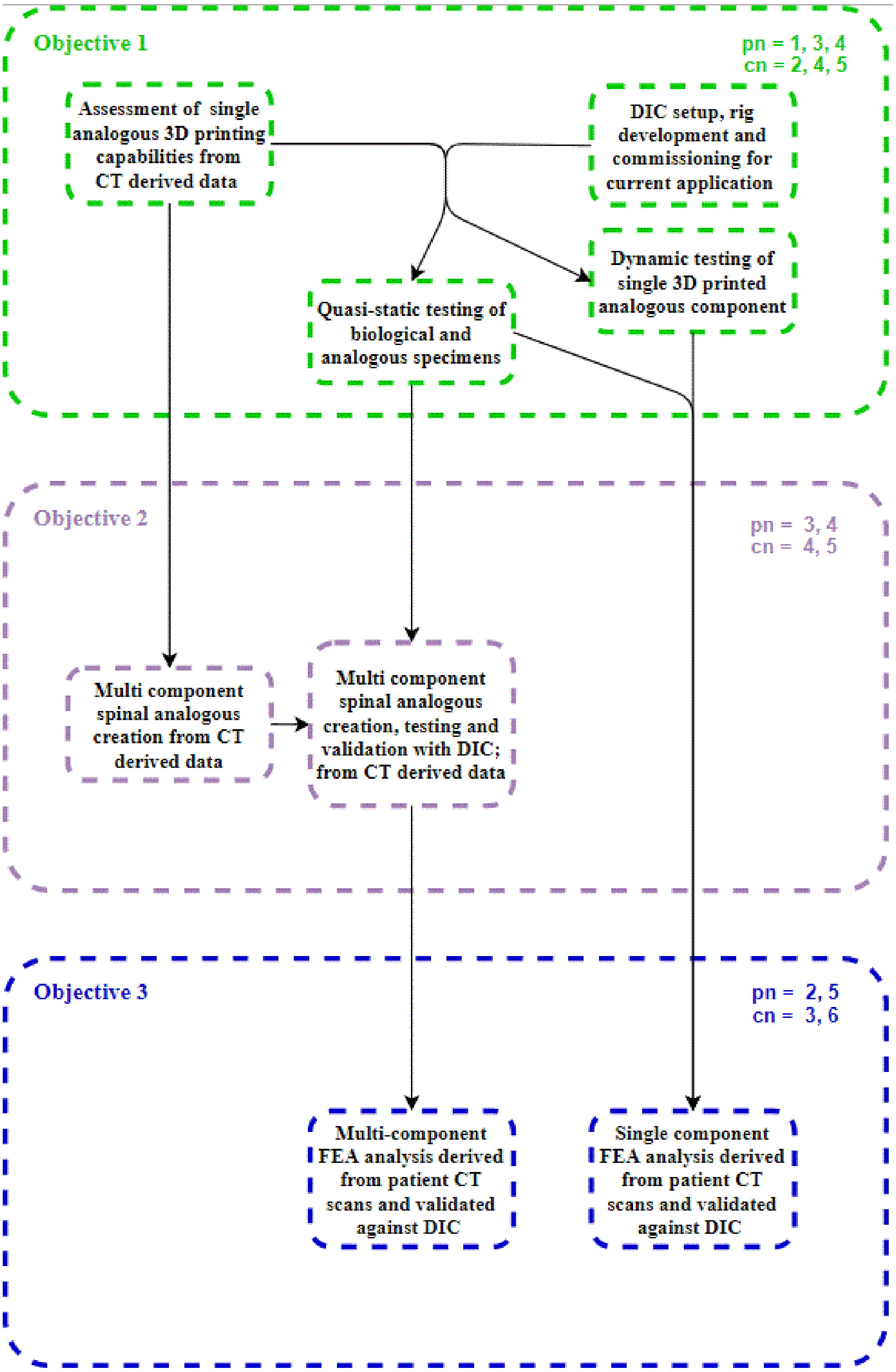

Figure 1-6 Outline of the thesis, showing how the individual chapters contribute to the subsequent chapters to achieve the primary objectives (pn = paper number, cn = chapter number).

Table 1-3 Status of work intended for publication, including working title, proposed journals and the corresponding objectives. The associated conference presentations are also included.

Chapter	Paper	Objective	Title	Conference
2	1	1	EVALUATION OF BONE EXCISION EFFECTS ON A HUMAN SKULL MODEL – I: MECHANICAL TESTING AND DIGITAL IMAGE CORRELATION	ESB 2016 SIMBIO-M 2018 SAFE EUR 2017
3	2	3	EVALUATION OF BONE EXCISION EFFECTS ON A HUMAN SKULL MODEL – II: FINITE ELEMENT ANALYSIS	SIMBIO-M 2018
4	3	1,2	SPINAL MOTION SEGMENTS: CONCEPT FOR A SUBJECT-SPECIFIC ANALOGUE MODEL	SAFE EUR 2017 SAFE US 2017
5	4	1,2	SPINAL MOTION SEGMENTS: TUNING AND OPTIMISATION OF BIOFIDELIC PERFORMANCE	ESB 2017 SAFE US 2017
6	5	3	MULTISCALE MODELLING AND TESTING OF A PORCINE LUMBAR SPINE MOTION SEGMENT ANALOGUE	CMBBE 2015
7	6	1,2,3	OVERALL DISCUSSION	SAFE EUR 2017
8	-	-	FUTURE WORK	-

1.8 References

Abitpol, J.-J., 2018. *Kyphoplasty, Vertebroplasty, Vertebral Augmentation Implant: Treatments for Spinal Compression Fractures,* Montclair, NJ, USA: Spine Universe.

Adams, M., 2004. Biomechanics of back pain. *Acupuncture in Medicine,* 22(4), p. 178.

Anderson, A. L. et al., 2009. The effect of posterior thoracic spine anatomical structures on motion segment flexion stiffness. *Spine,* 34(5), pp. 441-446.

Buckens, C. F., de Jong, P. A., Mali, W. P. & Verhaar, H. J., 2014. Prevalent vertebral fractures on chest CT: higher risk for future hip fracture. *Journal of bone and mineral research,* 29(2), pp. 392-398.

Busscher, I. et al., 2010. In Vitro Biomechanical Characteristics of the Spine: A Comparison Between Human and Porcine Spinal Segments. *Spine*, 35(2), pp. 35-42.

Croft, P. et al., 1993. The prevalence of chronic widespread pain in the general population. *The Journal of Rheumatology,* 20(4), pp. 710-713.

Currey, J. D., 2002. *Bones: Structure and Mechanics.* 2006 ed. Woodstock, UK: Princeton University Press.

Dath, R., Ebinesan, A. D., Porter, K. M. & Miles, A. W., 2007. Anatomical measurements of porcine lumbar vertebrae. *Clinical Biomechanics,* Volume 22, pp. 607-613.

Dehn, T. & Boeree, N., 2007. Degenerative Disc Disease: Disc Replacement. *Annals of The Royal College of Surgeons of England,* 89(1), p. 6.

Deyo, R. A. & Weinstein, J. N., 2001. Low Back Pain. *The New England Journal of Medicine,* 344(5), pp. 363-370.

Domann, J. P., 2011. *Development and Validation of an Analogue Lumbar Spine Model and its Integral Components,* Lawrence, KS, US: University of Kansas.

Eidelson, S. G., 2018. *Laminotomy versus Laminectomy,* Montclair, NJ. USA: Spine Universe.

Ensign, W. et al., 2000. *A survey of self-reported injuries among special boat operators,* San Diego, CA, USA: Naval Health Research Center.

Ferguson, S. & Steffen, T., 2003. Biomechanics of the aging spine. *European Spine Journal,* 12(2), pp. 97-103.

Gerace, L. et al., 1994. Skeletal differences between black and white men and their relevance to body composition estimates. *American Journal of Human Biology,* 6(2), pp. 255-262.

Hangai, M. et al., 2008. Factors associated with lumbar intervertebral disc degeneration in the elderly. *The Spine Journal,* 8(5), pp. 732-740.

Hongo, M. et al., 2008. Effect of multiple freeze-thaw cycles on intervertebral dynamic motion characteristics in the porcine lumbar spine. *Journal of Biomechanics,* 41(4), pp. 916-920.

International Organization for Standardization, 1997. *Mechanical vibration and shock -- Evaluation of human exposure to whole-body vibration -- Part 1: General requirements,* Geneva: International Organization for Standardization.

Jhawar, B. S., Fuchs, C. S., Colditz, G. A. & Stampfer, M. J., 2006. Cardiovascular risk factors for physician-diagnosed lumbar disc herniation. *The Spine Journal,* 6(5), pp. 684-691.

Knott, L. & Bailey, A. J., 1998. Collagen cross-links in mineralizing tissues: a review of their chemistry, function and clinical relevance. *Bone,* 22(3), pp. 181-187.

Konstantinou, K. & Dunn, K. M., 2008. Sciatica: Review of Epidemiological Studies and Prevalence Estimates. *Spine,* 33(22), pp. 2464-2472.

Landis, W. J., 1995. The strength of calcified tissue depends in part on the molecular structure and organization of its constituent mineral crystals in their organic matrix. *Bone,* 16(5), pp. 533-544.

Leone, A., 2007. Lumbar intervertebral instability: A Review. *Radiology,* 245(1), pp. 62-77.

Lorenz, M., Patwardhan, A. & Vanderby, R., 1983. Load-bearing characteristics of lumbar facets in normal and surgically altered spinal segments. *Spine,* 8(2), pp. 122-130.

Marine Accident Investigation, 2009. *Report on the investigation of injury to a passenger on board the RIB, Celtic Pioneer, Bristol Channel,* Southampton, UK: Marine Accident Investigation Branch.

Martin, R. B. & Burr, D. B., 1989. Structure function and adaptation of compact bone. *American Journal of Physical Anthropology,* 82(1), pp. 116-117.

Mayfield Clinic, 2018. *Mayfield Certified Health Info Materials,* Cincinnati, OH, USA: Mayfield Clinic.

McAfee, P. C. et al., 1988. The biomechanical and histomorphometric properties of anterior lumbar fusions: a canine model. *Journal of spinal disorders,* 1(2), pp. 101-110.

McLain, R. F., Yerby, S. A. & Moseley, T. A., 2002. Comparative morphometry of L4 vertebrae: comparison of large animal models for the human lumbar spine. *Spine,* 27(8), pp. 200-206.

Özkaya, N., Nordin, M., Goldsheyder, D. & Leger, D., 2017. *Fundamentals of Biomechanics - Equilibrium, Motion, and Deformation.* 3rd ed. Cham, Switzerland: Springer International Publishing.

Resnick, D. K., Weller, S. J. & Benzel, E. C., 1997. Biomechanics of the thoracolumbar spine. *Neurosurgery clinics of North America,* 8(4), pp. 455-469.

Rissanen, P., 1964. Comparison of pathologic changes in intervertebral discs and interspinous ligaments of the lower part of the lumbar spine in the light of autopsy findings. *Acta Orthopaedica,* 34(1), pp. 54-65.

Sharma, M., Langrana, N. A. & Rodriquez, J., 1995. Role for ligaments and facets in lumbar spinal stability. *Spine,* 20(8), pp. 887-900.

Shirazi-Adi, A. & Drouin, G., 1987. Load-bearing role of facets in a lumbar segment under sagittal plane loadings. *Journal of Biomechanics*, 20(6), pp. 601-613.

Silva, M. J., Wang, C., Keaveny, T. M. & Hayes, W. C., 1994. Direct and computed tomography thickness measurements of the human, lumbar vertebral shell and endplate. *Bone*, 15(4), pp. 409-414.

Taimela, S., Kujala, M. U., Salminen, J. J. & Vijanen, T., 1997. The prevalence of low back pain among children and adolescents. A nationwide, cohort-based questionnaire survey in Finland. *Spine,* 22(10), pp. 1132-1138.

Viquet-Carrin, S., Garnero, P. & Delmas, P. D., 2006. The role of collagen in bone strength. *Osteoporosis International,* 17(3), pp. 319-336.

Vogt, M. T., Hanscom, B., Lauerman, W. C. & Kang, J. D., 2002. Influence of Smoking on the Health Status of Spinal Patients. *Spine,* 27(3), pp. 313-319.

Wilke, H. J., Jungkunz, B., Wenger, K. & Claes, L. E., 1998. Spinal segment range of motion as a function of in vitro test conditions: effects of exposure period, accumulated cycles, angular-deformation rate, and moisture condition. *The Anatomical Record,* 251(1), pp. 15-19.

Wilke, H. J., Kettler, A. & Claes, L. E., 1997. Are sheep spines a valid biomechanical model for human spines?. *Spine,* 15(22), pp. 2365-2374.

Wilke, H. J., Krischak, S. T., Wenger, K. H. & Claes, L. E., 1997. Load-displacement properties of the thoracolumbar calf spine: experimental results and comparison to known human data. *European Spine Journal,* 6(2), pp. 129-137.

Wilke, H. J., Wenger, K. & Claes, L. E., 1998. Testing criteria for spinal implants: Recommendations for the standardization of in vitro stability testing of spinal implants. *European Spina Journal,* 7(2), pp. 148-154.

Zengin, A. et al., 2016. Ethnic differences in bone geometry between White, Black and South Asian men in the UK. *Bone,* Volume 91, pp. 180-185.

Zioupos, P., Cook, R. B. & Hutchinson, J. R., 2008. Some basic relationships between density values in cancellous and cortical bone. *Journal of Biomechanics*, 41(9), pp. 1961-1968.

2 EVALUATION OF BONE EXCISION EFFECTS ON A HUMAN SKULL MODEL – I: MECHANICAL TESTING AND DIGITAL IMAGE CORRELATION

Constantinos Franceskides[1*], Thibault Leger[2], Ian Horsfall[3], Gianluca Tozzi[4], Michael Gibson[5], Peter Zioupos[1]

[1]*Musculoskeletal and Medicolegal research Group, Cranfield Forensic Institute, Centre for Defence Engineering, Cranfield University, Defence Academy of the UK, Shrivenham, SN6 8LA, UK*

[2]*Materials Science, University of Paris-Sud, Orsay, France*

[3]*Impact and Armour Group, Centre for Defence Engineering, Cranfield University, Defence Academy of the UK, Shrivenham, SN6 8LA, UK*

[4]*School of Engineering, University of Portsmouth, Anglesea Road, Portsmouth, PO1 3DJ, UK*

[5]*Centre for Simulation & Analytics, Centre for Defence Engineering, Cranfield University, Defence Academy of the UK; Shrivenham, SN6 8LA, UK*

2.1 Abstract

The mechanisms of skull impact loading may change following surgical interventions such as the removal of bone lesions, but little is known about the consequences in the event of subsequent head trauma. We therefore prepared acrylonitrile butadiene styrene human skull models based on clinical computed tomography skull data using a 3D printer. Six replicate physical skull models were tested, three with bone excisions and three without. A drop-tower was used to simulate the impact sustained by falling backwards onto the occipital lobe region. The impacts were recorded with a high-speed camera and the occipital strain response was determined by digital image correlation (DIC). Although the hole affected neither the magnitude nor the sequence of the fracture pattern, DIC analysis highlighted an increase in strain around the excised area (0.45–16.4% of the principal strain). Our approach provides a novel method that could improve the quality of life for patients on many fronts, including protection against trauma, improved surgical advice/post-operative care, and advice in litigation cases, as well as facilitating general biomechanical research in the area of trauma injuries.

Keywords: Biopsy; Bone fracture; Strains; Digital image correlation; Physical models; Impact

2.2 Introduction

Between 2010 and 2015, more than 1 million falls resulting in head injuries, averaging ~200,000 per year, were recorded by the Health and Social Care Information Centre (HSCIC) of the United Kingdom (NHS Digital, 2016). During the same period, an average of 440 skull biopsies was conducted per year (Table 2-1).

Table 2-1 HSCIS data showing the number of falls resulting in head injuries and the number of skull biopsies between 2010 and 2015.

Year	Number of falls resulting in head injuries	Number of skull biopsies
2010–2011	229,177	421
2011–2012	226,002	450
2012–2013	211,895	467
2013–2014	214,900	406
2014–2015	217,529	461
Total	1,099,503	2,205

The consequences of bone and soft tissue tumour surgery, whether for biopsy or full excision, have been investigated since the 1970s (Benjamin, 2014). However, most of these investigations have focused on the biological (histological) impact, with only a few considering the biomechanical aspects [(Clark, et al., 1977); (Errani, et al., 2013)]. Therefore, it is unclear how the mechanisms of head impact loading may change following surgical interventions such as the removal of bone lesions.

With technological advances in biomedical and biomechanical modelling, many researchers have attempted to understand (Monea, et al., 2013) or even predict (Grassi, et al., 2013) musculoskeletal behaviour under different loading conditions. With this in mind, the prediction of bone excision effects could be improved by using previous biomechanical research in concert with evolving technological and mechanical testing methods. The main problems that must be addressed when examining a real-life/real-time loading scenario revolve around three aspects, namely: (1) representative biofidelic loading conditions (in terms of time and boundary effects); (2) accurate, real-time (fast), reliable and non-contact recording of the deformations; and (3) reproducibility of the tests and the samples in order to minimise and control for unknown factors such as biological variability (no real-life sample is like any other, each biological sample is unique). The present study addresses some of these challenges by combining three modern techniques: drop-tower impact loading, digital image correlation (DIC) and 3D rapid prototype printing following computed tomography (CT) scanning.

DIC is a non-contact data acquisition method which achieves full-field strain mapping through the analysis of consecutive images captured by camera. The speed and specifications of the camera allow the rapid capture of high-quality images to facilitate strain analysis in real-time and in high-speed scenarios. DIC has been combined with impact loading of the musculoskeletal system to evaluate effects such as ballistic helmet trauma in the military environment (Hisley, et al., 2010), and to develop and validate a model of infant skull impact loading (Jones, et al., 2017). Furthermore, patient-specific models have been used to validate the conformity of implants by combining finite element analysis (FEA) with DIC [(Sutradhar, et al., 2014); (Palanca, et al., 2016)]. Drop towers are modern instrumented versions of dead-weight impact loading systems, allowing accelerated loading with precise determination of the energy input. Three-dimensional physical model prototype printing has evolved into the most powerful method for the production of life-like models of natural structures. Depending on the sophistication, 3D printing can replicate the fine structural details of bones to the level of individual trabeculae. The information that drives the 3D printing is taken from modern CT scans, which can divide structures into voxels of just a few micrometres (Inglis, 2016).

Only a combination of these modern powerful methods allows us to analyse the loading of mechanically compromised skulls in real time. Despite the advances described above, previous studies have not addressed the influence of biopsies and excisions on the structural integrity of a human skull when exposed to impact loading. We therefore used a 3D printer to prepare human skull models based on clinical CT data from a case study, and then compared the mechanical behaviour of skulls with and without bone excisions in a simulated fall, causing an impact on the occipital lobe region. Our hypothesis was that skull surgery would have a profound effect on the fracture pattern and the dissipation of loading forces.

2.3 Materials and methods

2.3.1 The patient

The replica skulls used in this study were modelled on a 28-year-old male patient who had no previous history of musculoskeletal disorders and no prior bone tissue surgery. The excision to the occipital skull region was performed by a consultant neurosurgeon at Wellington Hospital, London, UK. The patient was otherwise healthy. Ethical approval for the work was granted by the relevant Cranfield University committee and the patient consented under the approval reference CURES/787/2016.

2.3.2 Creation of physical skull models

Six physical skull models were prepared, based on the same post-operative clinical CT scan acquired at a resolution of 0.488 x 0.488 x 1.2 mm and at 120 kV and 400 mA. Two distinct skull geometries were created (with and without the excision) using Simpleware ScanIP v7 (Figure 2-1) (https://www.simpleware.com/software/scanip/).

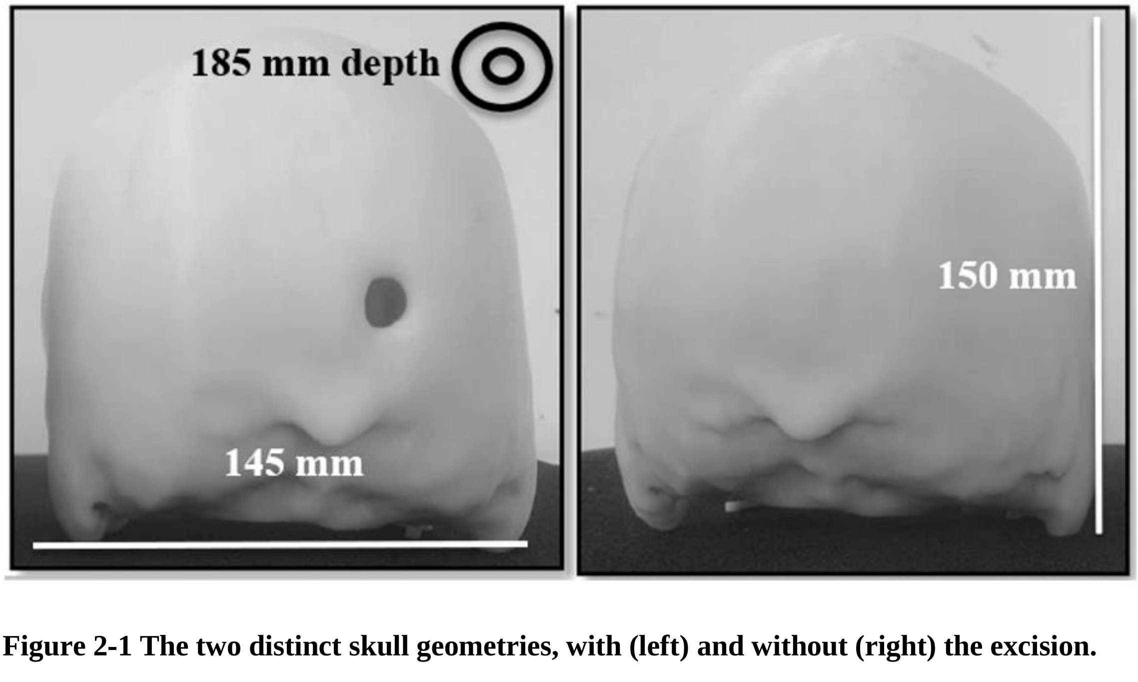

Figure 2-1 The two distinct skull geometries, with (left) and without (right) the excision.

The data were imported as a 32-bit float, but were converted to an 8-bit float and resampled (using the cubic function) to match the voxel axial dimension to the in-plane dimension with the resulting cubic voxels of side length 0.488 mm. A series of masks was then applied, with the appropriate greyscale thresholding and flood fill operations to select only bone matter within the scanned volume. A Gaussian smoothing filter was used to better represent the skull geometry and negate as much as possible the stepped appearance of voxel-based output from CT scanners.

The normal skull geometry was created using the neighbouring morphology, such as the surrounding bone thickness and curvature, thus mimicking as closely as possible the pre-operative condition of the region. The three skull models with an excision (S1, S2 and S3) and the three without (S4, S5 and S6) were imported to Stratasys CatalystEX to create the tool-path files, and then uploaded to the printer. The six physical skull models were printed on an FDM Stratasys UPrintSE 3D printer (http://www.stratasys.com/3d-printers) fitted with a 0.4-mm nozzle, using the acrylonitrile butadiene styrene (ABS) material supplied by the manufacturer. The support fill was set to ‘smart’ and the model interior to ‘solid’. This resulted in a typical printing time of 42 h per skull, requiring almost a complete reel of ABSPlus-P430 material (33 cubic inches). The precise choice of settings resulted from other tests we have conducted on material samples with simple and complex geometries, where we have demonstrated that the force/displacement curves of real biological and 3D-printed samples were identical in the elastic region (Franceskides, 2017). I addition, data observed by a previous study (Woo, et al., 2009) conducted with ABS, supported the use of RP technology and FE analysis in the non-destructive evaluation of the plastic mechanical characteristics of osteoporotic bone.

2.3.3 Refinement of the model skulls

Perma-Gel was used to fill the models in order to mimic the properties of the brain and reproduce its energy absorption and response (Harrington, 2014). The total mass of each model was ~2.1 kg with a maximum variance of 0.040 kg. A solid base was created, also from Perma-Gel, to allow the repositioning of the skulls, thus eliminating orientation errors. All samples were prepared in a similar manner as previously reported [(Vassolera & Fancelloa, 2012); (Pal & Routal, 1987); (Lecompte, et al., 2006)] with a randomised speckle pattern. The black-to-white ratio was kept as close as possible to 1:1, and Castrol White Contrast Paint 710 (2386) non-strippable aerosol was used to apply the high-contrast background evenly over the model surface. Finally, the size of the speckles (Figure 2-2) was determined using the following equations: (Palanca, et al., 2016); (Michael, et al., 2009)

Equation 2-1

$$S_{ideal} = \frac{4 \pm 1}{M} \qquad (1)$$

Equation 2-2

$$M_{factor} = \frac{n_{length\ sensor\ pixels}}{d_{length}} \qquad (2)$$

Figure 2-2 Typical speckle pattern, exemplified using a model with an excision to show the brain simulant within.

Equation **2-1** identifies how the ideal speckle size was calculated, 3 to 5 divided by the magnification factor, as shown in Equation 2-2. The magnification factor is simply the number of sensor pixels over the aperture, or in effect recorded real length (the physical distance a pixel represents within the recorded image).

2.3.4 Drop tests

The drop tests were conducted using an Imatek IM10 drop tower (http://www.imatek.co.uk/) with a total carriage and striker mass of 2.91 kg (Figure 2-3).

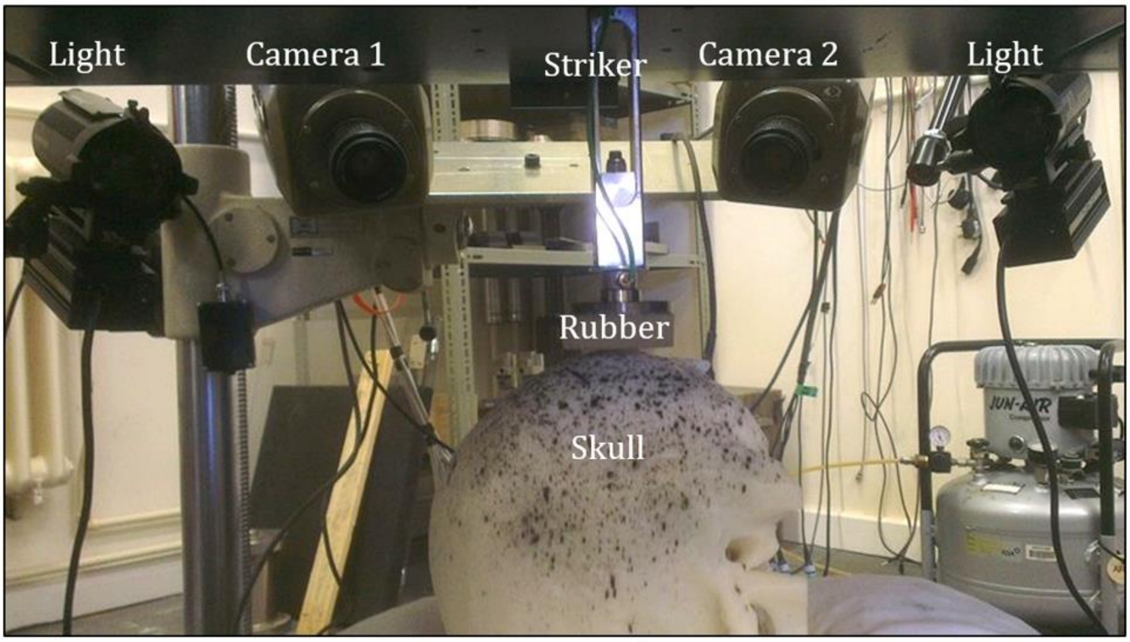

Figure 2-3 The experimental setup for the drop test.

At the end of the carriage, a 45-mm circular titanium striker was fitted with a dampening surface which was adapted from a Humanetics Hybrid III headform thickness of 12.7 mm (http://www.humaneticsatd.com/) with 43 ± 5 Shore hardness ‘A’. This provided a dampening effect and hence a smoother ramp rate, similar to the soft tissues surrounding a real human skull [(Office of Crash Worthiness Standards, 1997); (U.S. Army Medical Research Acquisition Activity, 2014)]. The rubber was manufactured to the specifications described above by Watts Urethane Products Ltd (https://wattspolyurethane.co.uk/). The skulls were subjected to a load on the occipital region proximal to the excision site, mimicking the effect of an unconscious or incapacitated human falling backwards and striking this region on a hard surface.

DIC data were acquired via a series of images captured using two V12.1 Phantom high-speed cameras that were set at a stereo incident angle of 25°, recording at 15,000 fps. The camera was controlled using PCC standalone software (https://www.highspeedcameras.com/Service-Support/PCC-Software), which provided a falling edge signal input from the drop tower to ensure synchronous capture. The data were analysed using GOM software (http://www.gom.com/metrology-systems/system-overview/aramis.html) with quadrangle facets at 19 pixels (size) and 17 pixels (step), 484 3D points generated over 176 stages, and an average intersection deviation of 0.0150 mm.

Due to the confined space of the drop-tower base, artificial lighting was installed to provide consistent lighting conditions. This was achieved using three light sources, namely two conventional halogen lights with focal adjustment, and a light emitting diode (LED) Cree flood light acting as a background source, which was reflected onto the object using a flat mirror placed outside the impact area.

Two series of tests were conducted, with varying striker velocities of 8 m/s at 100 J (T1) and ~9.75 m/s at 130 J (T2). The lower-energy impacts (T1) were used to determine the loading response under the defined testing parameters (50th percentile male adult losing consciousness and falling with direct impact on the occipital region), and the higher-energy impacts (T2) were used to induce failure in the skulls and thus determine the fracture pattern and propagation path.

Equation 2-3

$$\mathrm{V}_{PE} = m \ x \ g \ x \ L \ x \ cos\theta \tag{3}$$

As above mentioned, T1 utilised the height and skull mass of the average (50th percentile, adult male) adult male and applied a simple pendulum equation, as shown above in Equation 2-3, where the incident angle is 0.

2.4 Results and discussion

2.4.1 Preliminary tests on ABS cubes

Little is known about the biomechanical effect of surgical procedures such as bone lesion removal on the response of human skulls to impact trauma. Such interventions may have a detrimental effect on the load response of natural musculoskeletal structures because the integrity of the structure is compromised. This gives rise to legitimate concerns about the morbidity and mortality that may ensue in the aftermath of such procedures if the skull is exposed to subsequent impact trauma.

Consequently, although we set out to test the effect of lesions on 3D physical skull models, before producing the models, preliminary tests were conducted on four 3D-printed ABS cubes with external dimensions of 40 x 40 x 40 mm and 10 mm wall thickness (Figure 2-4) to address some inconsistency in the literature concerning the anisotropy of 3D-printed objects. Some reports indicate a difference in compressive performance depending on the orientation of layers (Cantrell, et al., 2016) whereas others do not (Zou, et al., 2016) thus making it necessary to investigate the variation of layer deposition for this specific printer and material.

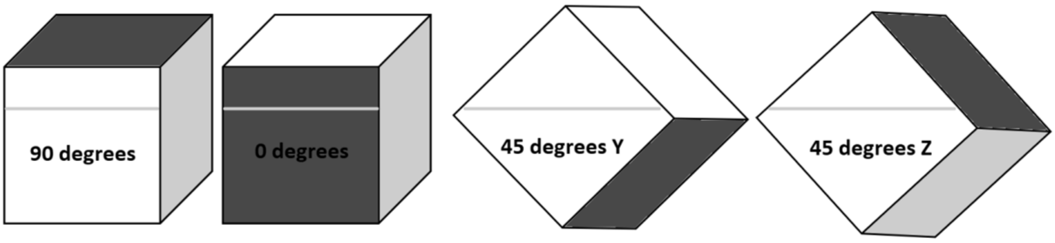

Figure 2-4 Direction of load (dark grey surface) and orientation of layer deposition (line) in 3D-printed cubes.

The dark grey surface in Figure 2-4 indicates where the load was applied, and the line represents the orientation of ABS layer deposition. The cubes were compressively loaded until failure using a Zwick Roell 1484 fitted with a 200 kN load cell (www.zwick.co.uk). The results (Table 2-2) indicated that, despite some layer directionality and inter-laminar bonding, the effect was less than 13% of the maximum compressive yield strength recorded.

Table 2-2 Cube compressive directional properties and anisotropic magnitudes.

Specimen	Gradient (kN/mm)	Gradient %
90 degrees	23.3	100
0 degrees	19.7	85
45 degrees Y	22.2	95
45 degrees Z	21.2	91

The results were similar when comparing moduli in the elastic region, with a difference of less than 16% observed between maximum and minimum values, highlighting the relative isotropy of the 3D printed structures.

2.4.2 Tests on the skull models

Having established the suitability of the test material by the compressive loading of cubes, we prepared physical skull models from a patient with a surgical hole in the occipital region and similar skull models with the excision hole filled to represent the pre-operative state. Three skull models in each configuration were then subjected to drop-tower tests with two impact velocities in order to test the strain responses (T1, low impact) and failure characteristics (T2, high impact). All tests were carried out in a single day to minimise errors and limit the number of models required for testing over the range of velocities/energies we considered.

Eight tests were conducted, six in the T1 state and two (S3 and S4) in the T2 state. During the T1 test series, model S2 suffered a premature failure, which resulted in a greater shear angle (incident shear angle between the viewing facets as analysed within the GOM software) in the proximity of the excision, leading to a lower strain recording (Figure 2-5; Figure 2-6).

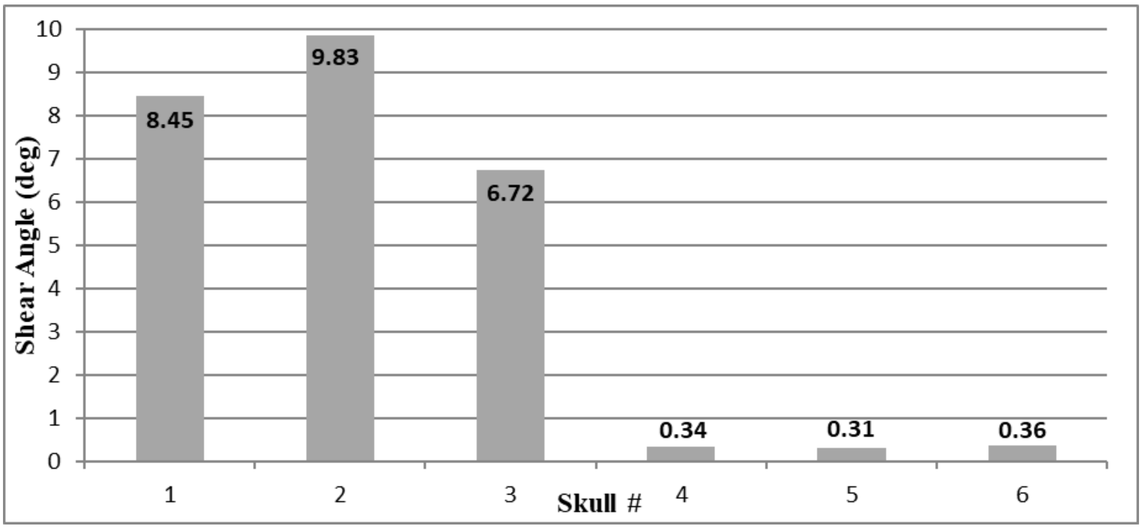

Figure 2-5 Shear angle proximal to excision for the six skull models under T1 test conditions.

During the T2 test series, models S3 and S4 both failed, showing three distinct crack propagation paths. In both cases, the cracks originated in the immediate vicinity of the impact zone.

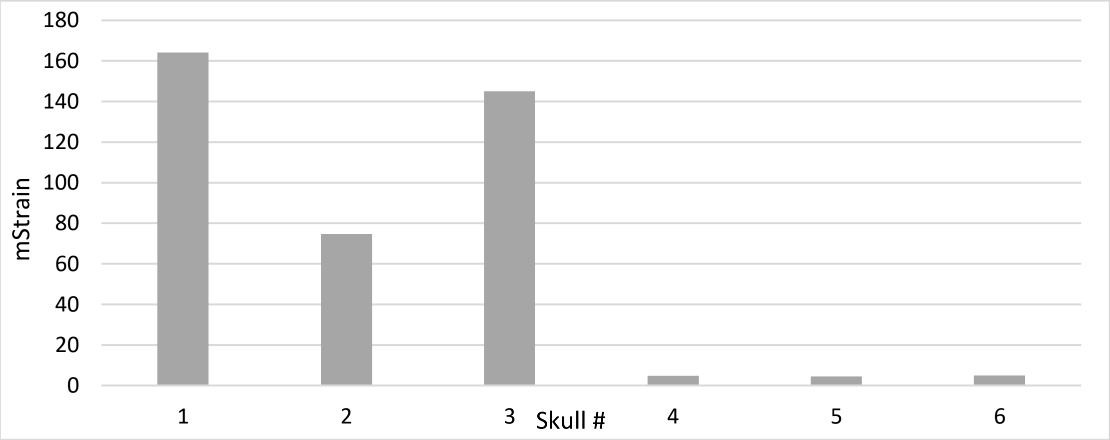

Figure 2-6 Principal strain recording for the six skull models under T1 test conditions.

Crack propagation was very similar in both cases, in extent and orientation. The high-speed videography clearly showed that even the crack branching sequence was the same, not only the manner and sequence of crack propagation, but also the extent.

Figure 2-7 shows models S3 and S4 with the cracks numbered in order of appearance and a rough trace of the extent of each crack.

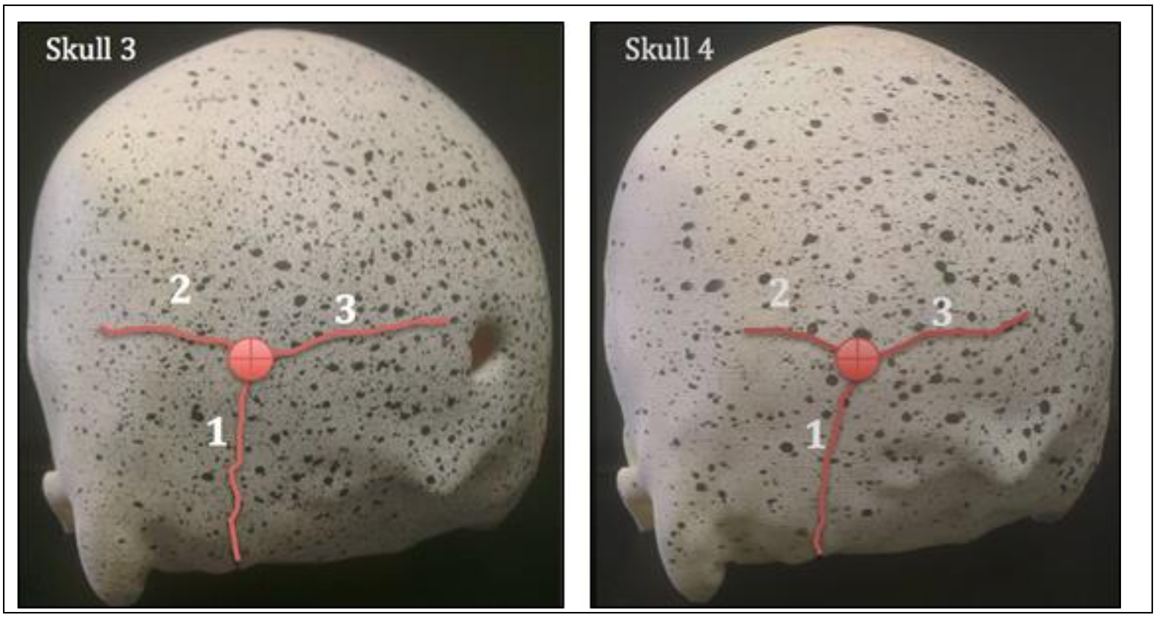

Figure 2-7 The initiation, propagation and magnitude of cracks under T2 test conditions in skull models with (left) and without (right) an excision.

DIC analysis clearly revealed strain concentration on the perimeter of the excision, but not in the case of the healthy skull (Figure 2-8).

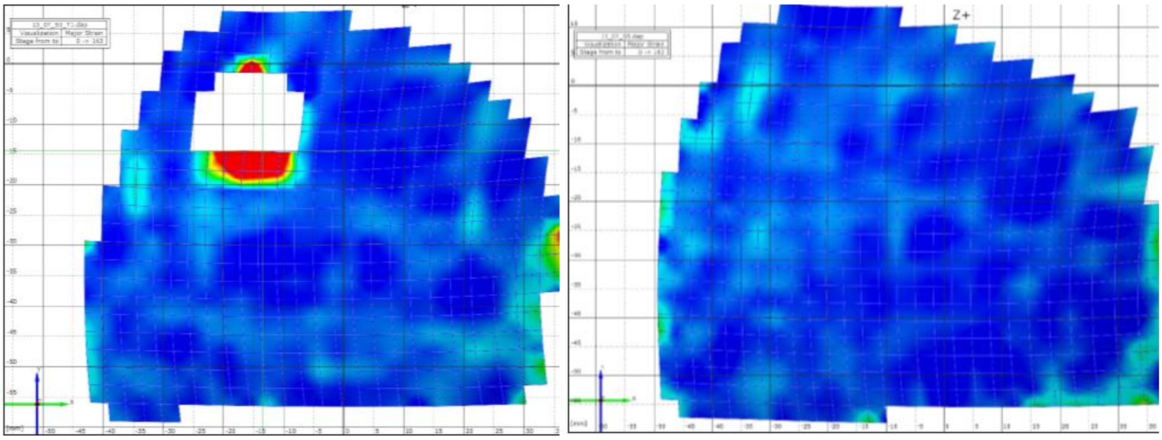

Figure 2-8 Screenshots of the Aramis GOM program showing strain concentration around the perimeter of the excision (left) but no equivalent strain concentration in the healthy skull model (right).

This compressive strain concentration was more noticeable during the elastic loading of the samples. The drop-tower data also revealed consistent velocity decay in each of the skulls (Figure 2-9).

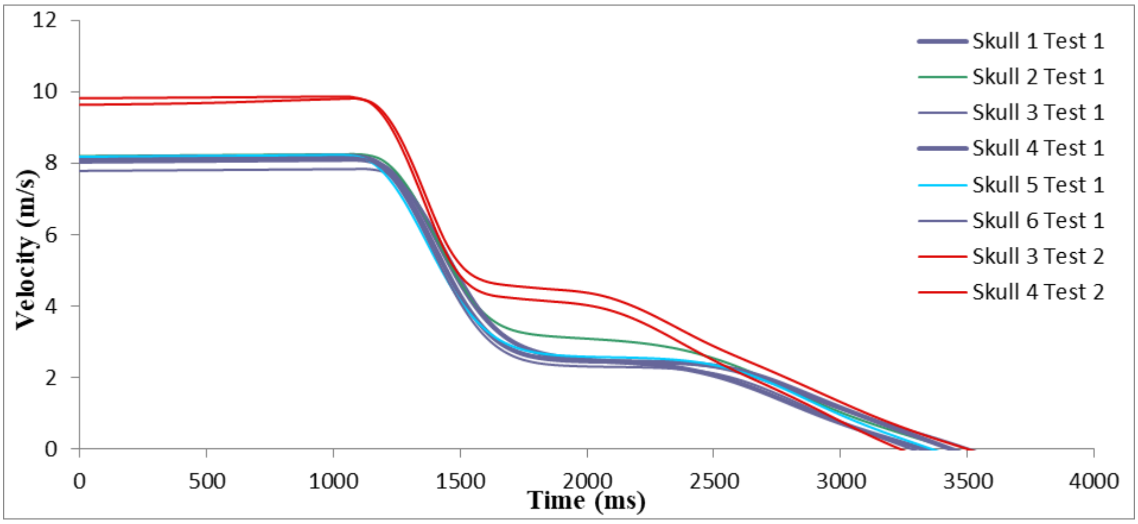

Figure 2-9 Impact velocity vs time decay in the T1 and T2 test environments.

The graduation tendency was similar in the T1 and T2 test environments, with only the magnitude (representing impact speed) differing between the test series. The force decay was also similar in the T1 and T2 test series (Figure 2-10) with the only major difference being the magnitude of the force, even though the T2 test series induced failure in the models.

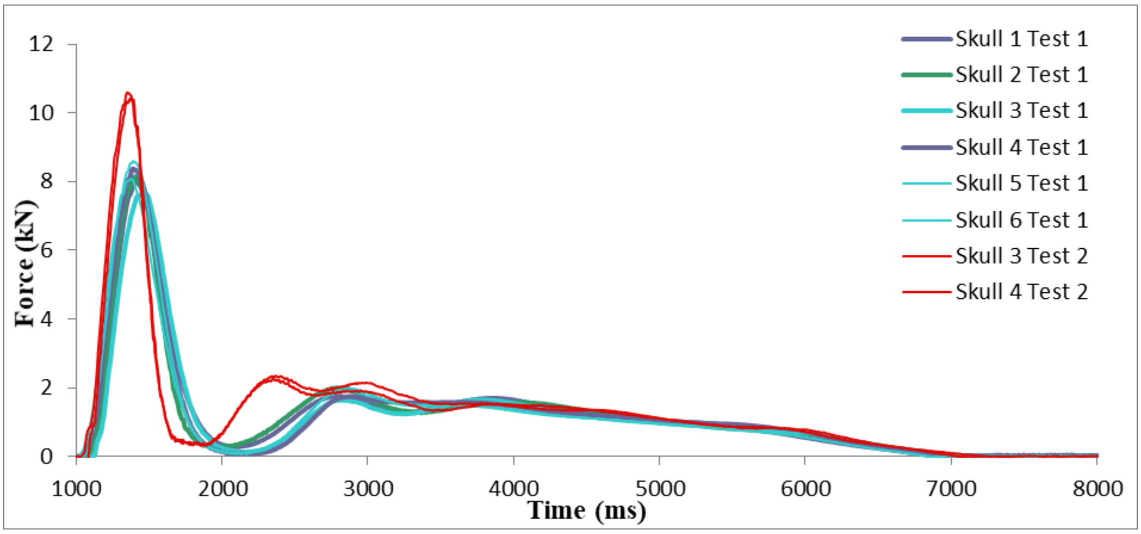

Figure 2-10 Impact force vs time decay for the T1 and T2 test environments.

As anticipated, there was a difference in performance between the two types of model (Figure 2-8, Figure 2-9 and Figure 2-10) which was confirmed by DIC strain mapping. Model S2 showed an unexpected lower principal strain value than models S1 and S3 and experienced failure under milder test conditions. This probably reflected an unanticipated printing anomaly caused by a temporary nozzle blockage and the consequential pause in printing, which allowed the already layered material to solidify, creating a weaker bond. Less energy was therefore absorbed (compared to the other models) before failure, and the resultant energy translated to less elastic deformation.

The T2 test series was conducted with much greater impact energy (130 J) in order to induce a controlled fracture. The energy absorption, velocity decay and force decay were similar in models S3 and S4 (Figure 2-9 and Figure 2-10) and the fracture patterns were nearly identical in location, size and propagation characteristics (Figure 2-7). This can be characterised as a closed linear vault fracture and is very similar in nature to the fracture expected on a real human skull after an impact of this kind (Galloway, 1999). Further analysis of the fracture based on high-speed photography revealed that the origin of the crack was the thinnest part of the skull (lower nuchal lines) and propagation then occurred towards the point of impact, from below the occipital condyle area and propagating up to the inferior nuchal line all the way through the superior nuchal line and terminating at the occipital bone, agreeing with earlier reports based on the behaviour of real skulls (Galloway, 1999).

Our tests were biofidelic to the extent that they precisely replicated the natural structure of the skull bone in shape and form. However, the 3D-printed material is an industrial polymer (ABS) rather than real bone, and the resolution of the printing process was ~400 μm, which inevitably meant that very fine trabeculae in the inner sandwich structure of the skull wall were not reproduced. However, this also meant there was no need to take into account biological variations such as dry versus wet bone properties, because the material in all models was uniform ABS. Other parameters such as fall energy, constraints and contact surfaces were also replicated in the most accurate manner possible. As a striking surface, material similar in mechanical properties to the silicone in the Hymanetics Hybrid III headform was used in order to simulate the skin-muscle-hair interface. Because we carried out a comparative study, both the affected and non-affected skull models had similar material properties, thus allowing comparisons to be made primarily driven by the geometric effect of the excision.

Furthermore, the biopsy hole was filled artificially *in silico* using the ScanIP software, which therefore only approximates the actual shape of a normal skull. The “plug” was of a uniform thickness, but there was still an element of manipulation which might lead to uneven tangential surfaces within the skull vault. Further studies should be conducted to highlight the influence of the void location with respect to the strike location. Indeed, a hole in the thinnest part of the skull might have a much greater effect on the formation and propagation of cracks, and interactions with the location of impact, compared to the models we tested, in which the hole was in one of the thickest parts of the skull. A more complete model, such as a skull attached to the neck, would also provide more realistic responses upon loading. Furthermore, testing with cadaveric skulls would provide validation and also a benchmark for the DIC experimental data, highlighting the potential for future research on this topic.

2.5 Conclusions

A combination of CT scanning, 3D printing, DIC analysis, and drop-tower tests allowed the investigation of real-time loading using mechanically compromised skulls. DIC analysis is useful for the measurement of full-field displacements and strains, especially in non-contact mode. Our experiments confirmed that a hole in the occipital region has a direct influence on strain propagation in the skull, but even though the hole increased the stress, the magnitude was not sufficient to trigger a failure initiating from the hole. Instead, the failure was initiated elsewhere in models with and without the lesion. Although the occipital lesion did not influence the initiation or propagation of cracks, it highlighted that the peripheral area of the excision experiences a much greater strain concentration in the elastic region compared to the rest of the occipital part of the skull. Recent advances in data collection and 3D printing make it feasible that analogue models, such the one used in this study, will be instrumental in providing life-changing results in patient-specific cases.

2.6 Acknowledgments

We acknowledge the work, skill and expertise offered by Karl Norris in the mechanical workshop of Cranfield University, and Jolyon Cleaves of Vision Research for providing the high-speed cameras. Ethical approval was granted by the Cranfield University Research and Ethics Committee (CURES). This paper is dedicated to one of the authors, Dr Mike Gibson, whose untimely death is a great loss to us all.

2.7 References

Benjamin, D. J., 2014. The efficacy of surgical treatment of cancer – 20 years later. *Medical Hypotheses,* 82(4), pp. 412-420.

Cantrell, J. et al., 2016. Experimental Characterization of the Mechanical Properties of 3D-Printed ABS and Polycarbonate Parts. *Advancement of Optical Methods in Experimental Mechanics,* Volume 3, pp. 89-105.

Clark, C., Morgan, C., Sonstegard, D. & Matthews, L., 1977. The effect of biopsy-hole shape and size on bone strength. *The Journal of Bone & Joint Surgery,* 59(2), pp. 213-217.

Errani, C. et al., 2013. Current Concepts in the Biopsy of Musculoskeletal Tumours. *The Scientific World Journal,* Volume 2013, p. 7.

Franceskides, C., 2017. *3D Printing - The future of cost effective biomechanical testing.* Zeist, The Netherlands, SAFE EUROPE.

Galloway, A., 1999. *Broken bones, anthropological analysis of blunt force trauma.* s.l.:Charles C Thomas.

Grassi, L. et al., 2013. Experimental validation of finite element model for proximal composite femur using optical measurements. *Journal of the Mechanical Behaviour of Biomedical Materials,* Volume 21, pp. 86-94.

Harrington, B., 2014. *Study of human head simulant's dynamic response to blast wave,* s.l.: Cranfield University, Defence Academy.

Hisley, D., Gurganus, J. & Drysdale, A., 2010. Experimental Methodology using Digital Image Correlation to Assess Ballistic Helmet Blunt Trauma. *Journal of Applied Mechanics,* Volume 78.

Inglis, S., 2016. 3D Printing in the NHS and healthcare sciences. *IPEM SCOPE - ISSN 0964-9565,* 25(4), pp. 10-13.

Jones, M. et al., 2017. Development and validation of a physical model to investigate the biomechanics of infant head impact. *Forensic Science International,* Volume 276, pp. 111-119.

Lecompte, D. et al., 2006. Quality assessment of speckle patterns for digital image correlation. *Optics and Lasers in Engineering,* 44(11), p. 1132–1145.

Michael, A., Orteu, J. & Schreier, W., 2009. Digital Image Correlation. In: *Image correlation for shape, motion and deformation measurements.* Springer-Verlag: Springer, pp. 1-37.

Monea, A. G. et al., 2013. The relation between mechanical impact parameters and most frequent bicycle related head injuries. *Journal of the Mechanical Behaviour of Biomedical Materials,* Volume 33, pp. 3-15.

NHS Digital, 2016. *Hospital Episode Statistics.* [Online] Available at: http://content.digital.nhs.uk/hes[Accessed 2016].

Office of Crash Worthiness Standards, 1997. *www.unece.org.* [Online] Available at: https://www.unece.org/fileadmin/DAM/trans/doc/2009/wp29/HIII_50th_Male_Drawings.pdf [Accessed 2016].

Palanca, M., Tozzi, G. & Cristofolini, L., 2016. The use of digital image correlation in the biomechanical area: a review. *International Biomechanics,* 3(1), pp. 1-21.

Pal, G. P. & Routal, R. V., 1987. Transmission of weight through the lower thoracic and lumbar regions of the vertebral column in man. *Journal of Anatomy,* Volume 152, pp. 93-105.

Sutradhar, A., Park, J., Carrau, D. & Miller, M. J., 2014. Experimental validation of 3D printed patient-specific implants using digital image correlation and finite element analysis. *Computers in Biology and Medicine,* Volume 52, pp. 8-17.

U.S. Army Medical Research Acquisition Activity, 2014. *Notice for Ballistic Load Sensing Headform System.* [Online] Available at: www.fbo.gov/index[Accessed 2014].

Vassolera, J. M. & Fancelloa, E. A., 2012. Error analysis of the digital image correlation method. *Asociación Argentina de Mecánica Computacional,* Volume XXIX, pp. 6149-6161.

Woo, D. G., Kim, C. H., Lim, D., Kim, H. S., 2009. Experimental and simulated studies on the plastic mechanical characteristics of osteoporotic vertebral trabecular bone. *Current Applied Physics*, Volume 10, pp.729-733

Zou, R. et al., 2016. Isotropic and anisotropic elasticity and yielding of 3D printed material. *Composites Part B: Engineering*, Volume 99, pp. 506-513.

CHAPTER 3 PREFACE

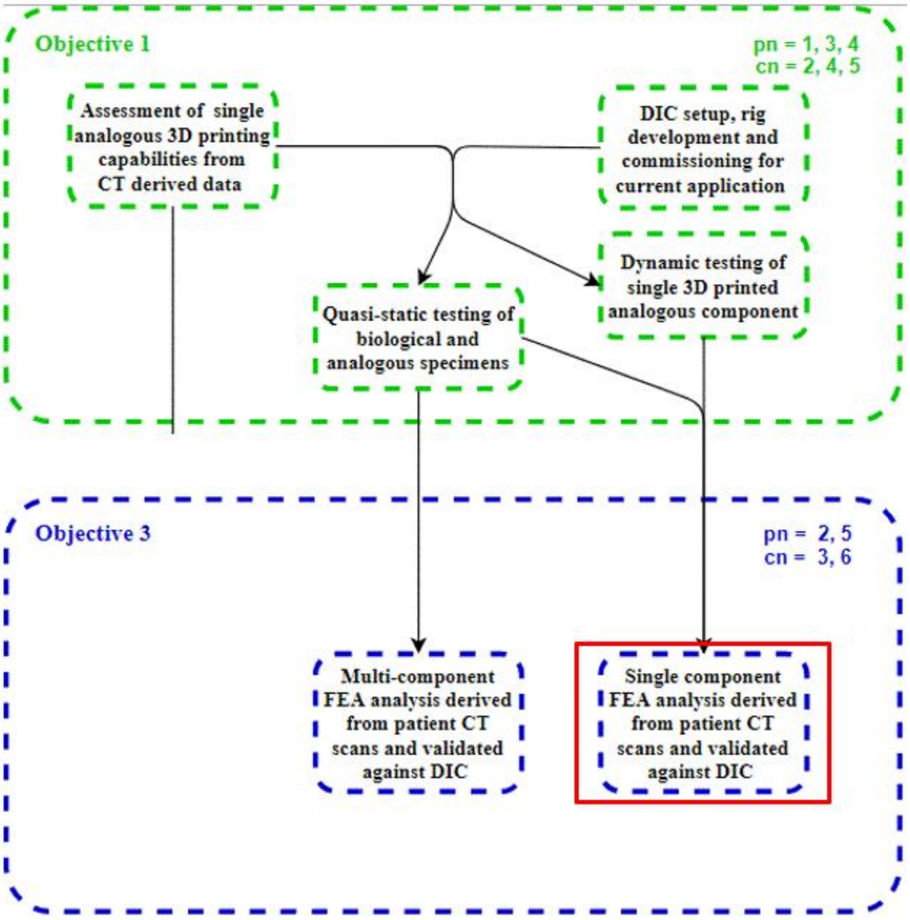

Chapter 2[1] (Paper 1) described the development of a methodology for the creation of 3D-printed components derived from the CT scans of an individual patient. The printing capabilities were assessed, the post-scanning analysis workflow was defined, and a protocol was established for the application of DIC. This body of work provided "proof of concept" for the subsequent experiments described in this thesis, but also yielded meaningful and applicable results.

Accordingly, Chapter 3[2] (Paper 2) takes the novel methodology from Chapter 2 and introduces FEA for validation. The agreement between the mechanical and computational analogues is also exploited to investigate the capabilities of the computer model in more detail, while looking at the effects of the excision site location on the loading patterns.

---

[1] Work presented in SIMBIO-M 2018, SAFE EUR 2017 and ESB 2016 Conferences

[2] Work presented in SIMBIO-M 2018 and ESB 2016 Conferences

3 EVALUATION OF BONE EXCISION EFFECTS ON A HUMAN SKULL MODEL – II: FINITE ELEMENT ANALYSIS

Constantinos Franceskides[1*], Michael Gibson[2], Peter Zioupos[1]

[1]*Musculoskeletal and Medicolegal research Group, Cranfield Forensic Institute, Centre for Defence Engineering, Cranfield University, Defence Academy of the UK, Shrivenham, SN6 8LA, UK*

[5]*Centre for Simulation & Analytics, Centre for Defence Engineering, Cranfield University, Defence Academy of the UK; Shrivenham, SN6 8LA, UK*

3.1 Abstract

Patient-specific computational models can be used to predict the consequences of invasive surgery on the musculoskeletal system, thus helping to improve therapeutic decision-making and post-operative care. However, the use of personalised models that predict the effect of biopsies and full excisions tends to be restricted to prominent individuals, such as high-profile athletes. We have developed a finite element analysis (FEA) model to determine the influence of the location of an ellipsoidal excision (14.2 x 11.8 mm) on the structural integrity of a human skull when exposed to impact loading, representing the free fall of an unconscious adult male. The FEA model was compared to empirical data based on the drop-tower testing of 3D-printed physical skull models where deformations were recorded by digital image correlation. The FEA model allowed meaningful conclusions to be drawn from simulations based on actual patient data in a clinically relevant timespan, indicating that the approach is not only clinically beneficial but also cost-effective, potentially allowing such models to be used more widely. We found that the excision site did not have a major effect on the calculated stress and strain magnitudes unless the excision was in the temporal region, where the reduction in stiffness around the excision caused failure within the neighbouring area.

Keywords: Biopsy; Skull fracture; Strains; Digital image correlation; Impact loading; FEA

3.2 Introduction

The increasing capacity for computed tomography (CT) and magnetic resonance imagining (MRI) in the oncology services industry has led to a steady growth in the number of screenings per year (Table 3-1).

Table 3-1 Annual growth in screening procedures. CT = computed tomography; MRI = magnetic resonance imaging; Pet-CT = positron emission tomography–computed tomography.

Year	Total growth %	CT	MRI	Pet-CT
2013/14	5.1	13.0	11.3	5.9
2014/15	4.9	11.1	10.5	18.5
2015/16	2.1	6.2	6.7	9.9
2016/17	0.9	5.1	6.1	32.5
Average	3.3	8.9	8.7	16.7

In turn, the number of cancer diagnoses has increased, and patient survival has improved (Magadia, et al., 2016), with the combined death rate in men and women falling 23% from its peak in 1991 to 2012 (National Institutes of Health, 2017). Where biopsies or excisions are required, personalised models (in either physical or computational form) that predict the outcome of surgery are rarely employed because of the drain on public healthcare resources. Such models are usually considered only for prominent individuals such as high-profile athletes. However, recent technological advances have raised the prospect that such personalised approaches could be based on data routinely obtained during screening, such as pre/post-operative CT scans, which could then be exploited to create computational and mechanical models that predict patient-specific outcomes. One modelling approach that has been demonstrated successfully in this context is finite element analysis (FEA), which subdivides a large problem into simpler parts (finite elements) that can be solved before reassembling them into a larger model of the entire problem.

Knowledge gained from the application of FEA techniques to cellular composite structures, and specifically the mechanical properties of bones, has highlighted the utility of such a modelling approach [(Verhulp, et al., 2008); (Bevill & Keaveny, 2009)]. Although it is important to point out that some assumptions were made, such as bone structures being regarded as homogenously porous structures because the structural characteristics were not easily determined, such tools still offer the ability to solve loading problems incorporating complex morphologies. For example, numerical simulations have been carried out to investigate three-point bending of the frontal part of the cranium [(Rahmoun, et al., 2014) ; (Boruah, et al., 2013)], where the internal morphology was simulated by introducing voids in anisotropic and isotropic models. When modelling skulls, a typical approach is to investigate their mechanical properties to optimise analogue or alternative structures corresponding to the actual elastic and/or plastic responses of human bones [(Falland-Cheung, et al., 2017); (Garcia-Gonzalez, et al., 2017)]. This added level of complexity is not considered here because the model skulls are replicas and we focus on the effect of surgical intervention in terms of comparative load dissipation. As the memory and processing capacity of computers increases, more detailed and biofidelic finite element models can be developed and solved within practical timescales.

A recent preliminary study tested the skull of a 28-year-old male patient *in silico*, based on clinical CT scans (Gibson , et al., 2016). Experimental data for the impact loading of the same skull are reported in our accompanying report (Chapter 2), which involves the drop-tower testing of physical models produced by 3D printing, followed by digital image correlation (DIC) (Franceskides, et al., 2017). The drawback of any experimental study is that it is destructive, and it can be repeated only for a small number of samples assuming the ability to replicate the boundary conditions. In contrast, FEA models are non-destructive, they allow a test to be repeated infinitely under diverse conditions, and they reproduce the results for any structural problem on a global scale (strain can be read and predicted at any part of the structure) not just locally (DIC and extensometry are always site specific).

Here we examined the behaviour of an *in silico* skull model under load testing, with lesions in different places but a common impact site. We re-examined the constraint methodology and then determined the ability of FEA to predict the behaviour of the 3D-printed models. We used DIC to study the empirical load dissipation and stress concentration, reflecting the precise excision location, and coupled this to local FEA data obtained during the impact. We then used the model to predict the outcomes for different sites on the skull, and thus we exploited the versatile predictive capability of the FEA modelling approach compared to DIC.

3.3 Materials and methods

3.3.1 The patient

The fabricated skulls used in this study were modelled on the case of a 28-year-old male patient with no previous history of musculoskeletal disorders and no prior bone tissue surgery. The excision to the occipital skull region was performed by a consultant neurosurgeon at Wellington Hospital, London, UK. The patient was otherwise healthy. Ethical approval for the work was granted by the relevant Cranfield University committee and the patient consented under the approval reference CURES/787/2016.

3.3.2 Design of the *in silico* skull models

The *in silico* skull models were based on the same post-operative clinical CT scan described in Chapter 2, which was acquired at a resolution of 0.488 x 0.488 x 1.2 mm and at 120 kV and 400 mA (Figure 3-1, step 1) (Franceskides, et al., 2017).

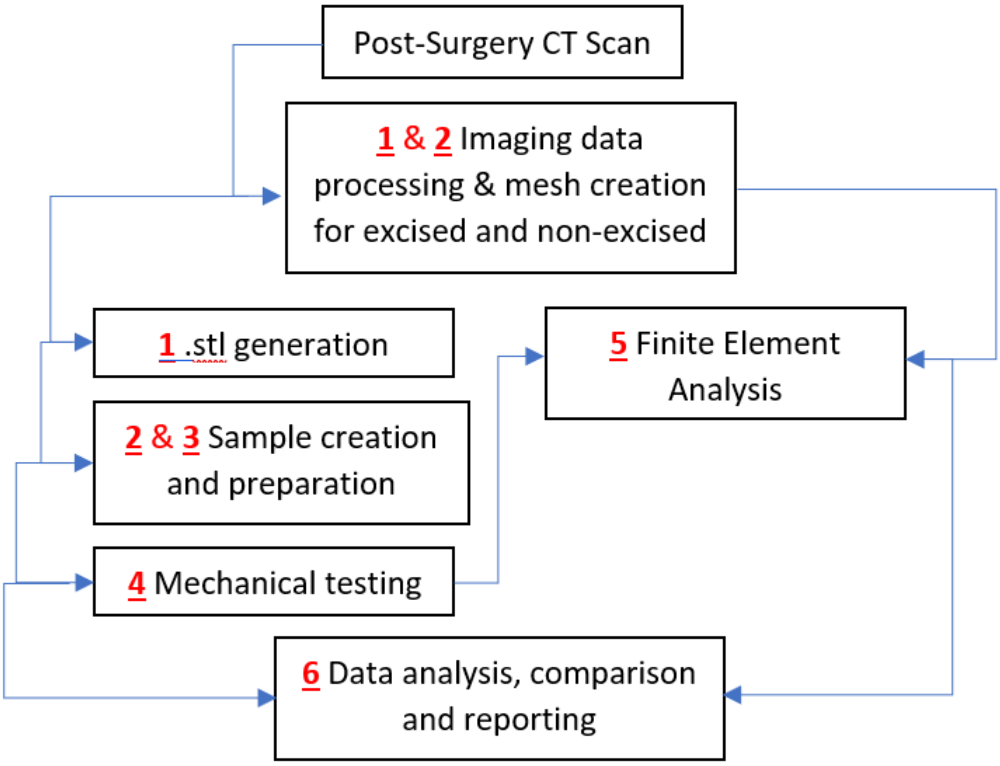

Figure 3-1 Combined methodology flow diagram. 1. Create 3D geometry of the skull plus excision based on patient's CT scan data; 2. Duplicate 3D model and fill the excision site to approximate the pre-operative state; 3. Create 3D models and accompanying meshes for various excision sites; 4. For each of the two 3D geometries: a. Create 3D-printed replicas of the excised and non-excised skulls using ABS. b. Mechanically test the 3D-printed replicas from point 2. c. Simulate impact of the drop hammer, considering the peak load as quasi-static. d. Compare FEA to mechanical testing. e. Re-run FEA to investigate the effect of different excision sites.

Five skull geometries were created: the "original" model with a lower occipital excision, a "healthy" control with the excision filled in, and three variants with the excision moved to the parietal, frontal or temporal region (Figure 3-1, step 2). All scans were imported to Simpleware ScanIP v7 as a 32-bit float, but were converted to an 8-bit float and resampled (using the cubic function) to match the voxel axial dimension to the in-plane dimension with the resulting cubic voxels of side length 0.488 mm. A series of masks was then applied, with the appropriate grayscale thresholding and flood fill operations to select only bone matter within the scanned volume. The resulting model was passed through a Gaussian smoothing filter to better represent the actual skull geometry (voxel-based output from CT scanners is dependent on the slicing interval, thus creating a stepped appearance). Further cavity-fill and morphological operations were conducted before exporting the model .stl file.

The “healthy” skull geometry was created using the neighbouring morphology, such as the surrounding bone thickness and curvature, thus mimicking as closely as possible the pre-operative condition of the region. The “original” skull model with the lower occipital excision was used to create the remaining geometries with alternative excision sites by first creating an intermediate skull with the excision patched, and then duplicating the geometry of the excision by subtracting the initial skull geometry from the initial patch geometry. This excision segment could then be moved to any point on the intermediate skull to create a new excision site. The tapering of the excision remained constant with respect to the excision diameter of 14.2 ± 0.5 mm, thus eliminating thickness variations at the different excision sites.

3.3.3 Preparation of the physical skull models

Six skulls were printed in acrylonitrile butadiene styrene (ABS) using a fused deposition modelling (FDM) Stratasys UPrintSE 3D printer (Figure 3-1, step 3). The .stl files were imported into the CatalystEX proprietary software, which was used to create the .cmb tool-path files to control the printing process. Support fill was set to ‘smart’, the model interior to ‘solid’ and the layer resolution to 0.254 mm. The printing of each model was completed in ~42 h and required almost a full reel of ABSPlus-P430 material (33 cubic inches). The freshly printed skulls were placed in a Support Cleaning Apparatus 1200 and washed with a cleaning solution containing sodium hydroxide (WaterWorks) at 70°C for 2 h to dissolve any remaining support material. Perma-Gel was used to fill the models in order to mimic the properties of the brain and reproduce its energy absorption and response. A random speckle pattern was then applied to make the surface of the skull univocally identifiable [(Vassolera & Fancelloa, 2012); (Lecompte, et al., 2006); (Pan, et al., 2010)]. The black-to-white ratio was kept as close as possible to 1:1, and Castrol White Contrast Paint 710 (2386) non-strippable aerosol was used to apply the high-contrast background evenly over the model surface. Finally, the size of the speckles was determined using the following equations [(Palanca, et al., 2015); (Michael, et al., 2009)]:

Equation 3-1
$$S_{ideal} = \frac{4 \pm 1}{M} \qquad (1)$$

Equation 3-2
$$M_{factor} = \frac{n_{length\ sensor\ pixels}}{d_{length}} \qquad (2)$$

The ideal speckle pattern size is expressed as 3–5 pixels divided by the magnification factor *M*, i.e. the ratio of the number of pixels along the length of the sensor to its physical length.

3.3.4 Drop tests

All six skull models were subjected to a load on the occipital region mimicking the effect of an unconscious or incapacitated human falling backwards and striking this region on a hard surface. An Imatek IM10 drop tower was used to deliver the impact with a total carriage and striker mass of 2.91 kg (Figure 3-1, step 4). The 45-mm circular titanium striker was fitted with a dampening surface adapted from a Humanetics Hybrid III headform thickness of 12.7 mm with 43 ± 5 Shore hardness ‘A’ to provide a dampening effect (smoother ramp rate) similar to the soft tissues surrounding a real human skull. Images were captured using two V12.1 Phantom high-speed cameras recording at 15,000 fps, controlled by PCC standalone software.

The data were analysed by DIC using GOM software with quadrangle facets at 19 pixels (size) and 17 pixels (step), 484 3D points generated over 176 stages, and an average intersection deviation of 0.0150 mm. Artificial lighting was provided by three light sources: two conventional halogen lights with focal adjustment, and a light emitting diode (LED) Cree floodlight acting as a background source. Due to space limitations, the LED source was reflected onto the object using a flat mirror placed outside the impact area. Two series of tests were conducted, with striker velocities of 8 m/s at 100 J and ~9.75 m/s at 130 J. The lower-energy impacts were used to determine the loading response and the higher-energy impacts were used to induce failure in the skulls and thus determine the fracture pattern and propagation path.

3.3.5 Finite element modelling

The five skull geometries described earlier were used to create the volumetric meshes required for FEA. These differed from the previously generated surface meshes (.stl files) in that the volume of each skull was divided into a relatively large number of small, geometrically simple, polyhedral elements (typically tetrahedra and hexahedra). ScanIP has two principal methods for generating meshes, *FE-Free* and *FE-Grid*. The former creates a free-form mesh of defined geometry, whereas the latter maps cubic (perfect hexahedral) elements directly onto the voxels defined by the scan, typically generating a much higher element count. The *in silico* models generated for the purposes of this investigation were meshed using the *FE-Free* method, setting the mesh refinement to –20 (a setting within the mesh refining tool of ScanIP). Some functions within the mesh refinement protocol is node interface density, void elimination and element size alteration. The meshes were then exported individually as .cdb files. An example of such a mesh is shown in Figure 3-2, rotated to show the excision site.

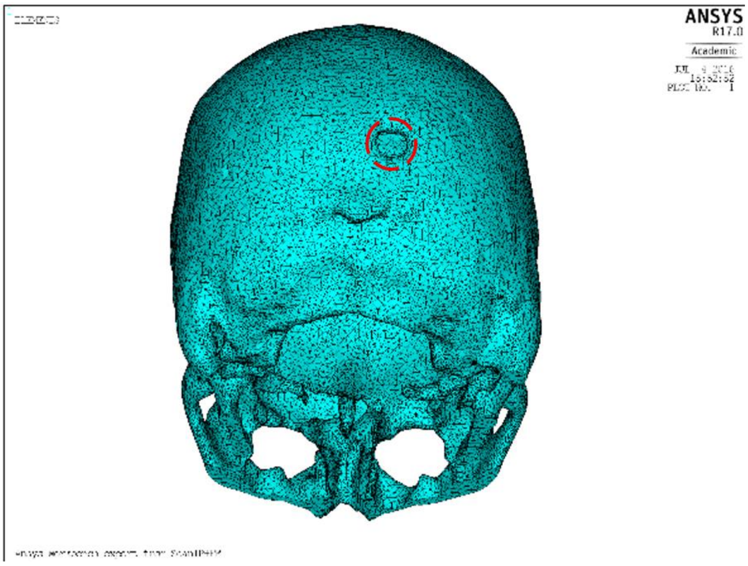

Figure 3-2. Sample skull mesh used for the finite element model.

3.3.6 Simulation

The static, structural simulations of the drop-tower test were conducted using ANSYS Mechanical APDL v17.1 FEA software. The FEA models were created by importing the meshes (see above) and applying the appropriate material properties, loads, constraints and solution settings to best match the experimental conditions, as previously reported for similar loading scenarios, impactor velocities and impact energies (Asgharpour, et al., 2014). During the modelling phase, the loading was considered to be quasi-static within the FEA model and was applied uniformly over the striker impact area on the rear of the skull, offset to the occipital lobe, with the load set as equal to the peak striker force measured experimentally. Two main constraint areas were selected: (1) the surface of the face, primarily to restrain forward motion, and (2) the lower surface of the skull. Each of the five skull variants was constrained and loaded in the same manner such that only the mesh varied. A constant impact force was applied, equal to the peak recorded impact force of the empirical tests, i.e. ~10,000 N as previously reported [(Asgharpour, et al., 2014); (Pinnoji & Mahajan, 2007)]. To estimate the associated duration of impact, the change in momentum of the striker was equated to the impulse applied to the skull, as shown in the following equation with F representing the force, m the mass, Δv the velocity change, I the impulse and t the time:

Equation 3-3

$$I = m\Delta v = Ft \qquad (3)$$

Therefore, assuming a constant deceleration force, the duration of deceleration may be estimated as follows:

Equation 3-4

$$t = m\Delta v / F \qquad (4)$$

which resolves to:

Equation 3-5

$$t = \frac{2.91\ x\ 4.6}{10000} = 0.00134 \text{ s} = 1.34 \text{ ms} \qquad (5)$$

The high-speed video used during the experimental portion of this investigation was recorded at 15,000 fps. Impact lasted ~25 frames (1.67 ms) indicating that the force applied was consistent with the represented change in momentum. The average force recorded during impact was somewhat lower than 10,000 N, which accounts for the discrepancy between the theoretical and actual force durations.

The ABS material was not expected to shatter when struck, but it was expected to undergo plastic deformation with little strain hardening (Newman & Williams, 1978). Accordingly, a bilinear, kinematic material model was used to represent it. The material properties required by the model, and the corresponding values used in this investigation, are listed in Table 3-2.

Table 3-2 Material specifications of acrylonitrile butadiene styrene (ABS). Values for Young's modulus and yield stress were supplied by Stratasys Ltd.

Property	Value
Young's modulus (E)	2200 MPa
Poisson's ratio	0.3
Yield stress	31 MPa
Plastic modulus	E/1000 = 2.2 MPa

The front face of the skulls was constrained in a distributed, flexible manner, to represent the PermaGel restraint block in the mechanical tests. The flexible constraint was achieved by applying a large number of spring elements (typically ~14,800) over the constrained surface, the first nodes of which were shared with a node on the face of the skull mesh, whereas the other end was fully constrained. Each spring element had a stiffness of 0.62 N/mm and an initial length of 5 mm. The lower surface of the skulls was constrained vertically, preventing rotation about the anterior-posterior and medial-lateral axes. The skull was therefore restrained during impact without causing localised stress concentrations, allowing the applied impact load to replicate a moving skull striking an obstacle. Each analysis was broken down into 10 load steps, each initially configured to solve with three sub-steps and with upper and lower limits of 15 and 2 sub-steps, respectively.

3.3.7 Comparison of experimental and FEA model data

The response of the FEA model was assessed against that of the ABS analogue by comparing three metrics: (1) impact site displacement; (2) maximum and minimum proximal excision strains; and (3) the crack initiation site. Additional trends among the FEA models of the different excision sites were assessed by comparing force, stress and strain data on a local and global basis.

3.4 Results and discussion

3.4.1 FEA mesh sensitivity

Global and near-excision peak stress data for the occipital excision are plotted in Figure 3-3.

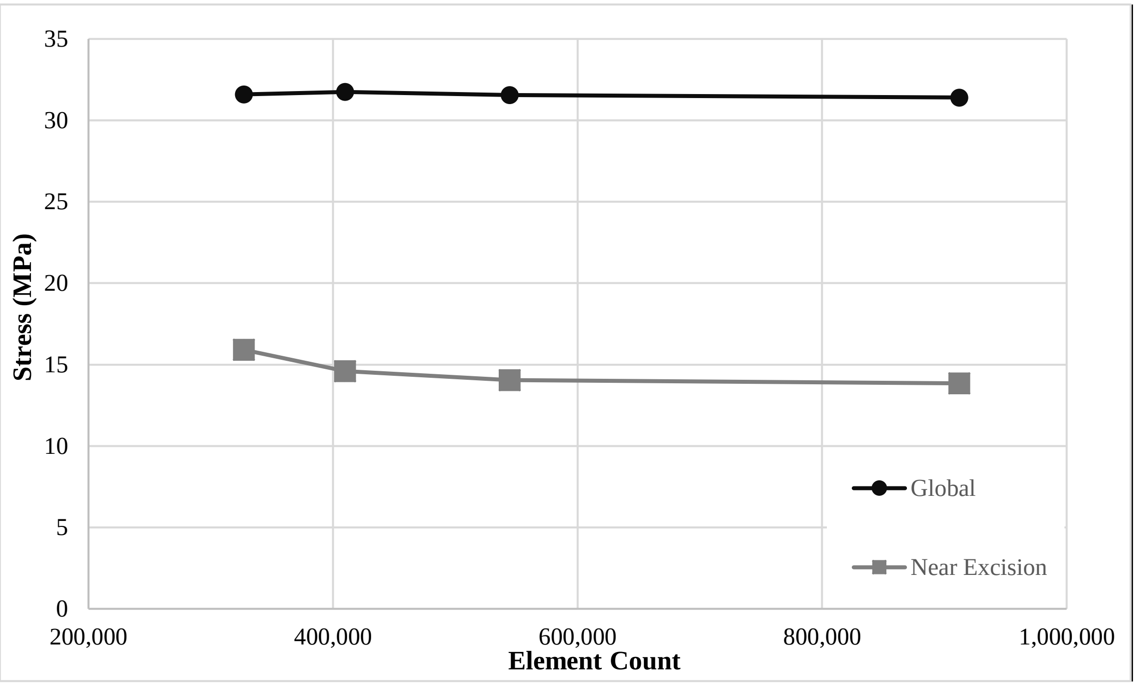

Figure 3-3. Global and near excision peak stresses within the skull FEA model, revealing the sensitivity of the elemental count.

Overall, the stress patterns and global peak stresses were very similar between meshes, whereas the near-excision stresses showed more mesh sensitivity. Accordingly, element-size sensitivity analysis was conducted based on the peak near-excision stresses. This revealed that the ~500,000 element mesh generated sufficiently similar results to the ~900,000 element mesh, and the model was therefore considered to be mesh-insensitive beyond that point. The ~500,000 element mesh corresponded to a refinement value of –20 within the ScanIP *FE-Free* meshing algorithm.

3.4.2 Comparison of impact site displacements

The displacement of the two sets of skulls (excised and non-excised) in response to impact loading was compared between the mechanical model (DIC data) and the FEA model (Figure 3-4).

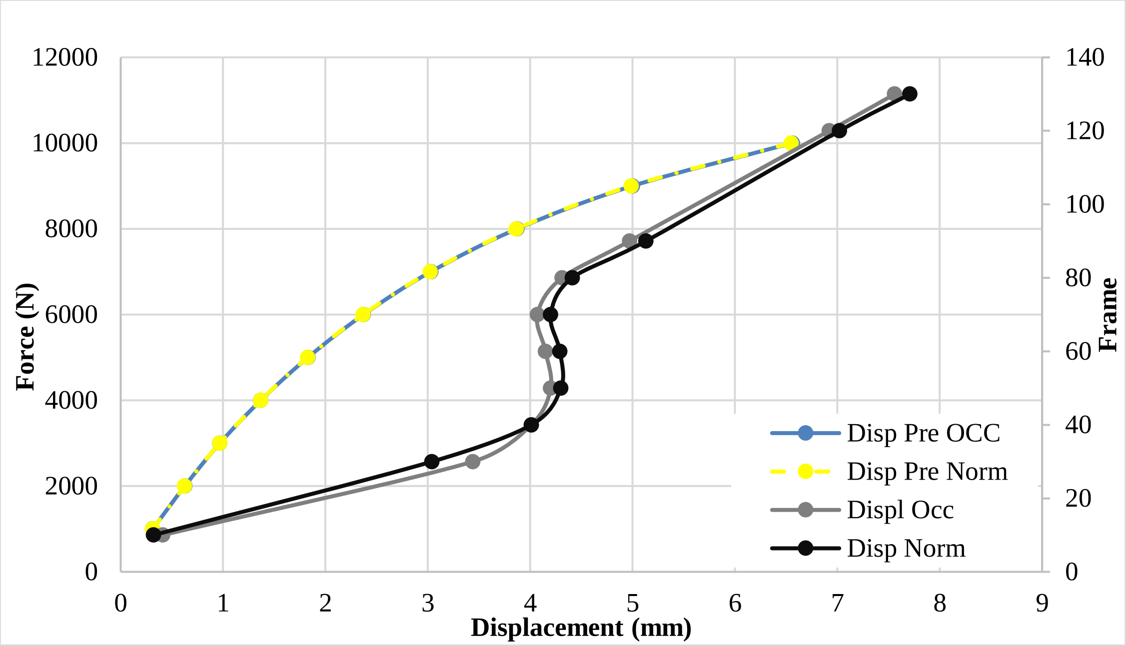

Figure 3-4 Comparison of force against displacement and frame sequence of excised (occipital) and non-excised skulls for both FEA and DIC data.

The FEA data were extracted as the mean displacement of the impact site in response to the applied impact load, whereas the DIC data were extracted from incidence displacements (of the skull) in the associated frame sequence of the impact site.

The FEA model showed a smooth displacement curve, with a gradual transition from an initially linear relationship to non-linear as yielding occurred at particular locations. In contrast, the DIC displacement curves showed some variation, probably reflecting non-ideal aspects of the model such as skull placement, test rig errors and viscoelastic effects of the PermaGel block. The notable delay between frames 40 and 70 (Figure 3-4) predominantly represents the energy absorbed by the skin simulant adhered to the impactor.

Plotting displacement against frame (indirect time) yielded a much more coherent result than displacement against load (force) because the load in this case is the load from the crosshead instead of the load experienced on the skull. The FEA and DIC data showed significant variation during the initial stages of the curves, again probably due to the inability of the model to replicate the properties of the skin simulant on the impactor. However, once beyond the initial compaction stage, there was much greater conformity.

When comparing the maximum displacements in the normal skulls and those with occipital excisions, FEA and DIC showed displacement variation of no more than 15%.

3.4.3 Comparison of excision-proximal strains

In contrast to the displacement results, the von Mises strain comparisons (Figure 3-5) revealed greater variation between the DIC and FEA techniques.

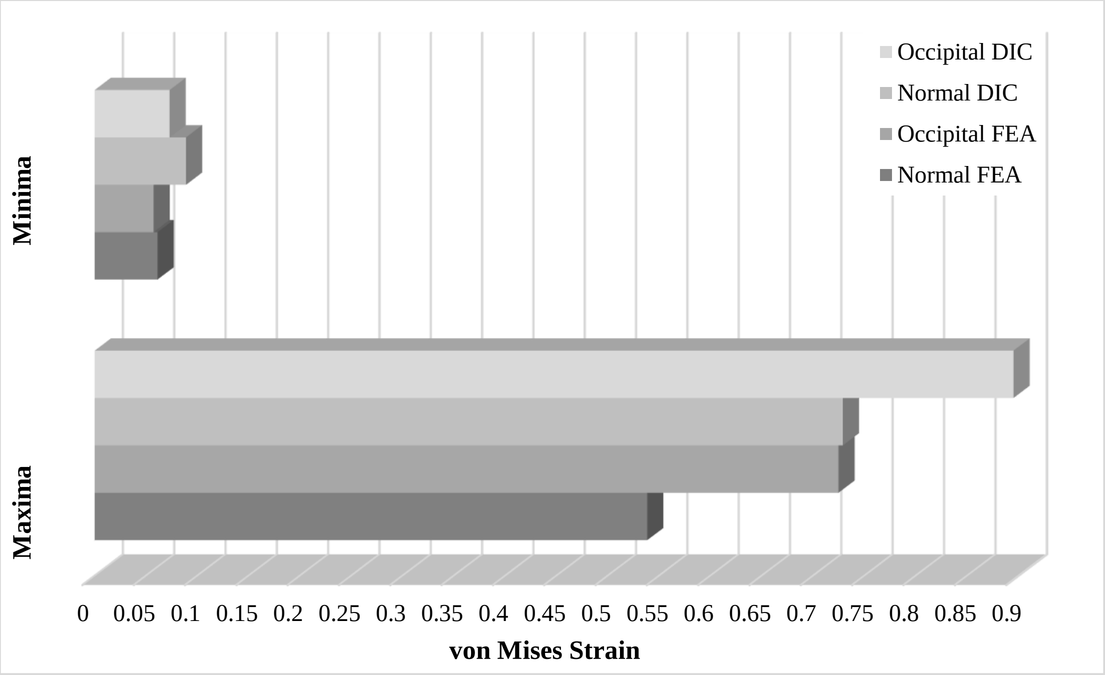

Figure 3-5 Comparison of proximal von Mises strain in normal skulls and those with excisions, following DIC and FEA analysis.

This was anticipated, because the FEA model does not account for moments of inertia effects or thermal softening. In addition, FEA data are based on volume analysis whereas DIC can only record surface strain. Nevertheless, the behavioural trends between the two skulls were clear, with an almost 20-fold difference between the maxima and minima. These data indicate that the excised skull experiences greater strain than the healthy skull.

The above data agree with previous research conducted on the outer cortical layer of adult human calvariums (Boruah, et al., 2017), where the effective failure stress and strain are related to skull position, whereas the bone modulus is related to the calvarium bone quality.

3.4.4 Comparison of crack initiation sites

On the lower edge of the occipital excision site, the localised von Mises stress was ~15.7 MPa compared to only ~11.8 MPa in the same region of the healthy skull. This result indicated that the excision increases the regional stress but does not affect the overall strength of the skull. The results from the 500,000-element FEA mesh were compared with empirical equivalents, revealing that the areas of plasticity within the FEA model correlated accurately with the regions that had cracked within the printed skull, including crack initiation at the lower edge of the occipital region on the impact side (Figure 3-6).

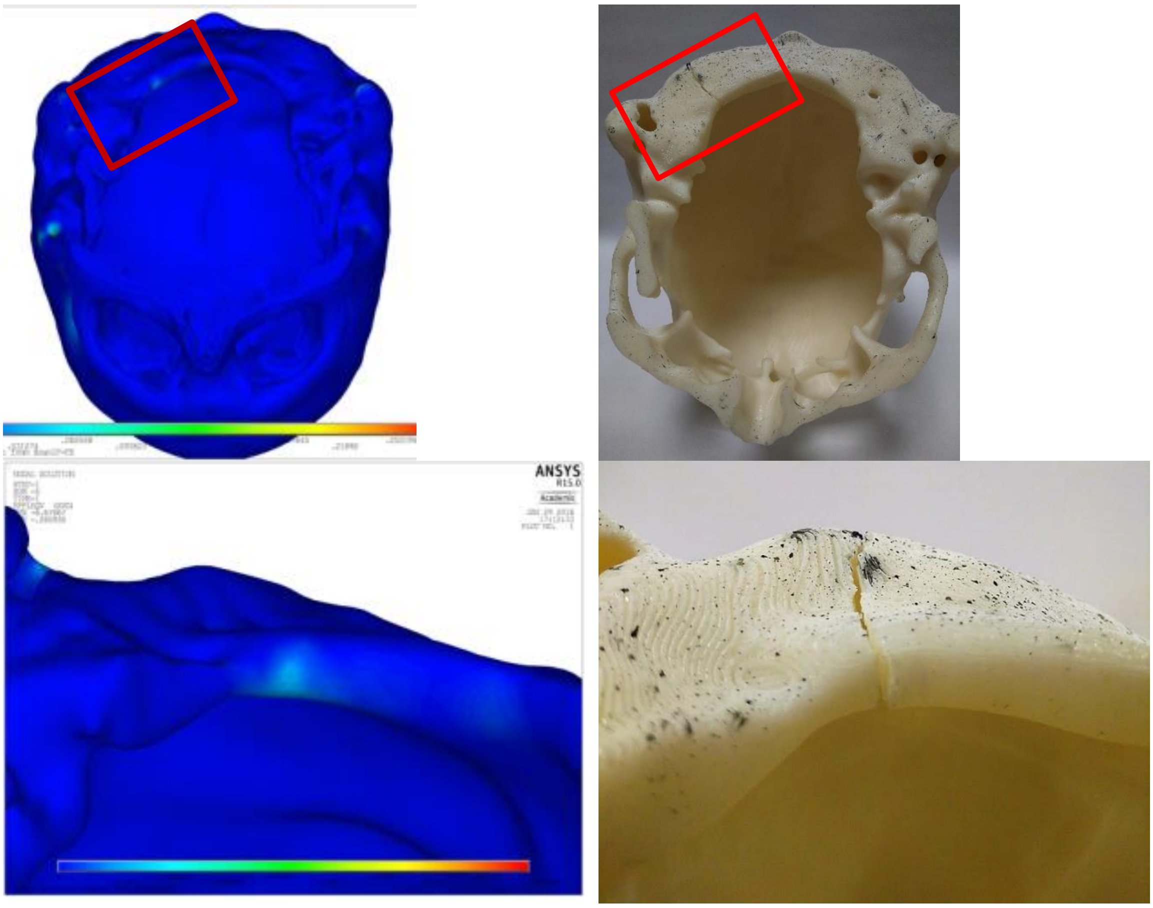

Figure 3-6 Maximum plastic strain in the FEA model compared to the failure site in a 3D-printed skull, highlighting the similarity of outcomes.

The FEA simulation predicted the behaviour of the printed ABS skull within the elastic region and revealed moderate degrees of plasticity, but once a crack initiated the simulation became less accurate and stress continued to increase with strain, albeit at a low modulus. The printed ABS medium also included a degree of laminar behaviour which was not replicated in the FEA model.

3.4.5 Comparison of stress and strain

The maximum excision-proximal stress at the frontal, parietal and temporal excision sites was consistently similar in magnitude, whereas less stress was experienced at the occipital excision site and the least stress was experienced by the intact, healthy skull (Figure 3-7).

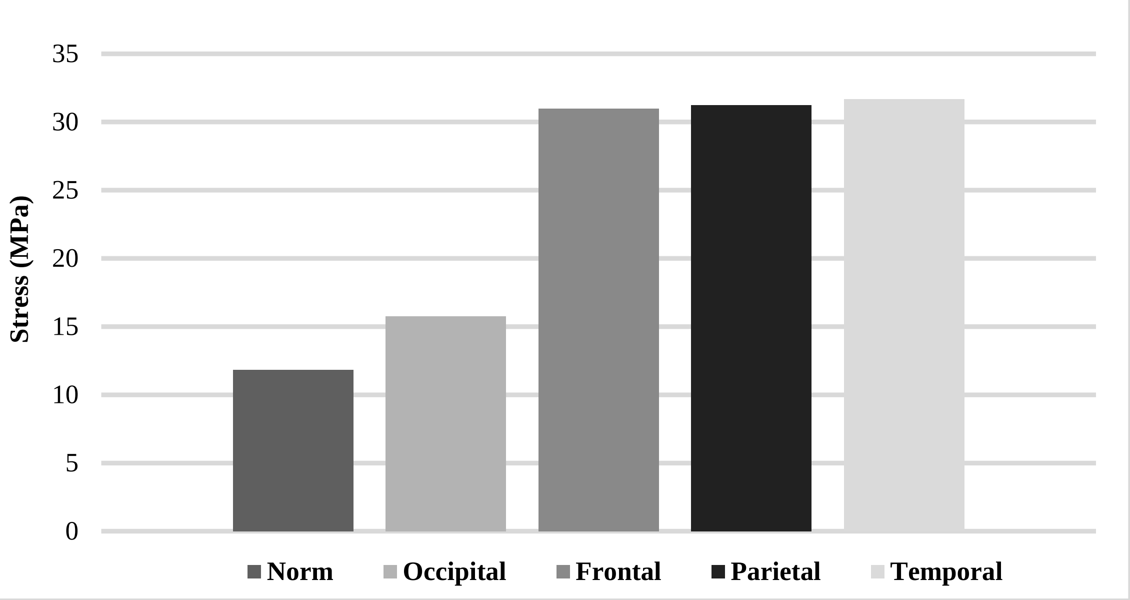

Figure 3-7 Maximum excision-proximal von Mises stress at the different excision sites.

However, the maximum excision-proximal strain was highest by far for the temporal excision, with the other skulls showing much lower values (Figure 3-8).

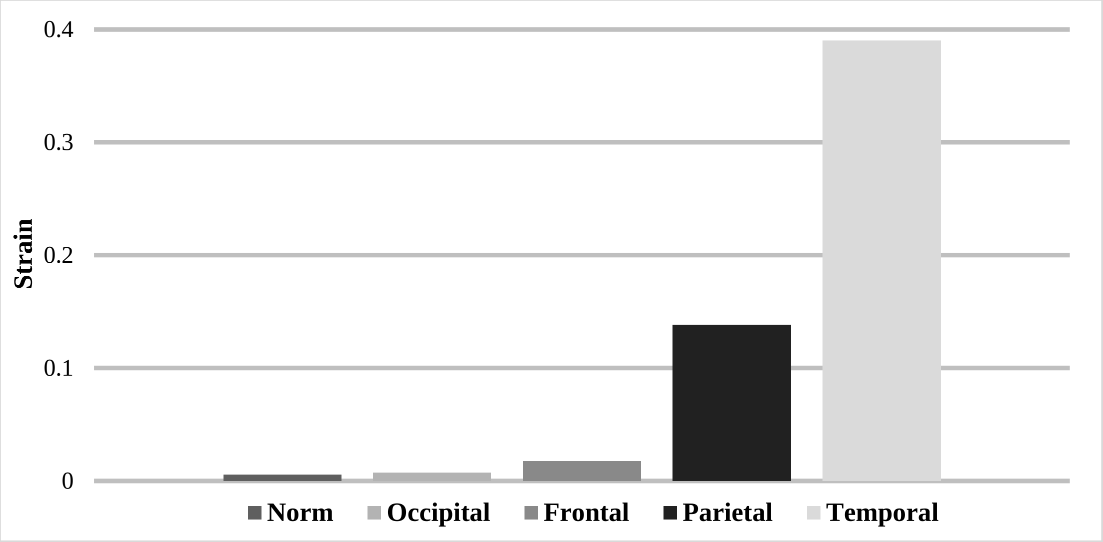

Figure 3-8 Maximum excision-proximal von Mises strain at the different excision sites.

This may reflect the relatively thin bone surrounding the temporal excision, whereas the other excisions feature much thicker peripheral bone. The profiles of global mean strain (Figure 3-9) and global mean stress (Figure 3-10) were similar to the maximum strain, with the temporal excision showing the highest values and the other four models showing lower values but with the same ranking: parietal, frontal, occipital, normal.

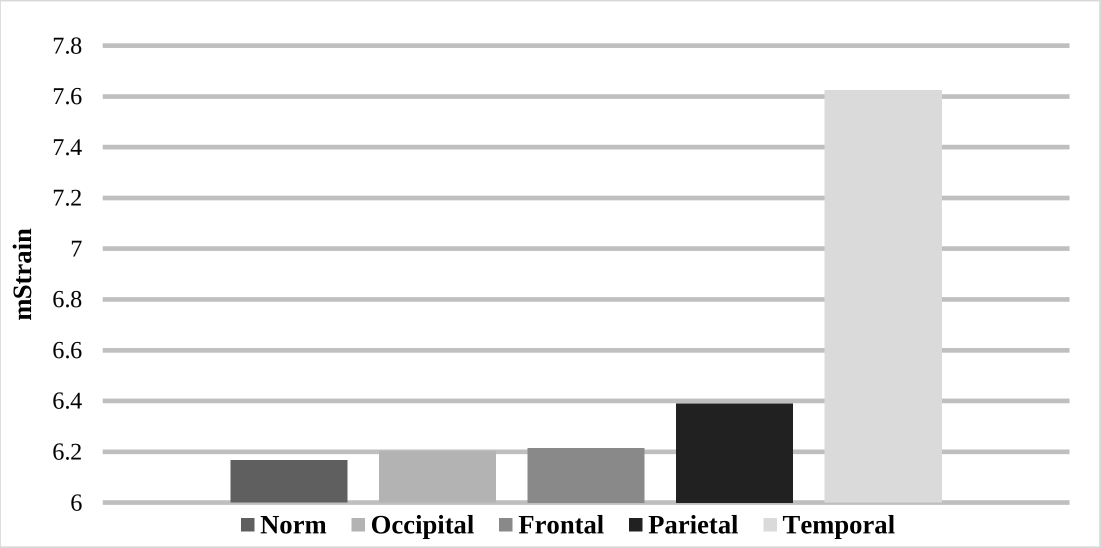

Figure 3-9. Global mean von Mises strain at the different excision sites.

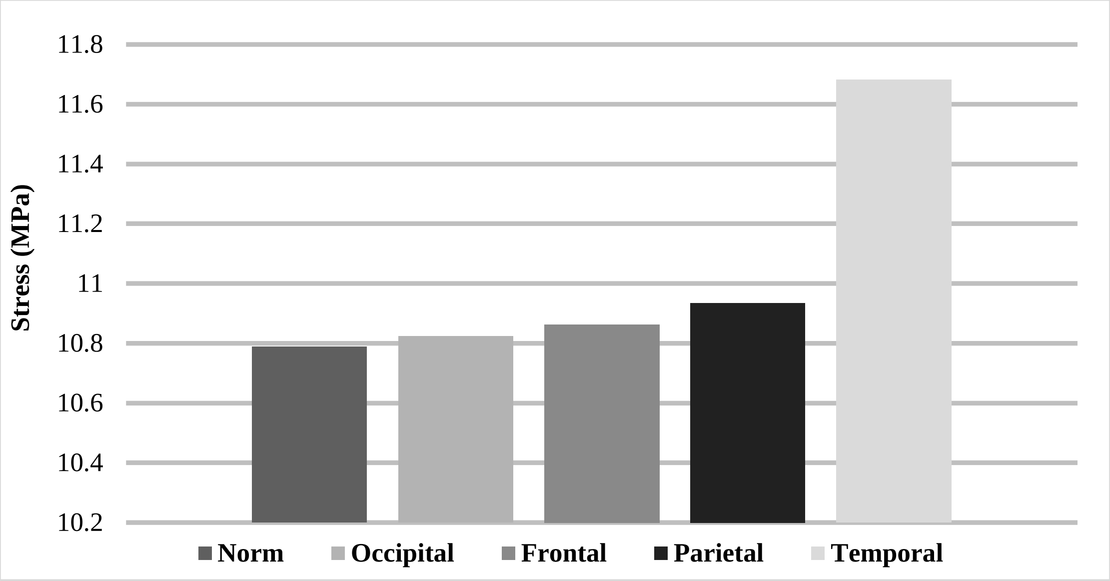

Figure 3-10 Global mean von Mises stress at the different excision sites.

The unique behaviour of the temporal excision may again reflect the relative thinness of the skull in that region, in sharp contrast to the lowest levels of regional and global stress and strain observed in the normal, healthy skull.

3.5 Conclusions

Our comparison of DIC and FEA testing methods indicated strong agreement between the two approaches, but there remains a degree of discordance which should be addressed by further model refinement. General properties, such as stress concentration and crack initiation sites, were easily identified by FEA and compared well with the mechanical counterparts. Furthermore, the displacement data were largely concordant, highlighting similarities between the trends observed in the normal skulls and those with excisions. The surgery on the patient does appear to have influenced the propagation and distribution of stress and strain as well as the mechanical response of the skull. Moreover, the hole created during the bone biopsy increased stress in the surrounding region, but not enough to induce a structural failure originating from the hole. This was confirmed in the tests involving both the FEA and DIC methods. The excision hole also experiences much greater strain concentration than the rest of the occipital part of the skull. Our research has shown that the excision location in relation to the site of impact can have a significant effect on strain magnitudes. Although our data are patient-specific, the results can be used as the basis for further research into the effect of invasive surgeries and their accompanying computer models, not only on the skull but also on the rest of the musculoskeletal system.

3.6 Acknowledgments

We acknowledge the work, skill and expertise offered by Karl Norris in the mechanical workshop of Cranfield University, and Jolyon Cleaves of Vision Research for providing the high-speed cameras. Ethical approval was granted by the Cranfield University Research and Ethics Committee (CURES). This paper is dedicated to one of the authors, Dr Mike Gibson, whose untimely death is a great loss to us all.

3.7 References

Asgharpour, Z., Baumgartner, D., Willinger, R., Graw, M., & Peldschus, S. (2014). The validation and application of a finite element human head model for frontal skull fracture analysis. *Journal of the mechanical behaviour of biomedical materials, 33,* 16-23.

Bevill, G., & Keaveny, T. (2009). Trabecular bone strength predictions using finite element analysis of micro-scale images at limited spatial resolution. *Bone, 44*(4), 579-584.

Boruah, S., Henderson, K., Subit, D., Salzar, R. S., Shender, B. S., & Paskoff, G. (2013). Response of Human Skull Bone to Dynamic Compressive Loading. Gothenburg (Sweden): IRCOBI.

Boruah, S., Subit, D. L., Paskoff, G. R., Shender, B. S., Crandall, J. R., & Salzar, R. S. (2017). Influence of bone microstructure on the mechanical properties of skull cortical bone – A combined experimental and computational approach. *Journal of the Mechanical Behaviour of Biomedical Materials, 65,* 688-704.

Falland-Cheung, L., Waddell, J. N., Li, K. C., Tong, D., & Brunton, P. (2017). Investigation of the elastic modulus, tensile and flexural strength of five skull simulant materials for impact testing of a forensic skin/skull/brain model. *Journal of the Mechanical Behaviour of Biomedical Materials, 68,* 303-307.

Franceskides, C., Leger, T., Gibson, M., Horsfall, I., Zioupos, P., & Tozzi, G. (2017). Impact of lesion excision on 3D printed human skull. *Materials Today COMMS.*

Garcia-Gonzalez, D., Yoon, S.-H., Cook, J., Siviour, S. R., Sotiropoulos, S. N., Yoon, S. H., . . . Jérusalem, A. (2017). On the mechanical behaviour of PEEK and HA cranial implants under impact loading. *Journal of the Mechanical Behaviour of Biomedical Materials, 69,* 342-354.

Gefen, A., & Epstein, Y. (2014). *The Mechanobiology and Mechanophysiology of Military-Related Injuries* (1 ed.). Springer.

Gibson, M., Franceskides, C., & Zioupos, P. (2016). Simulated Impact Response of a 3-D Printed Skull, with an Ellipsoidal Excision, using Finite Element Analysis. *22nd Congress of the European Society of Biomechanics.* Lyon: European Society of Biomechanics.

Lecompte, D., Smits, A., Bossuyt, S., Sol, H., Vantomme, J., Van Hemelrijck, D., & Habraken, A. (2006). Quality assessment of speckle patterns for digital image correlation. *Optics and Lasers in Engineering, 44*(11), 1132–1145.

Magadia, W., Exarchakoua, A., Racheta, B., Colemana, M., Jenkins, J., Bannister, N., . . . Rowlands, S. (2016). *Cancer survival in England: Patients diagnosed between 2010 and 2014 and followed up to 2015.* Office for National Statistics.

Michael, A., Orteu, J., & Schreier, W. (2009). Digital Image Correlation. In *Image correlation for shape, motion and deformation measurements.* (pp. 1-37). Springer-Verlag: Springer.

National Centre for the Replacement, Refinement and Reduction of Animas in Research. (2017). Retrieved 11 2017, from https://www.nc3rs.org.uk/the-3rs

National Institutes of Health. (2017). *Statistics at a Glance: The Burden of Cancer in the United States.* National Cancer Institute.

Newman, L. V. & Williams, J. G., 1978. The Impact Behaviour of ABS Over a Range of Temperatures. *Polymer Engineering and Science,* 18(11), pp. 893-899.

Office of Crash Worthiness Standards. (1997, April). *www.unece.org.* Retrieved 2016, from https://www.unece.org/fileadmin/DAM/trans/doc/2009/wp29/HIII_50th_Male_Drawings.pdf

Palanca, M., Tozzi, G., & Cristofolini, L. (2015). The use of digital image correlation in the biomechanical area: a review. *International Biomechanics, 3*(1), 1-21.

Pan, B., Lu, Z., & Xie, H. (2010). Mean intensity gradient: An effective global parameter for quality assessment of the speckle patterns used in digital image correlation. *Optics and Lasers in Engineering, 48*(4), 469–477.

Pinnoji, P. K., & Mahajan, P. (2007). Finite element modelling of helmeted head impact under frontal loading. *Sādhanā, 32*(4), 445-458.

Rahmoun, J., Auperrin, A., Delille, R., Naceur, H., & Drazetic, P. (2014). Characterization and micromechanical modelling of the human cranial bone elastic properties. *Mechanics Research Communications, 60*, 07-14.

Stratasys. (2015). *ABSplus-P430.* Retrieved 12 06, 2017, from http://usglobalimages.stratasys.com/Main/Files/Material_Spec_Sheets/MSS_FDM_ABSplusP430.pdf

U.S. Army Medical Research Acquisition Activity. (2014, August 6). *Notice for Ballistic Load Sensing Headform System.* Retrieved 2014, from www.fbo.gov/index

Vassolera, J. M., & Fancelloa, E. A. (2012). Error analysis of the digital image correlation method. *Asociación Argentina de Mecánica Computacional, XXIX*, 6149-6161.

Verhulp, E., Van Rietbergen, B., Müller, R., & Huiskes, R. (2008). Micro-finite element simulation of trabecular-bone post-yield behaviour – effects of material model, element size and type. *Computer Methods in Biomechanics and Biomedical Engineering, 11*(4), 389-395.

CHAPTER 4 PREFACE

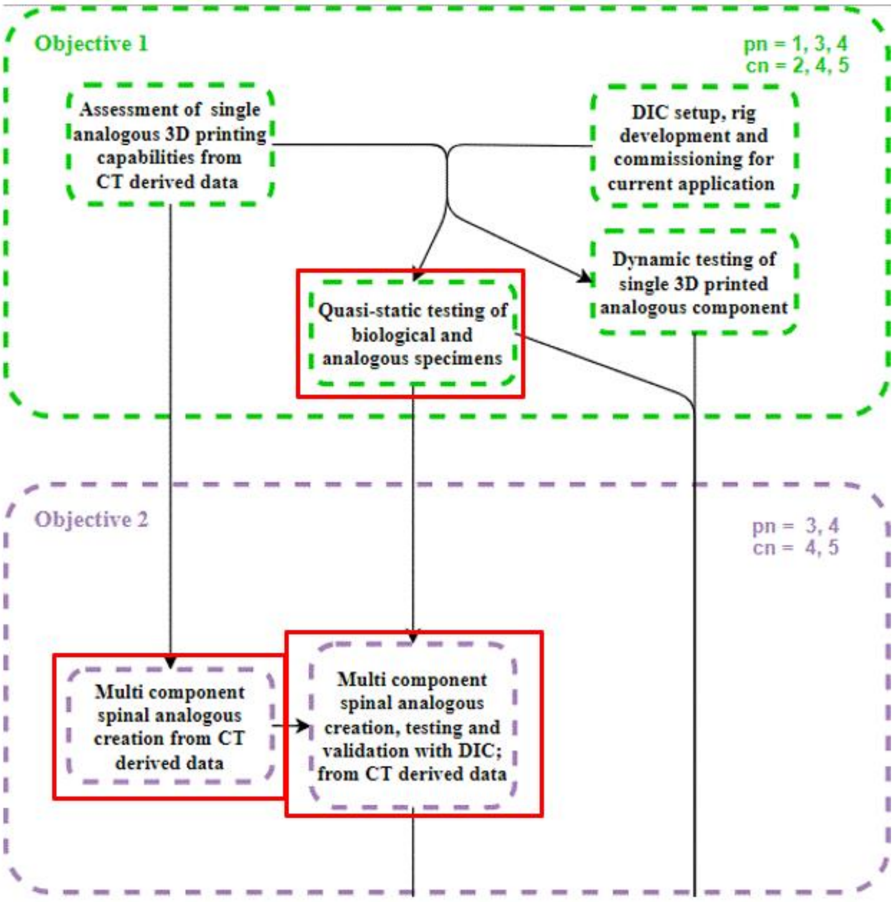

Chapter 2[3] (Paper 1) described the development of a methodology for the creation of 3D-printed components derived from the CT scans of an individual patient. The printing capabilities were assessed, the post-scanning analysis workflow was defined, and a protocol was established for the application of DIC.

Accordingly, Chapter 4[4] (Paper 3) extends the novel methodology presented in Chapter 2 by creating and testing more complex and intricate structures at both the sub-assembly and assembly levels, while changing the loading parameters from dynamic to quasi-static.

---

[3] Work presented in SIMBIO-M 2018, SAFE EUR 2017 and ESB 2016 Conferences

[4] Work presented in SAFE EUR 2017 and SAFE US 2017 Conferences

4 SPINAL MOTION SEGMENTS: CONCEPT FOR A SUBJECT-SPECIFIC ANALOGUE MODEL

Constantinos Franceskides[1*], Emily Arnold[1], Ian Horsfall[2], Gianluca Tozzi[3], Michael Gibson[4], Peter Zioupos[1]

[1]*Musculoskeletal and Medicolegal research Group, Cranfield Forensic Institute, Centre for Defence Engineering, Cranfield University, Defence Academy of the UK, Shrivenham, SN6 8LA, UK*

[2]*Impact and Armour Group, Centre for Defence Engineering, Cranfield University, Defence Academy of the UK, Shrivenham, SN6 8LA, UK*

[3]*School of Engineering, University of Portsmouth, Anglesea Road, Portsmouth, PO1 3DJ, UK*

[4]*Centre for Simulation & Analytics, Centre for Defence Engineering, Cranfield University, Defence Academy of the UK; Shrivenham, SN6 8LA, UK*

4.1 Abstract

Most commercial spine analogues are not intended for biomechanical testing. Those developed for this purpose are expensive and still fail to replicate the mechanical performance of biological specimens in their entirety. Patient-specific analogues that address these limitations and avoid the ethical restrictions surrounding the use of human cadavers are therefore required. We present a method for the production and characterisation of biofidelic patient-specific motion segment analogues that allow for biological variability. Porcine spine segments (L1–L4) were scanned by computed tomography, and 3D models were printed in acrylonitrile butadiene styrene (ABS). Four biological specimens and four ABS motion segments were tested, three of which were further segmented into two vertebral bodies (VBs) and an intervertebral disc (IVD). All segments were loaded axially at 0.6 mm/min (strain rate range 6–10×10^{-4}/s). The artificial VBs behaved like biological segments within the elastic region, but the stiffness of the best two-part artificial IVD was ~15% lower than that of the biological IVDs. High-speed images recorded during compressive loading allowed full-field strains to be computed. During the compression of motion segments, IVDs experienced greater strain than VBs as expected. Our method allows the rapid, inexpensive and reliable production of patient-specific 3D-printed analogues by comparing them with biological motion segments.

Keywords: Spine; Bone analogue; Micro-CT; 3D printing; Digital image correlation (DIC)

4.2 Introduction

Patient-specific analogues are needed in the modern fields of forensic and injury biomechanics because human cadaver specimens are variable and difficult to preserve for biomechanical testing [(Wilke, et al., 1996); (Palanca, et al., 2016)] and their use is subject to stringent ethical considerations (Smit, 2002). Accordingly, mammalian quadruped spines or spine analogues are used instead. Several anatomically-correct spine analogues are currently available, but most are not intended for biomechanical testing. They are used for training, for drilling and implant fixation trials, and to demonstrate the range of motion by handling and manipulation.

Replicating the mechanical behaviour of real spines is particularly important in relation to fixing and testing implants. Standardised tests, such as ASTM 1717, simply fix implants on blocks of material generally constructed from ultra-high molecular weight polyethylene (UHMWPE) without a ‘spine segment’ being present in parallel with the construct. These approaches are intended for use with both static and dynamic implant testing but make no attempt to evaluate the implants under loading in the presence of a spine (matching the *in vivo* environment) and without any replication of the shape architecture and geometry of the vertebrae in the experimental design. For example, although standardised test methods have been suggested for the reproducible comparison of stiffness or strength of implants, it is doubtful whether these are indicative of the *in vivo* behaviour of the spine (ASTM, 2015).

The biofidelity of the standard testing environments should be improved to allow the comparison of devices for orthopaedic applications. Usefully, a few commercially available spine analogues are similar both anatomically and biomechanically (range of motion) to human cadaveric spines. The Sawbones (www.sawbones.com) Biomechanical Spine (generic, non-specific model) is available as a full section (T12–sacrum), a small section (L2–L5) or a single motion segment (L3–L4). The vertebral body is a smoothed block and makes no effort to replicate the internal structure of the bone (Sawbones, 2012). Spinal implants have previously been tested using this device as an alternative to human or animal cadavers (Wang, et al., 2014). Its advantages include the low variability of the model and the long testing life, but limiting factors include the cost, lead time (process time), and lack of patient specificity. In addition, any destructive testing such as the installation of implants cannot be reversed. There is also a commercial option to order a patient-specific analogue, but this is even more expensive and only replicates the spine shape and form, not its properties.

A more accessible spine analogue is consequently needed to make biomechanical testing available readily, regularly and at a lower cost. The analogue model proposed in this paper is patient-specific and was produced from micro-CT (computed tomography) data by generating a 3D model of the vertebrae in acrylonitrile butadiene styrene (ABS). The intervertebral disc (IVD) was constructed using topographical data from the endplates. Once the distance between the endplates was determined, liquid polyurethane was injected to form the IVD. Both biological and analogue segments were mechanically tested by axial compression. Stiffness was calculated from the linear elastic region of each section based on data from both a virtual and actual extensometer. Surface displacements and strains for each segment were determined by digital image correlation (DIC). The novel and accessible protocol and equipment used to create this 3D-printed analogue model can easily be applied in future research projects focusing on the prediction and modelling of bone behaviour.

4.3 Materials and methods

A porcine spine (from a specimen less than 12 months old, intended for the food supply chain) was obtained from a local butcher. Four motion segments (L1–L5), i.e. two vertebral bodies with their adjoining intervertebral discs from the lumbar region, were prepared from this material. Porcine spine samples were chosen because they are already deemed suitable substitutes for human cadavers and are similar both in anatomy and biomechanical properties [(Busscher, et al., 2010); (Dath, et al., 2007)]. From the fresh spine, we measured the Shore hardness (Shore & Shore, 1930) of an intact IVD (lateral to medial) and a sectioned IVD (superior to inferior), giving values of 63.2 (14 sample size, 8.4 standard deviation) and 72.7 (10 sample size, 7.4 standard deviation), respectively. These results led to the choice of the silicone, which was a two-part polyurethane with Shore A hardness 70 (PT Flex 70, www.polytek.com).

Three motion segment samples were sectioned to each produce two VB samples and one IVD sample, and one motion segment was left intact (Figure 4-1).

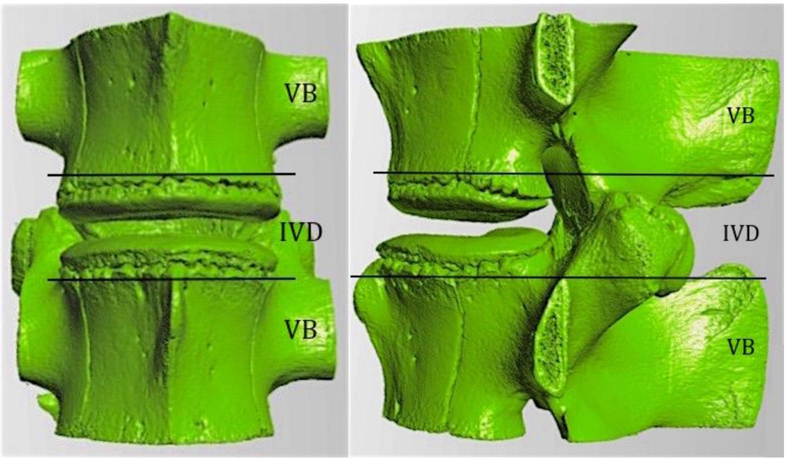

Figure 4-1 Motion segments were studied and optimised in three parts. Tissue samples were sectioned at the levels indicated above to produce three specimens: two vertebral bodies (VBs) and one intervertebral disc (IVD) from each motion segment. (a) Anterior view. (b) Lateral view.

Part of the pre-CT sample preparation involved placing samples into a water bath to remove any external tissue. Biological VBs 1–4 were immersed at <60°C for 90 min, which had little to no effect on bone properties and thus compressive stiffness [(Zioupos, et al., 1999); (Roberts, et al., 2002); (Lott, et al., 1980)]. Biological VBs 5 and 6 were immersed at ~80°C for 16 h to determine if there was a noticeable change in bone properties.

The IVDs were sectioned within the endplate to ensure the disc was intact. All unnecessary tissue was then removed. The superior and inferior planes of both the IVD and VB samples were then ground on a polisher with constant cooling to produce parallel surfaces for mechanical testing. The whole and sectioned motion segment samples were scanned (0.0412 mm at 70 kV and 90 µA) in a Nikon Metrology XT H225 CT-scanner and reconstructed using CT Pro 3D (www.nikonmetrology.com/en_EU).

All analogue components were printed on a Stratasys UPrintSE 3D printer (www.stratasys.com/3d-printers) using ABSplus-P430 (a production-grade thermoplastic ABS). The vertebral sections were imported to the printer software (CatalystEX) as a stereolithographic file (.stl) which was created by importing the CT volume file (.vol) into ScanIP (www.simpleware.com/software/scanip) and manipulating the file. Specifically, the background data were duplicated and resampled from 32-bit to 8-bit in an effort to reduce the file size. The threshold applied was based on the distinct histogram peaks and included small trabeculae while minimising soft tissue. All values were selected in order to maintain the morphology while reducing the number of elements and any errors in the resulting model.

After the .stl file was generated, an ABS sample known as an analogue vertebral body was printed. Following this an analogue motion segment (AMS) was created with the introduction of the silicone as the IVD simulant, for each real (biological) motion segment (RMS). An additional sample was produced from RMS 4, designated AMS 4ii. The origins of all segments, both biological and analogue, are summarised in Table 4-1.

Table 4-1 Origins of all biological and analogue segments. RMS = real (biological) motion segment. AMS = analogue motion segment. RVB = biological vertebral body. RVD = biological intervertebral disc. AVB = analogue vertebral body. AVD = analogue intervertebral disc.

Motion segment	Biological segment	ABS segment
RMS 1 (L5–L6)	RVB 1 RVB 2 RVD 1	AVB 1 AVB 2 AVD 1
RMS 2 (L4–L5)	RVB 3 RVB 4 RVD 2	AVB 3 AVB 4 AVD 2
RMS 3 (L3–L4)	RVB 5 RVB 6 RVD 3	AVB 5 AVB 6 AVD 3
RMS 4 (L1–L2)	RMS 4 / RMS 4_1	AMS 4 AMS 4ii

The setting used for the model interior was ‘solid’ and the support fill was set to ‘basic’. Most of the support material deposited during the printing process was removed manually, but a Support Removal Apparatus (SRA) bath was used as required to eliminate the final residues.

Earlier tests conducted on 3D-printed ABS cubes revealed their compressive strength. These data showed that the effect of layer orientation on the ultimate tensile load was less than 5.4% from the maxima to minima. Further, when comparing moduli in the elastic region, the difference was less than 16% between maximum and minimum values – however, when comparing similar orientations, the effect was negligible (Franceskides, et al., 2016). Consequently, because all the ABS samples in this study were printed and loaded in the same orientation, we assumed a negligible difference in stiffness due to the directionality of the ABS layers.

The IVD of each analogue motion segment was formed from PT Flex 70 liquid rubber, Shore A hardness 70. The design priority for the analogue IVD was to use a suitable rubber compound which, by adjusting its constitution, could be matched to the properties of biological IVD initially on the basis of its Shore A hardness value. Inevitably this kind of rubber analogue would only provide a uniform layer because the inner design and fibrous architecture of natural IVDs (with their collagen fibre woven layout) is too complex to replicate. PT Flex 70 2-part silicone was chosen for its curing time and a Shore A hardness value matching that of an IVD. An individualised cast was built around the superior and inferior endplates of the IVDs using Sugru (https://sugru.com). The correct height of the IVD (based on CT reconstructions) was ensured by placing struts (PT Flex 70) at three points on the endplates. PT Flex 70 was prepared and injected into the moulds (Figure 4-2).

Figure 4-2 Moulding of the IVD analogue using PTFlex 70.

A speckle pattern was applied to all samples for DIC analysis. White high-contrast paint was used as a base coat on the ABS samples and a black speckle pattern was then applied manually to all samples, with speckle size ranging from 0.35 to 4.35 mm in diameter (Figure 4-3).

The optimal speckle size was 3–5 pixels, (Palanca, et al., 2017) which was equivalent to 0.78–3.3 mm. All biological samples were removed from the freezer to thaw 6 h before testing as recommended (Smeathers & Joanes, 1988).

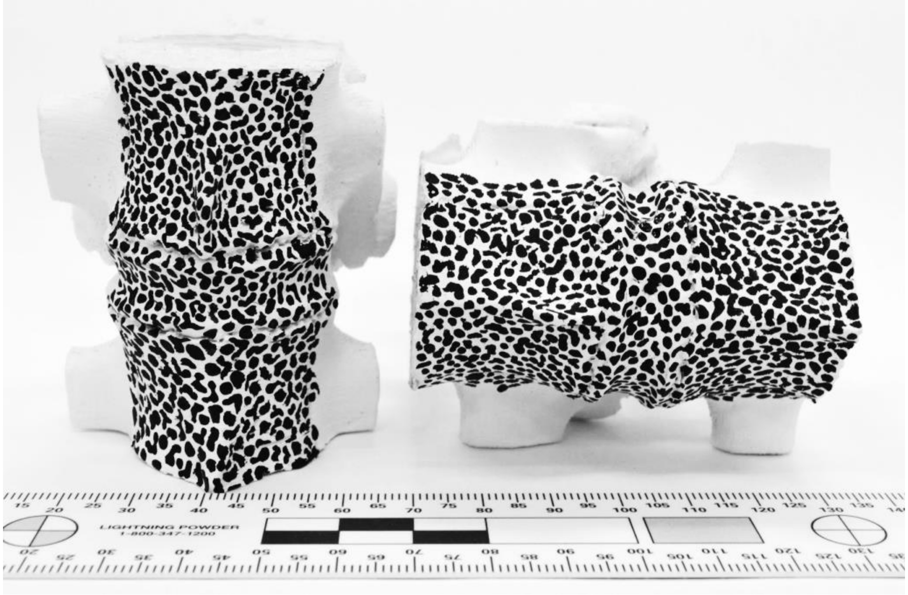

Figure 4-3 Speckle pattern applied to AMS 4 and AMS 4ii.

An Instron 5567 tensile testing machine (www.instron.co.uk) fitted with a 10-kN load cell was used to compress each sample at a quasi-static loading rate of 0.6 mm/min (strain rate range 6–10×10^{-4}/s). All samples were subjected to a 10–50 N preload before compression to reduce contact errors (Newell, et al., 2017). The top platen featured a spherical joint to further minimise contact errors and bending moments, and to ensure consistent loading across the sample. The experimental setup is shown in Figure 4-4.

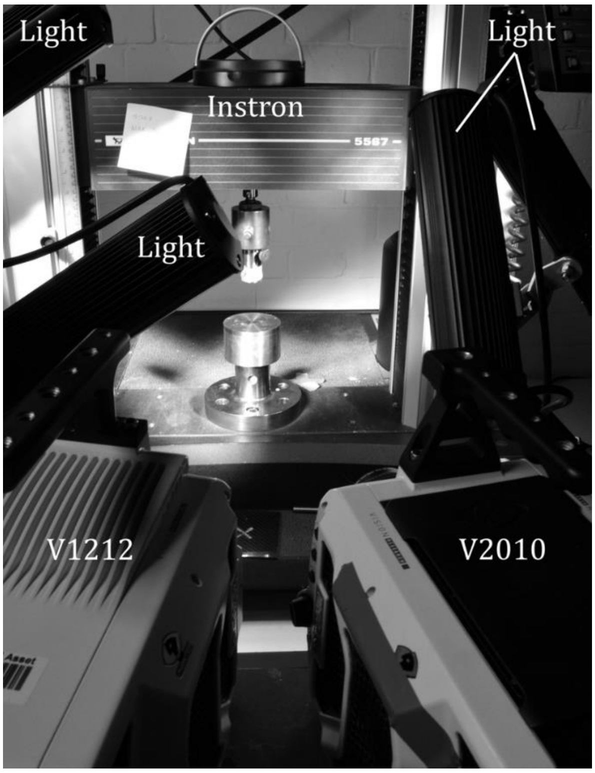

Figure 4-4 The experimental setup, with cameras V1212 (left) and V2010 (right), and with all light sources in position.

Two Phantom high-speed cameras (V1212 and V2010, with Nikon 50-mm f/1.4 lenses) recording at 1000 fps were used to obtain DIC data throughout loading. Cameras were positioned 25° apart and 450 mm from the sample. Calibration was performed with a simple 175 mm x 140 mm panel. PCC control software from the manufacturer was used to interface with the cameras. The DIC analysis facet size was 9 pixels, with a facet step of 3 pixels for all sections. The small facet step increased the measuring point density and accordingly also the computational time required, bringing the analysis time per specimen to more than 120 min. The strain calculation method was selected to match the non-uniform thickness of the specimens. Artificial lighting was provided by four LED light sources (Cree, www.cree.com/led-components), which produced negligible heat. All the natural light sources within the testing area were covered to produce consistent illumination for all tests. All DIC data collected by the high-speed cameras were analysed with GOM software (http://www.gom.com/metrology-systems/system-overview/aramis.html). Due to the large number of frames, high-speed image data were simplified by selecting one in every 10 images.

We performed 31 tests, 20 on ABS samples and 11 on biological samples. All samples were compressed at 0.6 mm/min. Each test was constrained to a total displacement calculated based on the height of the sample (Equation 4-1). The compression tests on all sections are summarised in Table 4-2.

Table 4-2 Compression data for all sections.

Sections	Nominal strain	Displacement (mm)
IVD	0.1	1.4 ± 0.1
VB	0.05	0.95 ± 0.42
AMS	See Equation 4-1	2.5
RMS	-	1.75

Equation 4-1

$$total\ displacement\ =\ height\ of\ vertebral\ bodies * 0.05\ +\ height\ of\ vertebral\ disc * 0.1$$

RMS4 was compressed to 1.75 mm due to load constraints, and greater compression was unnecessary because a sufficient portion of the elastic region was measured, and the yielding of samples was not required for this work.

4.4 Results and discussion

4.4.1 Isolated segments – vertebral bodies

Compression (load vs displacement) data for each analogue section were compared directly to the corresponding data for each biological section. Yielding and plastic deformation were observed in the biological vertebral body (RVB) samples but not the analogue vertebral body (AVB) samples at the tested constraints, as shown in Figure 4-5 and Figure 4-6.

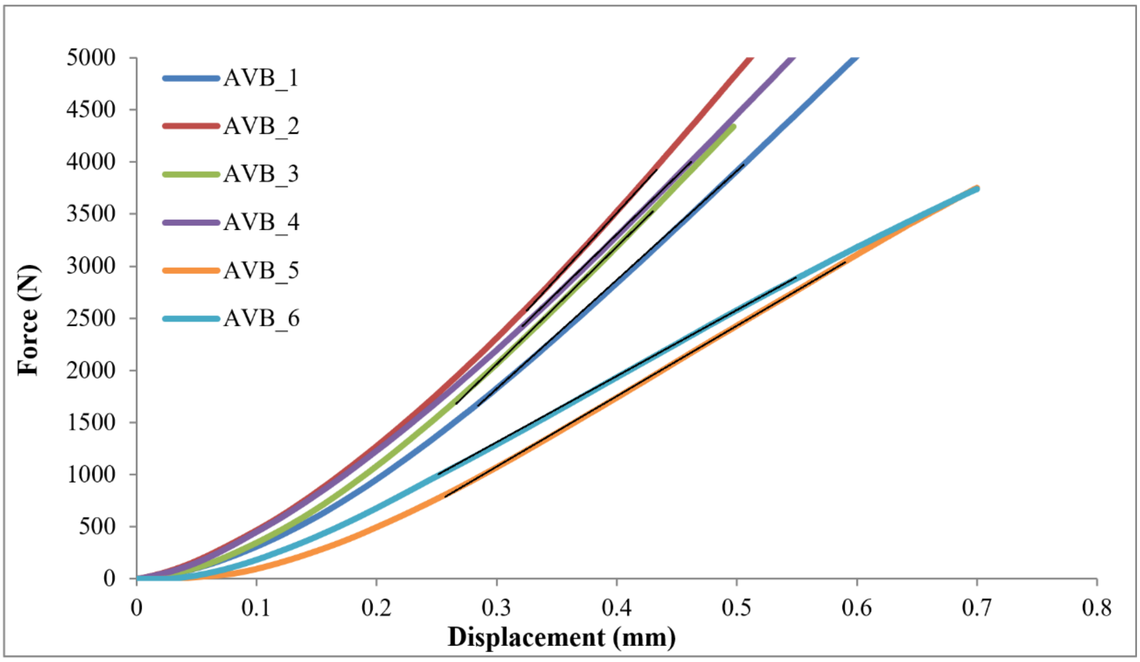

Figure 4-5 Compression (load vs displacement) data for AVB segments.

Stiffness was calculated from the linear elastic region of the curves for all samples. RVB samples had a mean stiffness of 8892 N/mm (N = 6, σ = 3375) and AVB samples had a mean stiffness of 9720 N/mm (N = 6, σ = 2,614).

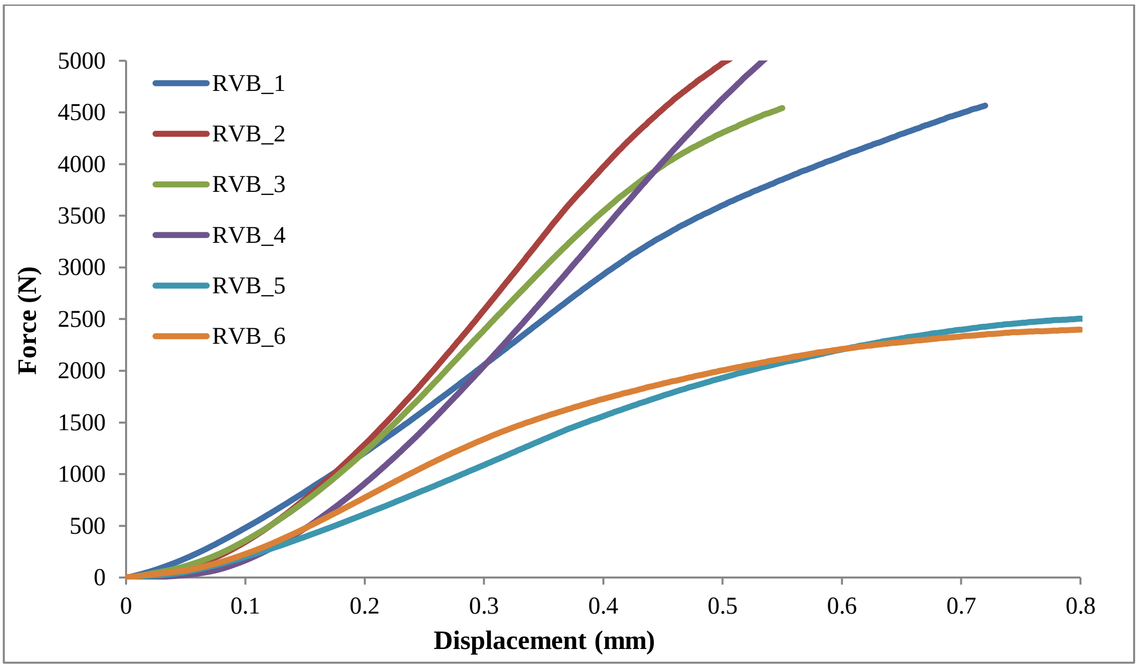

Figure 4-6 Compression (load vs displacement) data for RVB segments.

As shown in Figure 4-5 and Figure 4-6, two samples which were left in the warmer water (~80°C) bath for 16 h (RVBs 5 and 6) had a noticeably lower stiffness, probably due to the effect of the high temperature. There is a direct relationship between the loss of collagen and alterations to bone mineral structure caused by the boiling of bovine bone tissue, resulting in a three-fold increase in micrometre-scale porosity and an 18% reduction in bulk density (Roberts, et al., 2002). Such an effect would thus reduce the magnitude and breadth of the CT histogram.

Overall there was a very good one-to-one similarity between each real (biological) vertebral body (RVB) and its synthetic analogue. This is shown for RVB1 in Figure 4-7.

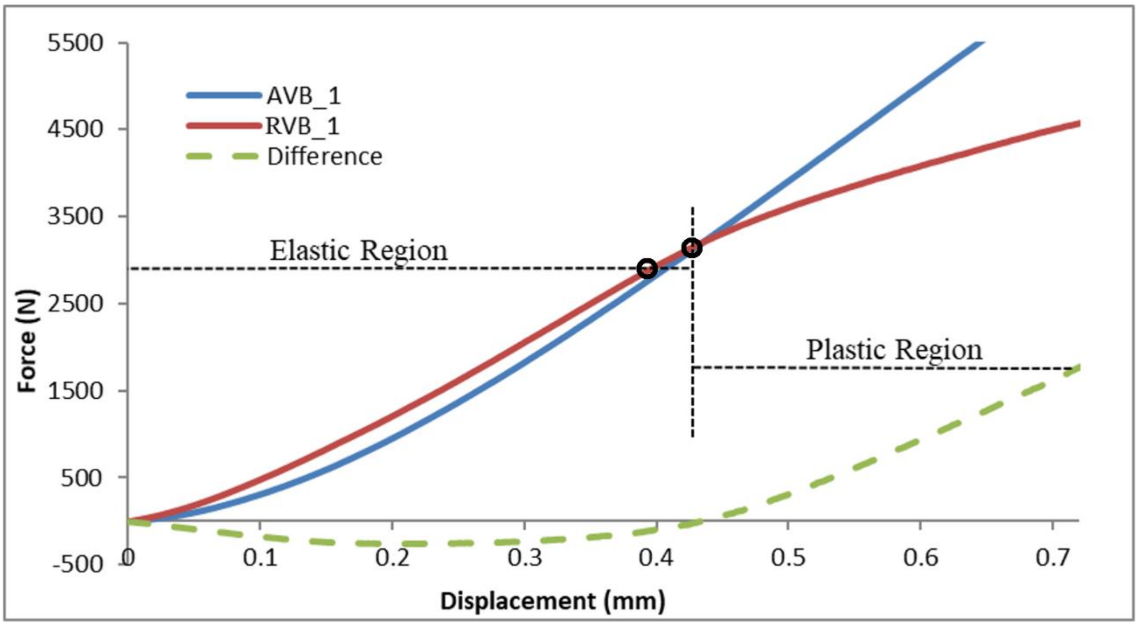

Figure 4-7 Load/deformation curves for RVB1 and AVB1 (the synthetic analogue). The difference in load between the two responses is shown separately as a dashed line illustrating the similarity of responses within the elastic region.

The two load/deformation curves followed each other until the start of the plastic region (for the biological samples) after which the load on the analogue specimen kept increasing while the biological specimen yielded and was crushed. The yield loads for the RVB were in the range 2000–4000 N or 3.8–10.3 MPa, in agreement with values reported in the literature [(Howarth, 2011); (Yingling, et al., 1997); (Gallagher, et al., 2010)].

4.4.2 Isolated segments – IVDs

Figure 4-8 shows the response of the biological IVDs (RVDs) and their rubber analogues (AVDs). The three RVDs behaved similarly and exhibited a J-shaped curve with an ever-increasing stiffness due to the presence of the collagen fibres in the annulus fibrosus.

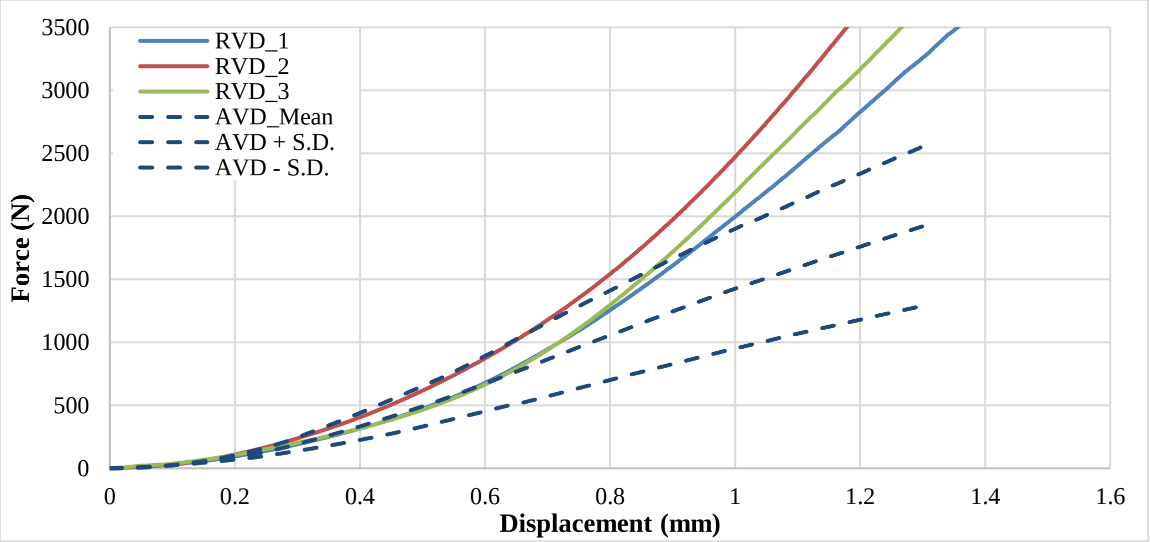

Figure 4-8 Compression (load vs displacement) data for RVD specimens (solid traces) and the envelope (mean ± SD) of PT Flex 70 analogue specimens.

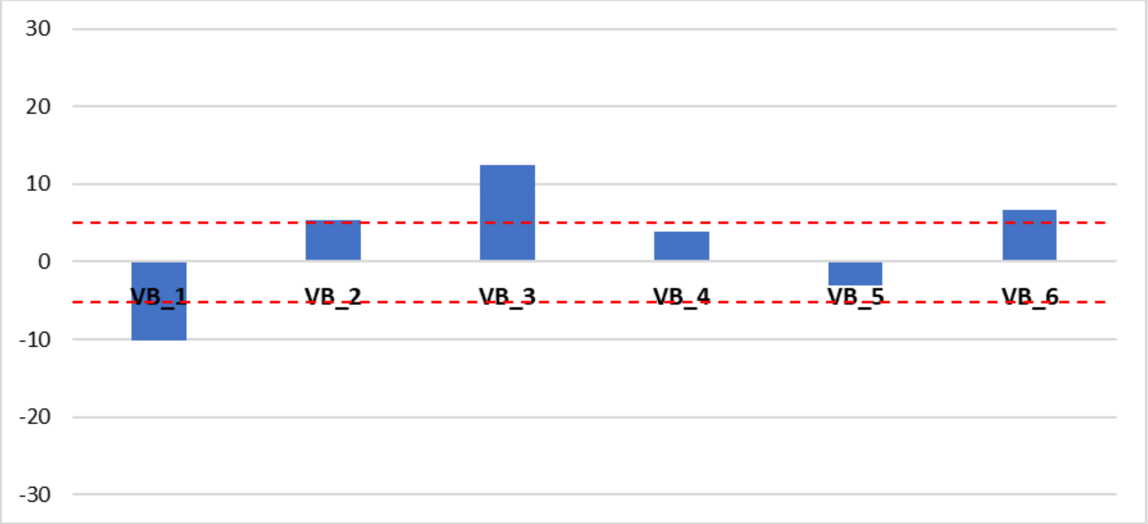

Figure 4-9 Percentage difference in stiffness values between each RVB and their synthetic analogues. The dashed lines represent ±5% differences in stiffness, shown for comparison.

The PT Flex 70 silicone analogue specimens were slightly softer (Figure 4-9 shows the envelope of the mean behaviour ± one SD of three curves) and exhibited the typical first stage of an elastomer load/deformation (F/d) curve.

These are S-shaped curves, which show a softening behaviour in the early region and then later on stiffen up considerably. S-shaped and J-shaped curves cannot be made to match each other throughout the whole range of F/d values, only within certain regions.

In our application, we chose to match the curves in the initial F/d region, starting with the selection of a compound of similar Shore A hardness, which seemed to work well for loads below 1000 N.

4.4.3 Motion segments

Figure 4-10 shows the load/displacement data for two biological motion segments and their synthetic analogues (two vertebral bodies and an artificial IVD between).

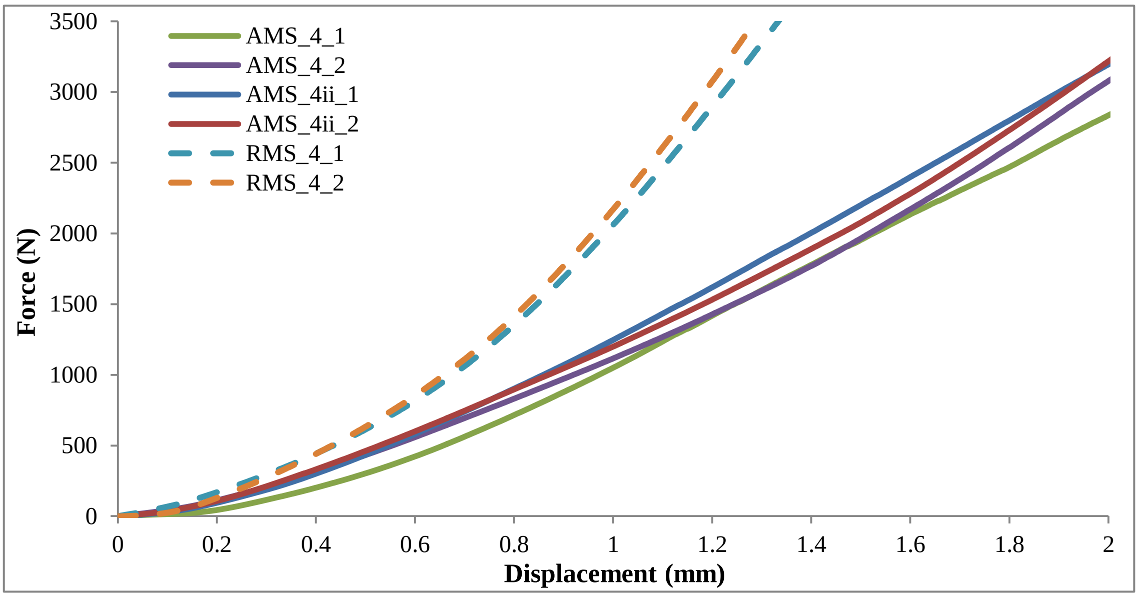

Figure 4-10 Compression (load/displacement) data for RMS4, AMS4 and AMS4ii.

The analogues were on the whole softer than the biological motion segments. The stiffness of RMS4 was 4,585 N/mm (N = 2, σ = 262), whereas the mean stiffness of AMS4_1 and AMS4ii_1 was 1868 N/mm (N = 4, σ = 82). The discrepancy between analogue motion segment models and their biological counterparts (from which the models were created) mainly reflects the imperfect matching of the IVD properties in models and biological specimens. This is because the much lower stiffness of IVDs compared to VBs means that much of the compression strain is concentrated in the IVD regions.

To demonstrate this effect, we used DIC to focus on the strains for VBs, IVDs and the total strain across the whole motion segment (Figure 4-11 and Figure 4-12).

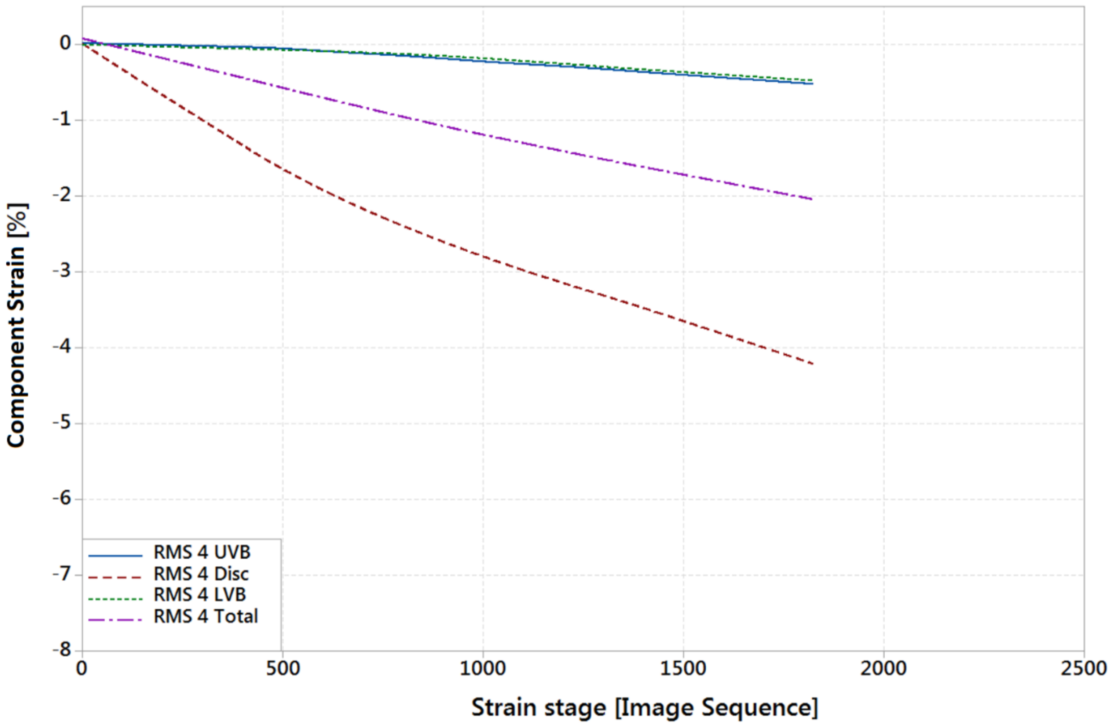

Figure 4-11 Smoothed line strain of four sections of RMS4: Upper Vertebral Body (UVB), IVD (measured endplate to endplate), Lower Vertebral Body (LVB), and Total (measured superior to inferior).

Calibration was performed with GOM before the test sequence. The static error was ± 4.2% as calculated using Equation 4-2 below.

Equation 4-2

$$\boldsymbol{Static\ Error} = \frac{(\boldsymbol{Displacement\ maximum} + \ |\boldsymbol{Displacement\ Minimum}|)}{\boldsymbol{Length}}$$

DIC analysis was performed on all biological and analogue samples with displacement measured between two points (a virtual extensometer). Lines were drawn vertically over each VB (upper and lower) and IVD section. Four sets of points were chosen on each motion segment: the top and bottom of each VB, the top and bottom of the IVD, and top and bottom of the entire motion segment.

The average major strain of each part was represented within each specific strain stage (capture image).

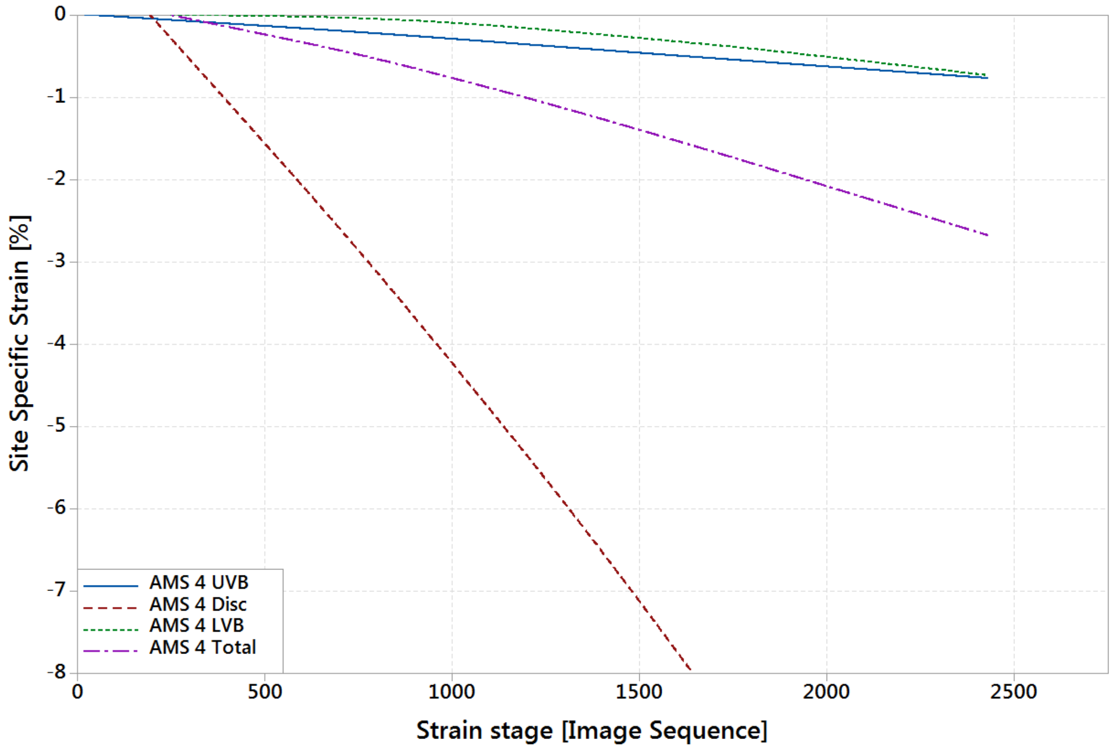

Figure 4-12 Smoothed line strain of four sections of AMS4: Upper Vertebral Body (UVB), IVD (measured endplate to endplate), Lower Vertebral Body (LVB), and Total (measured superior to inferior).

Figure 4-11 and Figure 4-12 show an example of the data obtained for RMS4 and AMS4, with the highest strain on the IVD and the lowest strain on the upper and lower VB. As expected, the total full-field strain is situated between these values.

4.4.4 Benefits and drawbacks of the model

Reliable and inexpensive patient-specific analogues are needed in the fields of forensic and injury biomechanics but it has been challenging to develop models which are both straightforward and accurate. We used micro-CT data to develop analogue models of VBs, IVDs and spinal motion segments and then tested them by compression, comparing like for like. The stiffness of the biological vertebral bodies (RVB) and the analogue vertebral bodies (AVB) were similar in magnitude. Each RVB behaved in a similar manner to the corresponding AVB section on an individual basis. However, the AVB samples tended to be less variable than the RVB samples, with standard deviations of 2,614.7 N/mm and 3,375.7 N/mm, respectively. This is consistent with previously tested spinal analogues [(Newell, et al., 2017); (Domann, 2011)]. The higher variability of the RVB specimen probably reflects the fact that live samples vary in both material properties and structural architectural design. The AVB samples were made from the same grade of industrial material (ABS), with only the structure matching the natural one.

The differences between the F/d behaviour of biological and analogue specimens were more pronounced once the biological specimens were taken beyond the yield point. At this stage, whereas the RVB samples yielded, the much stronger AVB samples continued in the elastic region. Shearing was observed in one sample (AVD1), which resulted in delamination of the disc from the endplate and thus a lower stiffness than AVD2 and AVD3. We can deduce that facet-less motion segments tend to be less stiff than the complete comparative segments, as previously reported (Holsgrove, et al., 2015).

Strains over the motion segment samples were taken in four different areas: UVB, LVB, IVD and Total. The strains over the IVD were measured from superior to inferior endplates because the surface layer of high-contrast medium bearing the fiducial marks was prone to delamination/deterioration during loading of the AVD. These four strains were plotted for motion segment testing and each section was plotted for all segments. All four strains correlated: LVB and UVB experienced the least amount of strain and the IVD experienced noticeably more strain, with the total strain between these values. Strains measured over the UVB followed a similar trend for both AMS and RMS, which was also true of the LVB measurements (Figures 4.11 and 4.12). Strains measured over the IVD were noticeably different, with the AMS samples experiencing significantly more strain than the RMS samples.

It is worth noting, however, that not all micro-CT scans were conducted at the same time and marginal differences in greyscale and more importantly the shading correction may therefore be present. These differences may cause minor changes in thresholding values during the manipulation and generation of the .stl files. To reduce the size of the .stl files, resampling of the data to 0.1 mm was necessary, as well as several other manipulations described in the methods section. These manipulations affect small morphologies in the samples. A higher-resolution printer might achieve a more detailed representation of the internal structure of the sample, which could lead to more accurate results. Furthermore, the moulding of the IVD analogue produced small bubbles within the polyurethane which also may affect the mechanical characteristics of the disc.

Another effect not considered here was the testing of the biological discs under hydrated conditions. Research using sheep vertebrae has revealed that the stiffness of ovine IVDs differs significantly when tested in a saline bath environment compared to air alone, with this being true in most loading modes such as torsion, flexion and bending: the IVDs were stiffer in air and more pliant in a saline environment (Costi, et al., 2002).

The quality of DIC analysis was limited by the lenses available because the minimum focus distance produced a large viewing field which was suboptimal for data collection. The high-contrast media applied to the ABS disc samples delaminated in some cases during compression and then folded. This delamination and folding affected how much coverage was received from DIC during the later stages of compression.

In the future, further work should be conducted on the stiffness of the motion segment by varying the polyurethane that makes up the IVD and the construction of the facet joints. Polyurethane with a higher Shore hardness value should produce a motion segment with greater stiffness. Facet joints could be made more realistic by adding a cartilage analogue. If the stiffness of AVD and AMS samples can be improved, the method could be applied to human spinal motion segments with a higher degree of agreement.

4.5 Conclusions

The method described in this report produced VB analogues similar in stiffness to biological VBs with less apparent variability. The polyurethane chosen for the IVD analogue was significantly less stiff than biological IVDs because it was originally chosen to match only the Shore A hardness values. Further work is needed to find a more suitable IVD analogue, allowing the production and validation of more accurate spinal motion segment analogues. Analysis of DIC data revealed that although the RMS and AMS samples deformed in the same manner, the IVDs deformed more than the VBs, although the biological IVDs deformed significantly less than the analogue IVDs. Overall, this new method produces a simple analogue of spinal VB segments within the elastic regions for quasi-static axial compressive loading, which will improve our ability to build accurate patient-specific models for biomechanical testing.

4.6 Acknowledgments

This work was supported by an internal grant from Cranfield University (CF), a project grant from the Royal Centre for Defence Medicine (RCDM) Birmingham (PZ), and by in-kind support from Vision Research. The authors have no conflicts of interest to declare. We acknowledge the work, skill and expertise offered by Karl Norris in the mechanical workshop of Cranfield University, and Jolyon Cleaves of Vision Research for providing the high-speed cameras. Ethical approval was granted by the Cranfield University Research and Ethics Committee (CURES) under approval reference CURES/1014/2016. This paper is dedicated to one of the authors, Dr Mike Gibson, whose untimely death is a great loss to us all.

4.7 References

ASTM, 2015. *Standard Test Methods for Spinal Implant Constructs in a Vertebrectomy Model,* West Conshohocken (PA, USA): ASTM International.

Busscher, I. et al., 2010. In Vitro Biomechanical Characteristics of the Spine: A Comparison Between Human and Porcine Spinal Segments. *Spine,* 35(2), pp. 35-42.

Costi, J., Hearn, T. & Fazzalari, N., 2002. The effect of hydration on the stiffness of intervertebral discs in an ovine model. *Clinical Biomechanics*, 17(6), pp. 446-455.

Dath, R., Ebinesan, A. D., Porter, K. M. & Miles, A. W., 2007. Anatomical measurements of porcine lumbar vertebrae. *Clinical Biomechanics,* Volume 22, pp. 607-613.

Domann, J. P., 2011. *Development and Validation of an Analogue Lumbar Spine Model and its Integral Components,* Kansas: University of Kansas.

Franceskides, C. et al., 2016. *Evaluation of bone excision on occipital area of simulated human skull.* Lyon, European Society of Biomechanics.

Gallagher, K. M., Howarth, S. J. & Callaghan, J. P., 2010. Effects of anterior shear displacement rate on the structural properties of the porcine cervical spine. *Journal of Biomechanical Engineering,* Volume 132, pp. 1149-1154.

Holsgrove, T. P., Harinderjit, S. G., Miles, A. W. & Ghenduzzi, S., 2015. The dynamic, six-axis stiffness matrix testing of porcine spinal specimens. *The Spine Journal,* 15(1), pp. 176-184.

Howarth, S. J., 2011. *Mechanical response of the porcine cervical spine to acute and repetitive anterior-posterior shear,* Waterloo, Ontario: University of Waterloo.

Lott, B. D., Reece, F. N. & Drott, J. H., 1980. Effect of Preconditioning on Bone Breaking Strength. *Poultry Science* , Volume 59, pp. 724-725.

Newell, N. et al., 2017. Biomechanics of the human intervertebral disc: A review of testing techniques and results. *Journal of the Mechanical Behavior of Biomedical Materials,* Volume 69, pp. 420-434.

Palanca, M., Marco, M., Ruspi, M. L. & Cristofolini, L., 2017. Full-field strain distribution in multi-vertebra spine segments: An in vitro application of digital image correlation. *Medical Engineering & Physics,* Volume 000, pp. 1-8.

Palanca, M., Tozzi, G. & Cristofolini, L., 2016. The use of digital image correlation in the biomechanical area: a review. *International Biomechanics,* 3(1), pp. 1-21.

Roberts, S. J., Smith, C. I., Millard, A. & Collins, M. J., 2002. The taphonomy of cooked bone: Characterising boiling and its physico-chemical effects. *Archaeometry,* 44(3), pp. 485-494.

Sawbones, 2012. *Biomechanical Spine Product Research.* [Online] Available at: http://www.sawbones.com/UserFiles/Documents/Product/BioSpine_info.pdf[Accessed February 2018].

Shore, A. . F. & Shore, C. P., 1930. *Apparatus for measuring the hardness of materials.* US, Patent No. US1770045 (A) — 1930-07-08.

Smeathers, J. E. & Joanes, D. N., 1988. Dynamic compressive properties of human lumbar intervertebral joints: a comparison between fresh and thawed specimens. *J Biomech,* 21(5), pp. 425-433.

Smit, T. H., 2002. The use of a quadruped as an in vivo model for the study of the spine – biomechanical considerations. *European Spine Journal,* Volume 11, pp. 137-144.

Wang, T., Ball, J. R., Pelletier, M. H. & Walsh, W. R., 2014. *Initial Experience with Synthetic Spinal Motion Segments: Biomechanical Assessment of High Cycle and Implant Performance.* New Orleans (LA, USA), ORS Annual Meeting.

Wilke, H. J., Krischack, S. & Claes, L. E., 1996. Formalin Fixation Strongly Influences Biomechanical Properties of the Spine. *Journal of Biomechanics,* 29(12), pp. 1629-1631.

Yingling, V. R., Callaghan, J. P. & McGill, S. M., 1997. ynamic loading affects the mechanical properties and failure site of porcine spines. *Clinical Biomechanics,* Volume 12, pp. 301-305.

Zioupos, P., Smith, C. & Yuehuei, A., 1999. Factors Affecting Mechanical Properties of Bone. In: A. Yuehuei & D. A. Robert , eds. *Mechanical Testing of Bone and the Bone-Implant Interface.* s.l.:CRC Press, pp. 65-85.

CHAPTER 5 PREFACE

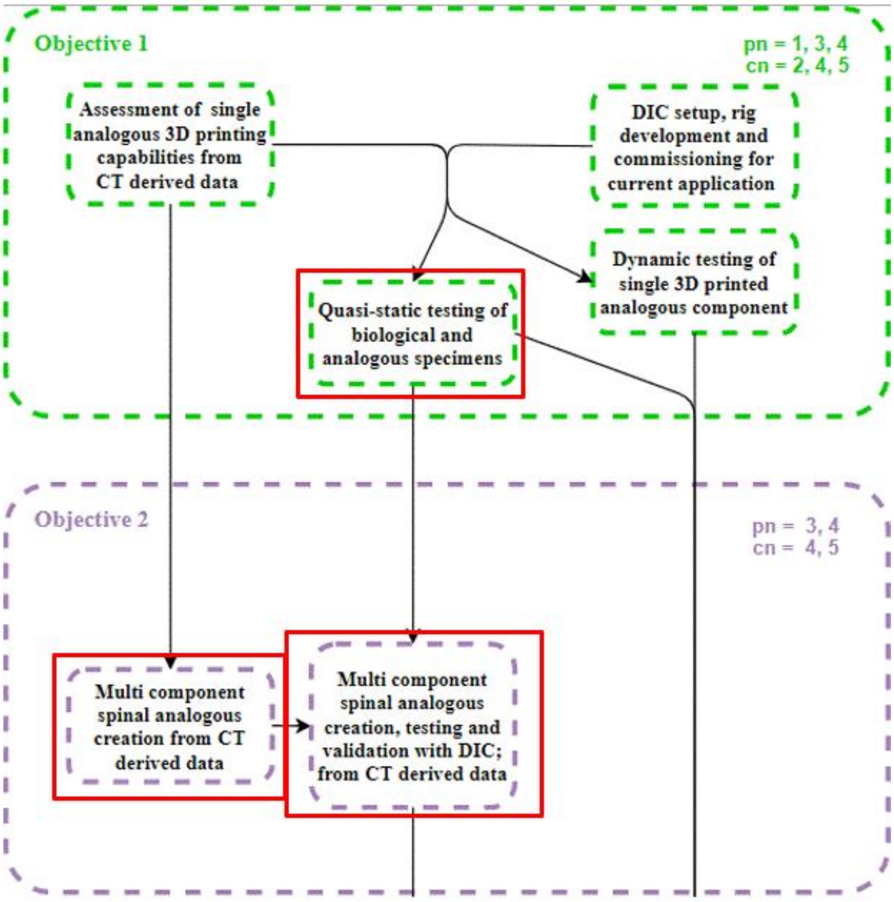

Chapter 4[5] (Paper 3) described the development of 3D-printed components at both the sub-assembly and assembly levels. The biofidelity and mechanical responses of the components were assessed. Critical factors and limitations in the manufacturing process were identified, which in turn affected the performance of the analogues.

Accordingly, Chapter 5[6] (Paper 4) fine-tunes the manufacturing process and assesses in more detail the critical factors presented in Chapter 4 while quantifying the performance limitations of the system in all three phases: manufacturing, testing and analysis.

---

[5] Work presented in SAFE EUR 2017 and SAFE US 2017 Conferences

[6] Work presented in SAFE US 2017 and ESB 2017 Conferences

5 SPINAL MOTION SEGMENTS: TUNING AND OPTIMISATION OF BIOFIDELIC PERFORMANCE

Constantinos Franceskides[1*], Emily Arnold[1], Ian Horsfall[2], Gianluca Tozzi[3], Michael Gibson[4], Peter Zioupos[1]

[1]*Musculoskeletal and Medicolegal research Group, Cranfield Forensic Institute, Centre for Defence Engineering, Cranfield University, Defence Academy of the UK, Shrivenham, SN6 8LA, UK*

[2]*Impact and Armour Group, Centre for Defence Engineering, Cranfield University, Defence Academy of the UK, Shrivenham, SN6 8LA, UK*

[3]*School of Engineering, University of Portsmouth, Anglesea Road, Portsmouth, PO1 3DJ, UK*

[4]*Centre for Simulation & Analytics, Centre for Defence Engineering, Cranfield University, Defence Academy of the UK; Shrivenham, SN6 8LA, UK*

5.1 Abstract

Most commercially available spine analogues are not intended for biomechanical testing, and the few that are suitable for this purpose are very expensive, creating a demand for better patient-specific analogues that are more widely accessible. Such analogues would also avoid the ethical restrictions surrounding the use of biological specimens and complications arising from their inherent variability. Here we sought to improve the accuracy of patient-specific motion segment analogues by creating acrylonitrile butadiene styrene replicas of porcine spine segments (T12–L5) scanned by computed tomography. We then tested them by axial loading at 0.6 mm/min (strain rate range 6–10×10^{-4}/s). We used different intervertebral disc and facet joint simulants and measured the effect of the facet joints on the compressive response. Different scanning resolutions and data acquisition techniques were also compared in order to determine their effect on analogue performance. We found that the selection of an appropriate intervertebral disc simulant (PT Flex 85) achieved a realistic force/displacement response and highlighted the key role of facet joints in the biofidelic behaviour of the entire motion segment. We have therefore confirmed the feasibility of a rapid and inexpensive 3D-printing method for the production of high-quality patient-specific spine analogues suitable for biomechanical testing.

Keywords: Spine; Bone analogue; Micro-CT; 3D Printing

5.2 Introduction

The availability of imaging methods to analyse and comprehend the musculoskeletal system has increased the demand for more accurate analogues that are suitable for biomechanical testing. Analogues also circumvent the challenges associated with tests on cadaveric materials, including storing, handling and disposal issues as well as ethical restrictions (Wilke, et al., 1996).

Mechanically and anatomically correct models are provided by companies such as ASM, Sawbones and Synbone, but they are expensive, and, like all commercial analogue models, they are not patient-specific [(Domann, et al., 2011), (Friss, et al., 2003)]. Such analogues have in the past provided support for implant testing as an alternative to human or animal cadavers (Wang, et al., 2014). They also emulate human cadaveric spines in both morphological and biomechanical terms, such as the range of motion (focusing on bending, twisting, flexing and extending). However, they do not address uniaxial compressive effects [(Camisa, et al., 2014); (Wang, et al., 2014); (Campbell, et al., 2010); (Domann, et al., 2011)].

We have previously reported the development of biofidelic models of an analogue porcine motion segment (Franceskides, et al., 2018). However, as data acquisition by digital image correlation (DIC) has become more refined, the role of the facet joints and intervertebral discs (IVDs) has been highlighted (Pal & Routal, 1987), (Jaumard, et al., 2011). It is important to determine the best practices for the incorporation of such elements into analogue models in order to emulate cadaveric samples more accurately. It is also necessary to consider the resolution of scanning and how this affects the analogue’s performance.

Here we have developed a novel and accessible protocol based on our earlier methods [(Palanca, et al., 2017); (Franceskides, et al., 2016)] involving the inexpensive production of 3D-printed analogues augmented with realistic facet joints and IVDs. Such analogues can be applied in future research projects to develop more complex and accurate models of the musculoskeletal system.

5.3 Materials and methods

5.3.1 Analogue creation

The templates for the motion segment analogues were porcine spinal material (from animals 8–12 months old, destined for the food supply chain) obtained from a local butcher. The cadaveric material was de-fleshed with scalpels in a 40°C water bath for 90 min [(Lott, et al., 1980) and (Roberts, et al., 2002)]. The cleaned samples were scanned using a Nikon CT H225 cone beam μCT scanner (X-Tek Systems Ltd, Tring, Hertfordshire, UK) operated at 70 kV and 90 μA.

After scanning the cadaveric spinal portions (defined here as real motion segments and represented by the abbreviation RMS), noise reduction and beam hardening corrections were applied to the data using CT Pro 3D (Nikon Metrology UK Ltd, Hertfordshire, UK). Further reconstruction and editing was carried out using Simpleware ScanIP M-2017.06-SP2 (Synopsys Inc., Mountain View, CA, USA). This process also yielded over-threshold and under-threshold samples which were derived by altering the volume fraction (VF) of the normal analogue by ±40%. The data were then used to create artificial motion segments (represented by the abbreviation AMS) containing artificial vertebral bodies (AVBs).

Four real motion segments were tested, named RMS4–7 (Table 5-1).

Table 5-1 Allocation of analogues from cadaveric materials.

Motion segment	(L1–L2)	(T12–L1)	(L2–L3)	(L4–L5)
Real motion segment	RMS 4	RMS 5	RMS 6	RMS 7
ABS-based artificial motion segment	AVB8_O AVB8_U AMS8_70 AMS8_85	AVB5_N AVB5_L AMS5_F AMS5_NF	AVB6_N AVB6_L AMS6_F AMS6_NF	AVB7_N AVB7_L AMS7_F AMS7_NF

The variance in scanning resolution for RMS5–7 was tested by producing two distinct voxel dimensions of 0.063 and 0.123 mm (RMS#_N for the normal scans and RMS#_L for the low magnification/resolution scans), thus replicating the artificial vertebral bodies (AVB5–7). In contrast, RMS4 was used as a model to select disc simulants (AMS8_70 and AMS8_85). In addition, facet stiffness was tested (AMS#_F denoting a facet present and AMS#_NF denoting facet absence) simply by removing the facet processes from the tested models. Finally, the overcompensation and undercompensation of thresholding was tested using RMS4 samples AVB#_O for overcompensation and AVB#_U for undercompensation. This was carried out using the Grey Scale (GS) selection tools in ScanIP and adjusting as required to achieve the appropriate VF variance. Finally, operations such as flood-fill as well as a smoothing filter (Recursive Gaussian at 0.2 pixels) were applied to finish off the post-printed models.

The CT (DICOM) data were imported as a 32-bit float, converted to an 8-bit float and then resampled to 0.400 mm in an effort to reduce the file size, to match the printer nozzle size, and also to be in line with earlier work on this topic (Franceskides, et al., 2018). The analogues were then printed using a fused deposition modelling (FDM) UPrintSE 3D printer (Stratasys Inc., Eden Prairie, MN, USA). The .cmb toolpath files were created using Stratasys CatalystEX v4.5 (Stratasys, Inc.). Support fill was set to ‘smart’ and model interior to ‘solid’, meaning that the average printing time per sample was ~40 min for the larger AVB samples.

Finally, the IVD was formed using PT Flex 85 (Shore A hardness 85) and the intra-facet cartilage was formed using PT Flex 70 (Shore A hardness 70) liquid rubber (Polytek Development Corp., Easton, PA, USA). Once mixed, the rubber was injected into a cast created around the superior and inferior endplates and the superior and inferior articular processes of the IVDs using Sugru mouldable glue (FormFormForm Ltd, London, UK). The IVD thickness was based on the CT reconstruction data and was achieved by placing struts of the appropriate height (produced using the matching PT Flex compound) at three points separating the endplates.

5.3.2 Sensitivity and refinement of data acquisition techniques

5.3.2.1 Strain validation

The DIC method was tested against a 25 x 9 mm polyvinyl chloride (PVC) core with a speckled pattern applied using high-contrast paint (Figure 5-1).

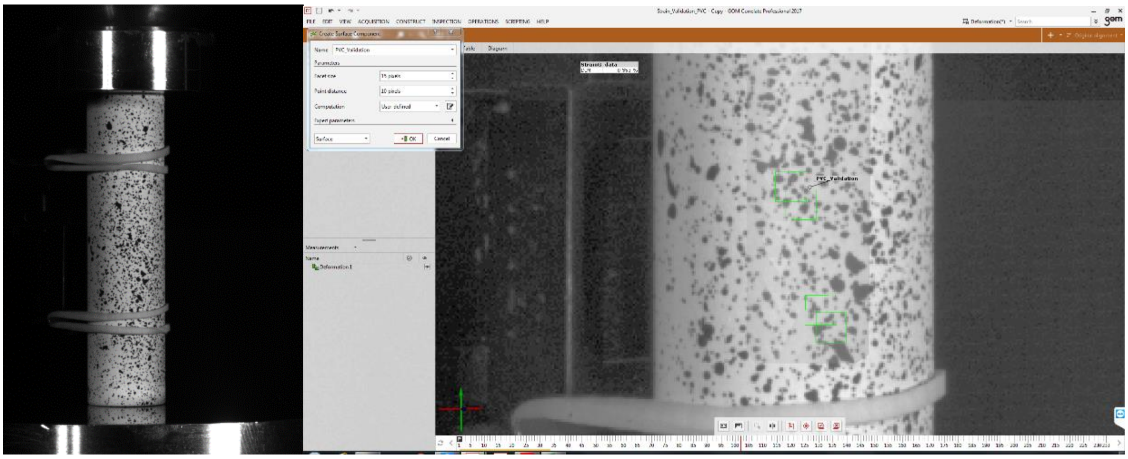

Figure 5-1 PVC core setup. (Left) PVC core with strain gauge attached and speckle pattern applied. (Right) Detailed GOM configuration.

A sequence of images was captured at 1000 fps using Phantom V1212 and V2512 cameras. PVC was used instead of ABS due to its availability, given that the Young's modulus and tensile strength of both materials are similar (Matmatch GmbH, 2018). The DIC data were analysed using GOM Correlate Professional (2017 Hotfix 5, GOM GmbH, Braunschweig, Germany). The strain gauge was applied on the rear of the core, in order to allow DIC acquisition in the front.

5.3.2.2 Computational-facet and point distance sensitivity study

To measure the effect of the computational-facet size and point distance, the results from the strain gauge were considered as the benchmark and thus compared to the results obtained from GOM. To do this, the results from the default point distance (16 pixels) and computational-facet size (19x19 pixels) were used to compare the default point distance to computational-facet size ratio (16/19) to other ratios (4/3, 3/3, 1/2 and 1/3). The results were then compared to the strain gauge results and their variances were plotted. In a similar manner, the different computational-facet sizes (6, 12, 19, 24 and 30) were tested with varying point distances and the results were then compared to the strain gauge data to obtain the corresponding variances. The different point distance to computational-facet size ratios (lowest common multiplier, LCM) are shown in Table 5-2.

Table 5-2 LCM point distances compared to the computational-facet sizes tested.

Point distance to computational-facet size ratio					
608/456	456/456	384/456	228/456	152/456	
6	6	6	6	6	**computational-facet size**
12	12	12	12	12	
19	19	19	19	19	
Not Comp	24	24	24	24	
Not Comp	30	30	30	30	

5.3.2.3 Dead-weight experiments

The motion segment was incrementally loaded to determine whether residual effects under constant loading were identified by DIC analysis. This was achieved by looking at the displacement in the *x* and *y* axes along the entire length of the sample. Loads were applied in increments of 100 N up to 2000 N, with a series of 10 images captured once the sample held the constant load for 1 h. The testing method and apparatus are shown schematically in Figure 5-2.

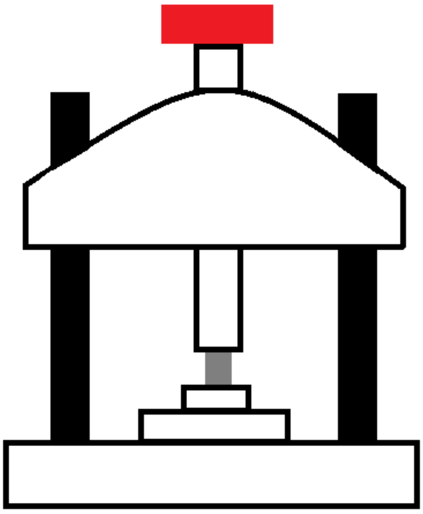

Figure 5-2 The dead-weight testing apparatus, with the red block denoting weight, black rods denoting the traverse guides, and the grey block denoting the sample.

The sample was loaded directly under the push rod and then weight was added on top to achieve the necessary load increments.

5.3.2.4 Effects of the support cleaning apparatus

A combination of Support Cleaning Apparatus (SCA) (PADT Inc., Tempe, USA) and WaterWorks P400SC (Stratasys Inc., Eden Prairie, MN, USA) is the preferred method for cleaning/removing the support material from 3D-printed components. As per the Stratasys SCA manual (GOM mbH, 2018) the construct supports were removed by immersion in NaOH at 70C° for 4 h (Phoenix Analysis & Design Technologies, 2010). For intricate and complex geometries, and where mechanical responses are important, the removal of the support is essential. Figure 5-3 illustrates a mask created (shown in green) to highlight the support within the vertebral body. To test the effect of cleaning, two analogues were printed.

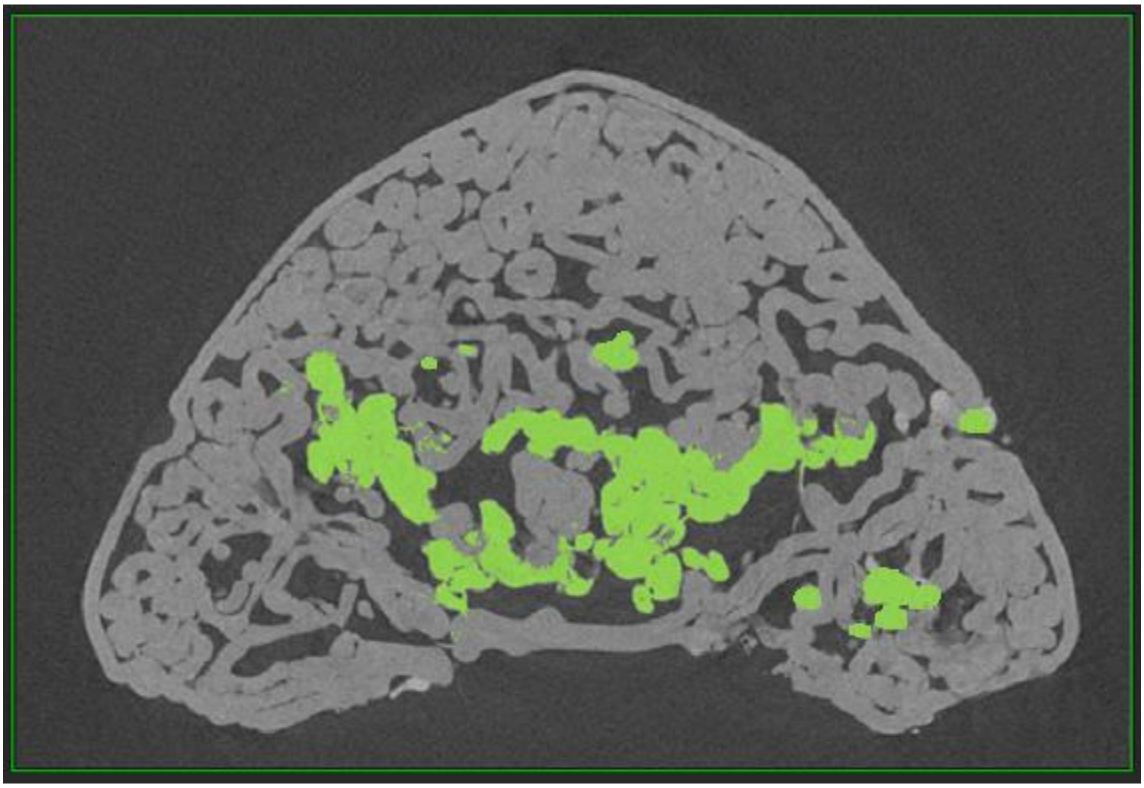

Figure 5-3 Artificial vertebral body (printed and rescanned sample) with support material highlighted in green, and ABS shown in grey.

One was subjected to the cleaning treatment and the other was used as an untreated control for subsequent testing to failure.

5.3.3 Testing the analogue specimens

All compressive testing was conducted using an Instron 5567 tensile testing machine (Instron, High Wycombe, UK) fitted with a 10-kN load cell, and each sample was compressed at a quasi-static loading rate of 0.6 mm/min (strain rate range 6–10×10^{-4}/s). A relatively small preload of 10–50 N was applied to all samples before initiating the test to reduce any inherent contact errors (Newell, et al., 2017). A 75-mm diameter spherical joint platen was used to minimise both contact errors and bending moments, and also to ensure consistent loading across the sample surface area. Finally, DIC analysis was conducted by capturing images at 1,000 fps using a pair of Phantom high-speed cameras controlled by Phantom Camera Control (PCC) v2.8.761 software (both from Vision Research Inc., Wayne, USA).

5.4 Results and discussion

5.4.1 DIC sensitivity, strain validation and dead-weight error

The tests conducted on varying computational-facet sizes, point distances and their associated ratios are shown in Figure 5-5 and Figure 5-6. The largest ratio of 4/3 (or as per LCM, 608/456) was unable to yield strains in two cases, when the computational-facet sizes were 24 and 30, probably because the intersection deviation was outside computational limits. In addition, the worst ratio when comparing average errors was 1/3 (or as per LCM, 152/456), partly due to the error of 4.32% obtained on the six-pixel computational-facet. All average errors were closely grouped: 1.39%, 1.70%, 1.34%, 1.61% and 1.73%, respectively. Figure 5-4 highlights the error observed when keeping the computational-facet size fixed and varying the point distance (thus altering the point distance to computational-facet size ratio).

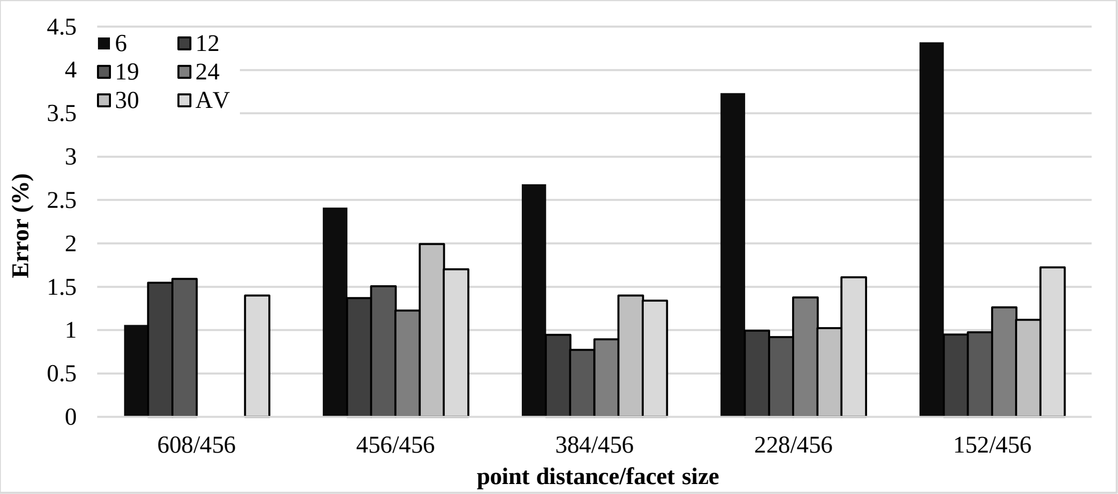

Figure 5-4 Error variance between the strain gauge data and each point distance to computational-facet size ratio, with varying facet size.

Clearly, the six-pixel computational-facet size resulted in the lowest resolution, probably because the speckle pattern becomes less resolvable with smaller computational-facet sizes, resulting in total colour patching (only white or black within a visible single computational-facet). Hence the recommended speckle size should not be greater than 3–5 pixels (Palanca, et al., 2016).

Average errors varied from 2.84% down to 1.15% when compared to the strain gauge readings. Computational-facet size provided a consistent low error with the best reading obtained at the 16/19 ratio (or as per LCM, 384/456), which is the ratio recommended by GOM (GOM mbH, 2018). Results obtained with the ratios 4/3 (as per LCM, 608/456) and 3/3 (as per LCM, 456/456) were less reliable because they provided no data overlap and therefore no intersection, making the computational-facet-to-facet interpolation at every stage even less accurate. Even so, the ratio selected for our remaining experiments was the one recommended in the literature, as was the computational-facet size (Figure 5-5). This achieved the lowest average error and also the lowest individual error of 0.77%.

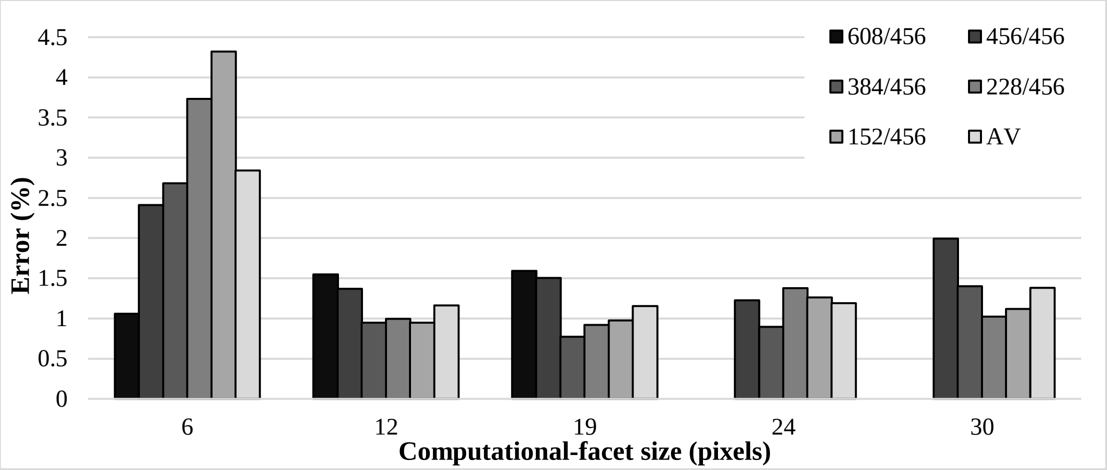

Figure 5-5 Error variance between the strain gauge data and each computational-facet size, with varying point distance to computational-facet size ratios.

Figure 5-6 shows the plot obtained from the PVC compression tests.

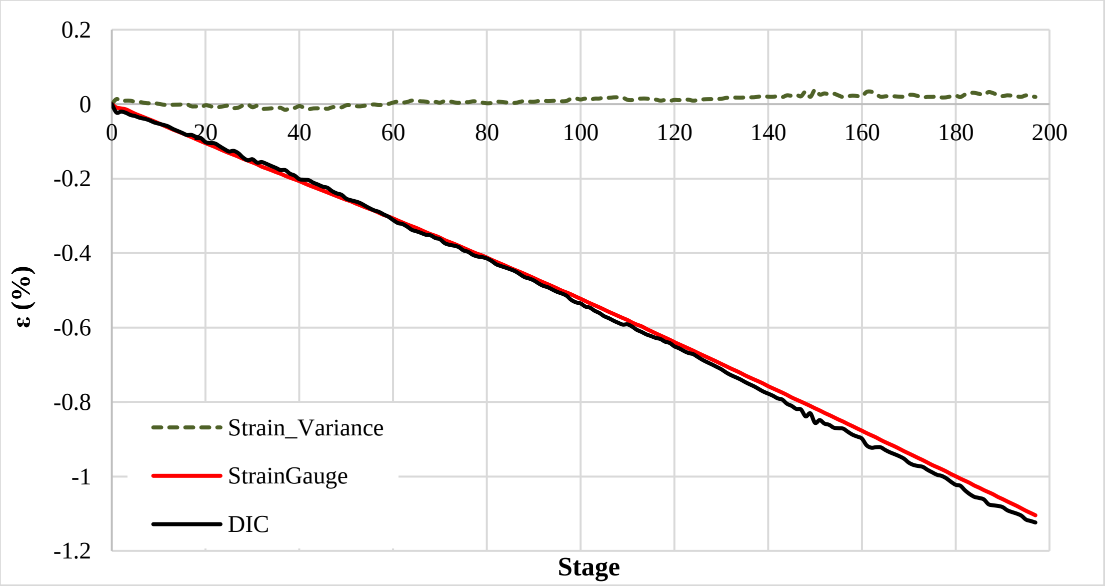

Figure 5-6 Strain measurements obtained by DIC analysis compared to strain gauge data, with errors shown as a dashed line.

The plot shows a clear agreement between the DIC and strain gauge data. Figure 5-7 shows the error obtained from the variance of the DIC and strain gauge data, with the average error line at 9.2 με (%). The total error is represented by the dashed green line in Figure 5-6, with the average error shown in red. Although the error was based on a 0.3-mm compression, the agreement between the two techniques was within anticipated limits (Amiot, et al., 2013).

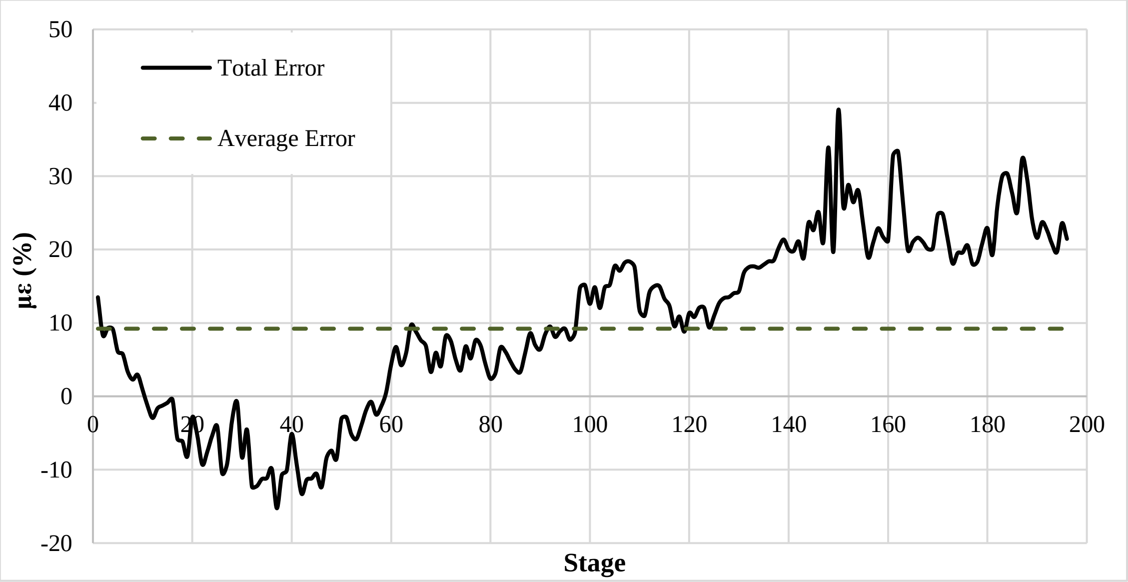

Figure 5-7 Total error in με throughout the 200-stage comparison obtained by DIC analysis compared to strain gauge data.

Finally, the noise in the system was recorded as previously described (Franceskides, et al., 2016).

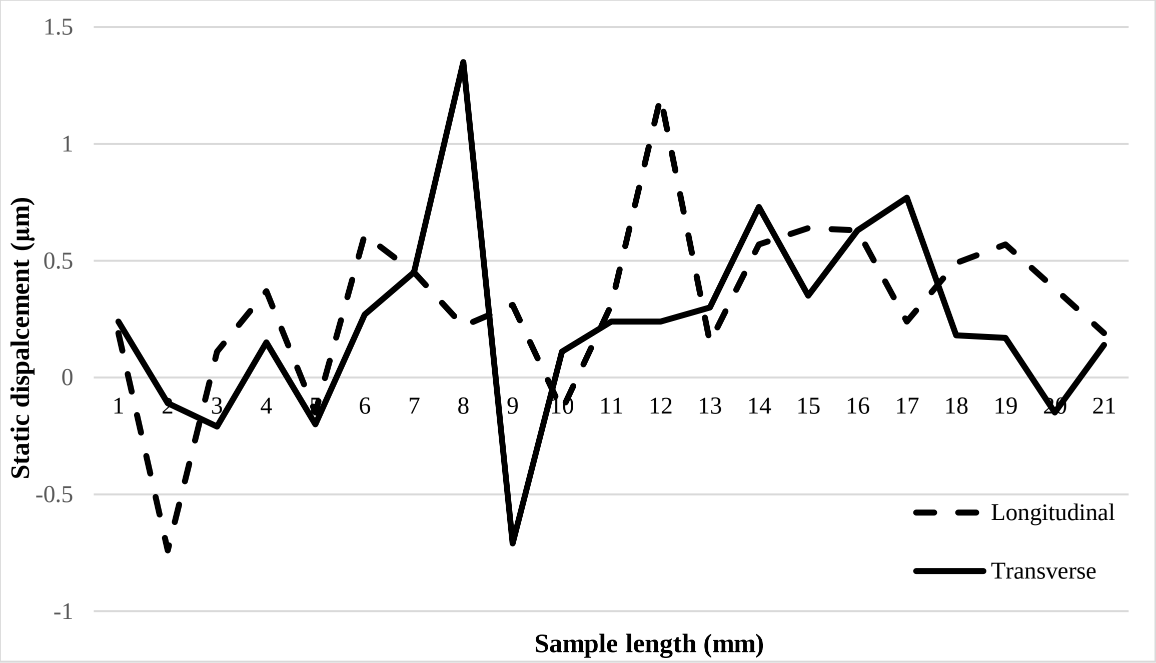

Figure 5-8 Static error over a viewing aperture of 21 x 21 mm on the *x* and *y* axes.

This was obtained in the static state without loading (Figure 5-8) and in the static state with dead-weight loading (Figure 5-9).

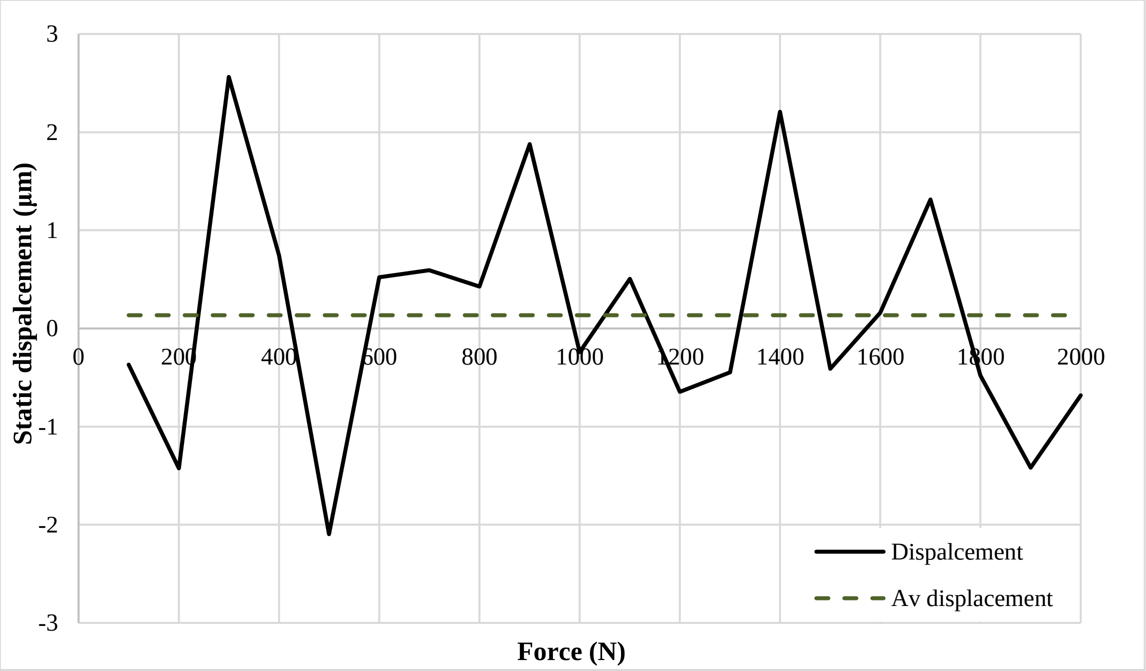

Figure 5-9 The *y*-axis displacement error under uniaxial dead-weight loading.

The in-plane strains (pseudo-strains) were therefore ignored because no external factor was acting against the component so no in-line movements were anticipated. The error obtained from a 21 x 21 mm aperture on the *x* and *y* axes is shown in Figure 5-8. Along the *x* axis, the error ranges from –0.71 to 1.35 µm and along the *y* axis it ranges from –7.4 to 1.2 µm, which is less than 2 µm over the 21-mm test length and can therefore be disregarded. The dead-weight error was calculated only for the direction of loading (*y*) but also with a 20-mm aperture. The error was acquired by averaging the displacement observed along this axis over the sequence of a 10-image burst at 1000 fps. The loading was introduced in increments of 100 N at 60-min intervals up to and including 2000 N. As shown in Figure 5-9, the displacement varied from –2.1 to 2.7 µm, which is twice the displacement under no load. This was not expected, yet there seems to be a periodic tendency which may indicate that external factors contribute to the effect. One uncontrolled variable was the heating of the test area, which had an unknown periodicity. This should not be ignored because the radiant heat from the elements could have affected the component temperature and thus the loading response of the polymer. Regardless of the factors that may have contributed to the variance observed, the resulting peak-to-peak error was within the range observed in previous studies, i.e. less than 20 µm (Siebert, et al., 2007). These results provide confidence in the DIC method, which could be fine-tuned to increase its accuracy. The most important factors include, but are not limited to, the speckle pattern, the computational-facet size and the point distance, which ensure a fine balance between computational speed and accurate image analysis.

5.4.2 Effects of the support removal process

Due to the intricate geometry of vertebral bodies and their internal architecture, the toolpath creation software (Stratasys CatalystEX) infilled areas using a soluble support as the analogues were printed. The supports were removed by immersion in NaOH at 70°C for 4 h. We then conducted a test to compare treated and untreated vertebral bodies in order to determine any effects the support cleaning apparatus might have on their mechanical behaviour under quasi-static compression. Figure 5-10 shows the responses of the samples.

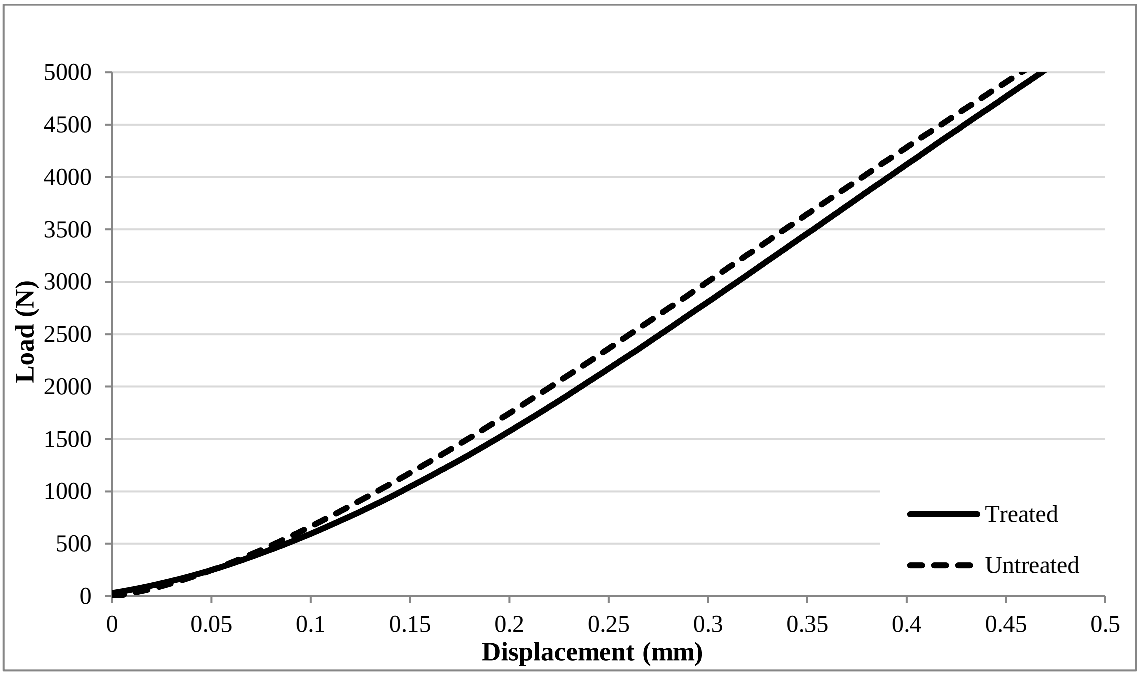

Figure 5-10 Effect of the support cleaning apparatus on artificial vertebral bodies under compressive loading.

The recorded stiffness values were 12,838 and 12,763 N/mm for the treated and untreated samples, respectively. It is unclear whether this small (0.6%) variance is purely due to the response of the support, or whether it includes the effect of the bath on the material or a combination of both factors. It is not currently possible to test the different options directly because the printing software does not allow printing without the support, thus cleaning is an essential process for support removal.

5.4.3 Threshold and low-resolution scanning effects

Resampling was required for the AVBs to mimic the responses of their biological counterparts as previously reported (Franceskides, et al., 2018). The VF was therefore increased, and tests were conducted to determine whether this affected the stiffness of the AVBs and thus their response under loading. Table 5-3 shows the degree to which the VF was altered with respect to the original cadaveric vertebral bodies and the normal AVBs.

Table 5-3 Volume fraction (VF) adjustments based on real vertebral bodies (RVB) and normal artificial vertebral bodies (AVB).

Direction of adjustment		VF adjustment
RVB to	Normal	1.39
	Over	0.84
	Under	1.98
Normal to	Over	1.4
	Under	0.6

The over-threshold and under-threshold specimens were adjusted to represent a change of ±40% in the VF of the normal analogue, and this deviated by +39% from the cadaveric sample. Figure 5-11 shows the responses obtained from the different specimens under the same loading conditions.

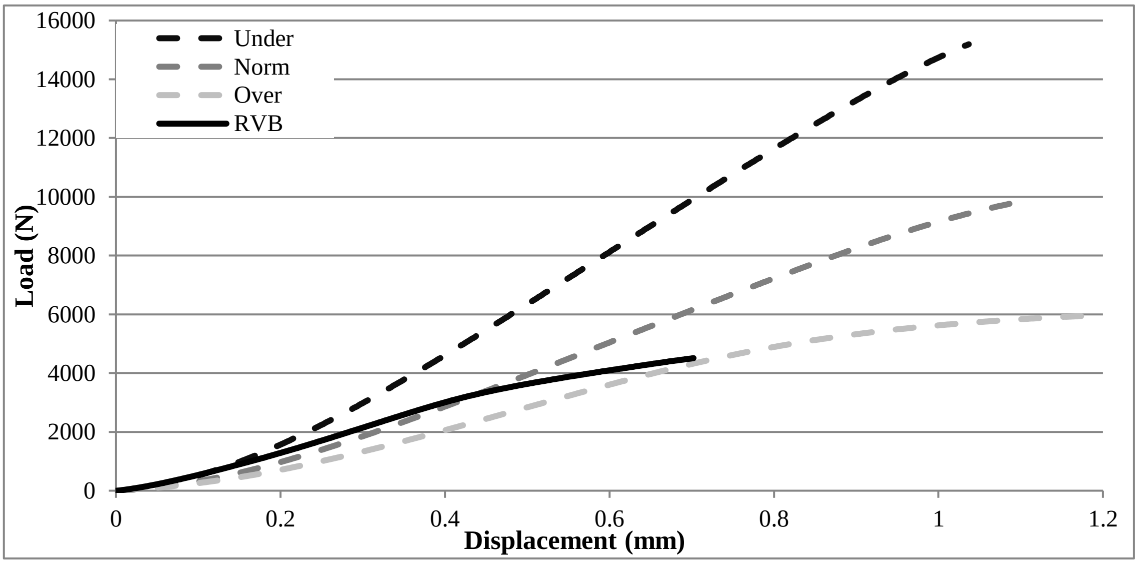

Figure 5-11 Load-displacement curves of normal, over-threshold and under-threshold artificial vertebral bodies compared to a real cadaveric sample.

As expected, the printed specimen with the highest VF was the stiffest, with the normal showing good agreement with the real vertebral body. However, the closest specimen in terms of VF to the real vertebral body was the over-threshold analogue, and as expected this was considerably less stiff than the cadaveric sample (Table 5-4).

Table 5-4 Stiffness values for real vertebral bodies (RVB) and artificial vertebral bodies (AVB).

Specimen	Stiffness N/mm
AVB Over	17,429
AVB Norm	10,808
AVB Under	7775
RVB	9778

This outcome was anticipated because bone is generally stiffer than ABS [(Zioupos, et al., 1999), (Matmatch GmbH, 2018)].

Low-resolution manufactured replicas were based on scans with a voxel dimension of 0.123 mm whereas the normal-resolution replicas had a voxel dimension of 0.063 mm.

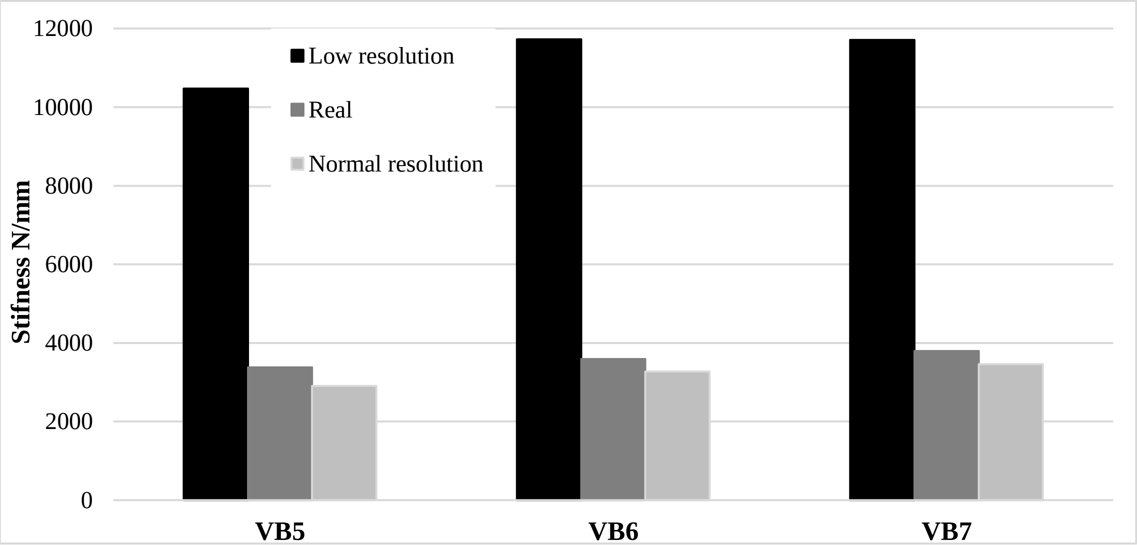

Figure 5-12 Scanning resolution effects for three artificial vertebral bodies compared to a real cadaveric sample.

Figure 5-12 compares the stiffness values of the two analogues to the cadaveric sample. The dramatic increase in stiffness shown for the low-resolution analogue highlights the need for high-resolution CT scanning in order to recreate biofidelic replicas. This sharp increase in stiffness reflects the “bleaching” that occurs within the voxels. With higher scanning capability, darker areas become more evident against a lighter background, but as the voxel size increases so does the merging of the higher and lower GS values, resulting in a less defined geometry. When this is the reproduced by the 3D printer, which has only a single material capability, this bleached area will either be solid ABS or a void. The choice depends on the thresholding values, and whether the GS value falls within the selected range. This explains the increase in VF and consequently the stiffness.

5.4.3.1 Tests of disc and facet joint compositions and facet loading

As previously reported, the IVD plays a significant role in the initial part of the loading of the motion segment and a stiffer material was needed for a more realistic analogue response (Franceskides, et al., 2018). This was achieved by testing two different constitutions of two-part liquid rubber (PT Flex 85 and PT Flex 70), which provided Shore A hardness values of 85 and 70, respectively. Figure 5-13 shows the responses of these materials compared to their cadaveric counterparts.

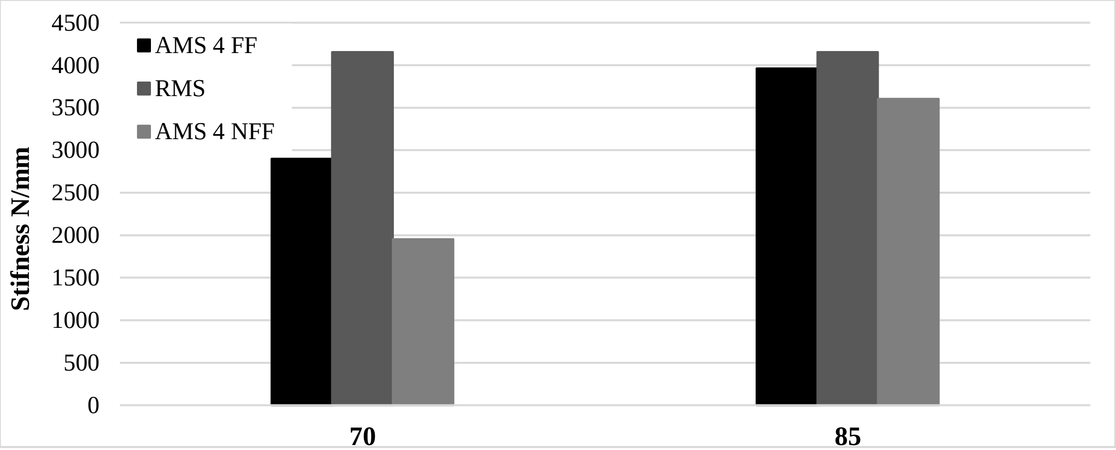

Figure 5-13 Comparison of two-part silicone compositions (PTFlex 70 LHS and PTFlex85 RHS) with and without facet fixation.

In addition, AMS#FF denotes a fixed facet joint (in which the cartilage was simulated with the same grade of liquid rubber used for the IVD) and AMS#NFF denotes a non-fixed facet. When comparing the responses, we found that the facets play a key role in achieving more accurate and realistic representations of real vertebral bodies. Furthermore, PT Flex 85 provided a much better representation of the cadaveric response. This is shown clearly in Figure 5-14, where the force-displacement curve of the biological sample lies between the curves representing the two types of rubber.

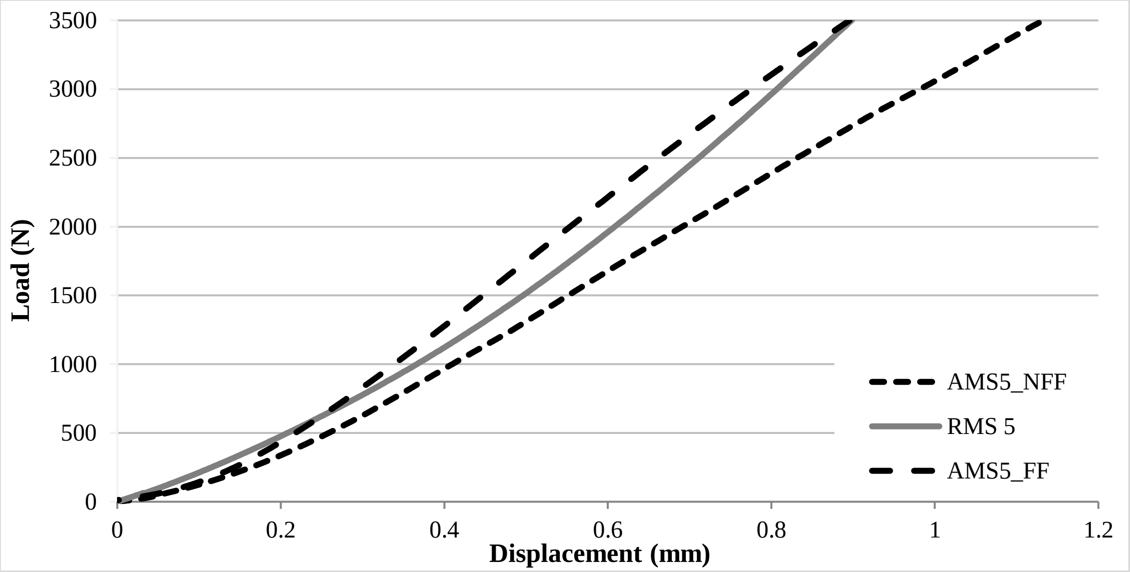

Figure 5-14 AMS5 force-displacement curve with and without facet fixation, compared to a cadaveric motion segment.

All subsequent tests were therefore conducted using PT Flex 85. Figure 5-15 compares the stiffness values obtained using PT Flex 85 with facet fixation (FF) and the absence of facets (NFF).

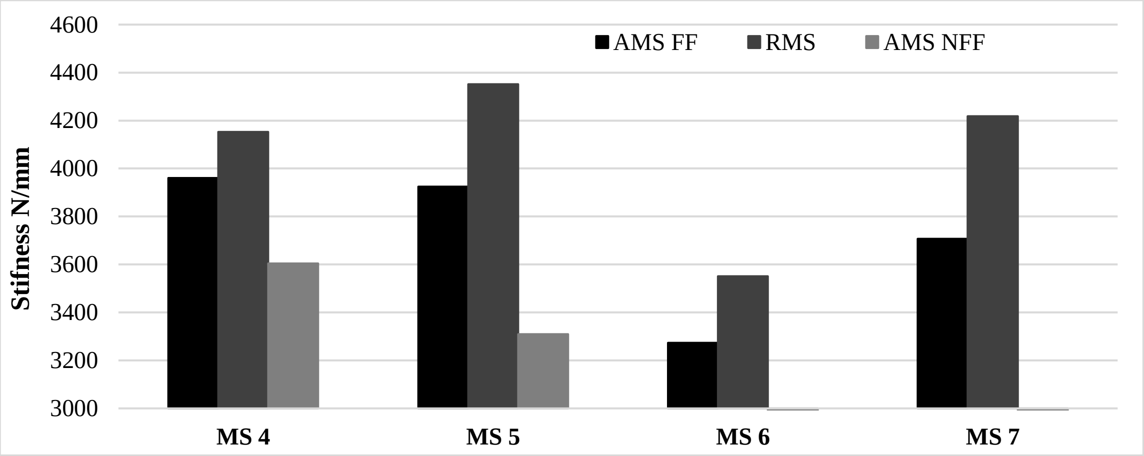

Figure 5-15 Effect of facet fixation on the loading response of four motion segments.

Again, the facet fixation experiment achieved more realistic stiffness values than the NFF analogues. DIC analysis also highlighted the significance of facet fixation in the accurate replication of responses. The analysis of initial loading and displacement with AMS4 revealed that the displacement observed for the whole motion segment (i.e. the vertebral body including the facet joint and IVD) was lower for the FF segment than the

NFF segment. In addition, a sudden peak in displacement occurred after approximately 6000 images, probably representing the stage at which the NFF specimen was compressed beyond the width of the joint and contact was made between the articular processes. The FF sample showed an immediate displacement and the overall displacement was greater than that observed in the NFF specimen (Figure 5-16).

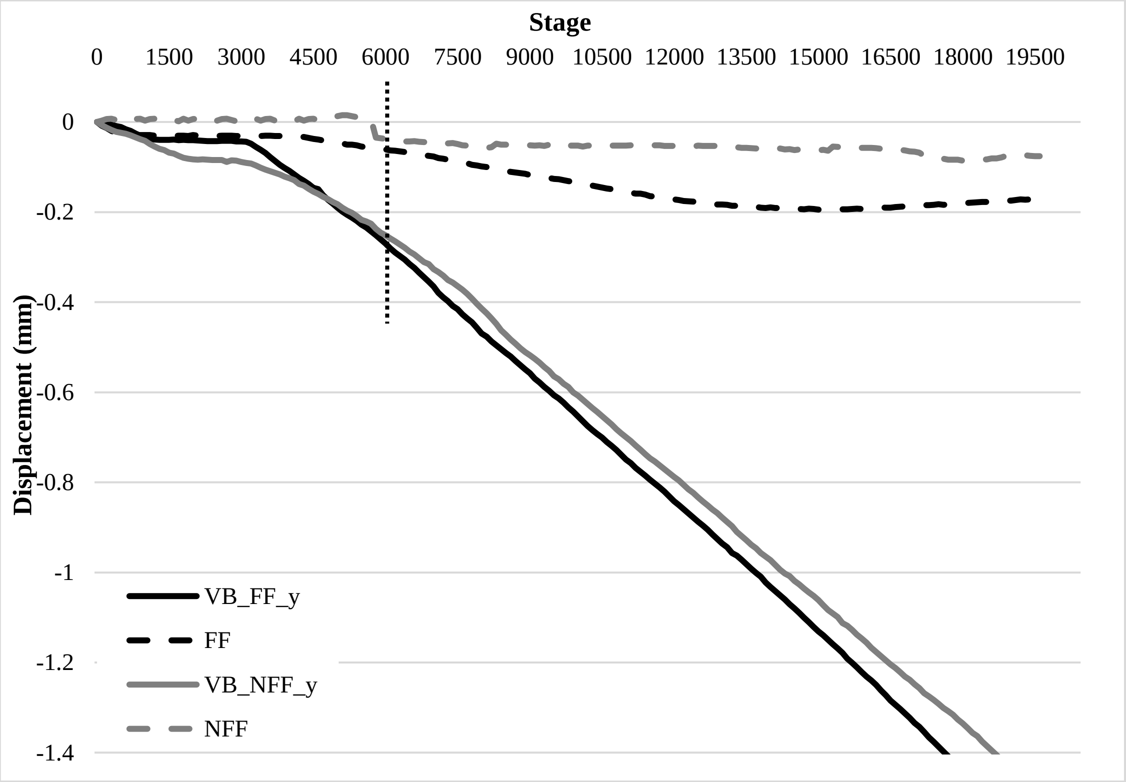

Figure 5-16 DIC analysis of displacements for entire motion segments and their associated facets using fixed facet (FF) and non-fixed facet (NFF) samples.

Finally, Figure 5-17 shows the in-plane displacements observed for the AVB with facet fixation. Although the loading was uniaxial along the *y* axis (compressive), an almost immediate in-plane displacement was detected on the lower AVB of the motion segment. In contrast, the facet displayed in-plane displacements much later, coinciding with the higher displacements along the *y* axis.

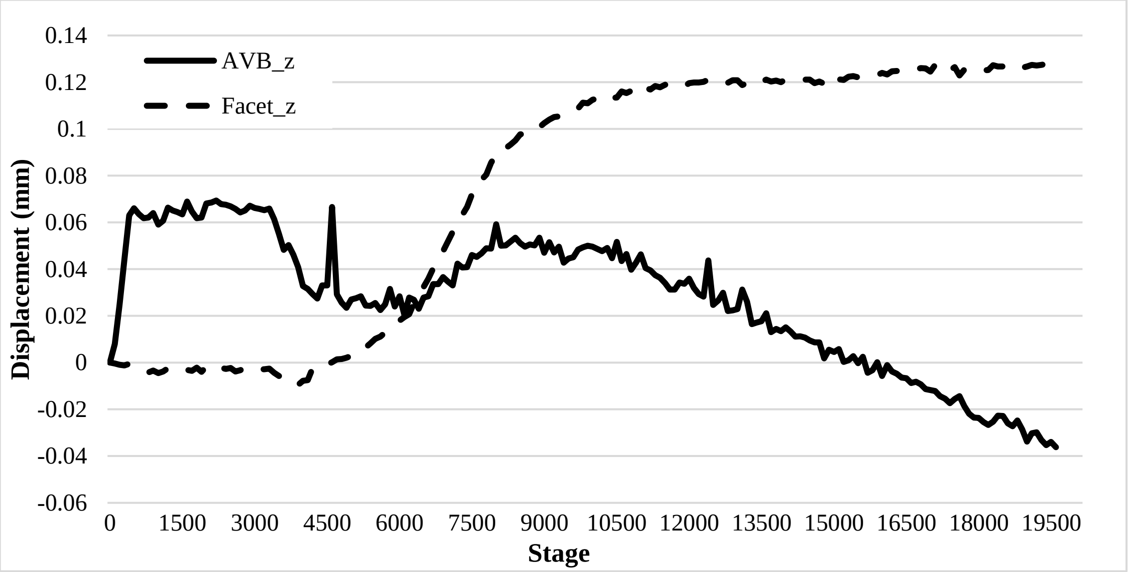

Figure 5-17 In-plane displacements for the bottom of an artificial vertebral body and its associated fixed facet joint.

This is typical of the flexion movement of the spine, indicating that facets respond to loading in an interlinked manner. Although the facet showed increasing displacement, the AVB did not follow the same trend.

5.5 Conclusions

We have demonstrated that it is possible to fine-tune spinal motion segment analogues to obtain better, more biofidelic responses. Our data highlight the suitability of DIC data acquisition techniques, while confirming that any errors are strongly dependent on the settings, with the best results obtained using the point distance to computational-facet size ratio recommended by GOM. In addition, the error trends in the dead-weight experiments showed no conclusive relationship with the variation of the loading conditions.

The accuracy of printed analogues depends on the scanning resolution, given that a low-resolution scan overestimated the VF requirement. This is also true for thresholding techniques, which showed a similar effect to low scanning resolutions. The experiments described herein confirmed that the facet joint plays an integral part in the generation of results that are better and more closely related to real motion segments, and that the simulant used for the IVD should be selected carefully because it has a significant effect on the loading response of the whole segment. Although this research focused on quasi-static loading, it paves the way for the development of rapid, inexpensive, accurate and replicable strategies for the preparation of patient-specific analogues.

5.6 Acknowledgments

We acknowledge the work, skill and expertise of Karl Norris and the mechanical workshop of Cranfield University, Shrivenham, and Jolyon Cleaves of Vision Research for providing the high-speed cameras. Ethical approval was granted by the Cranfield University Research and Ethics Committee (CURES). This paper is dedicated to our friend and colleague Dr Mike Gibson, whose untimely death is a great loss to us all.

5.7 References

Phoenix Analysis & Design Technologies, 2010. *SCA User Manual, Rev1a.,* Tempe, USA: PADT, Inc.

Amiot, F. et al., 2013. Assessment of digital image correlation measurement accuracy in the ultimate error regime: main results of a collaborative benchmark. *Strain,* 49(6), pp. 483-496.

ASTM, 2015. *Standard Test Methods for Spinal Implant Constructs in a Vertebrectomy Model,* West Conshohocken (PA, USA): ASTM International.

Camisa, W., Leasure, J. & Buckley, J., 2014. Biomechanical Validation of a Synthetic Lumbar Spine. *The Spine Journal,* 14(11), pp. 129-130.

Campbell, J., Imsdahl, S. & Ching, R., 2010. *Evaluation of a synthetic L2-L5 spine model for biomechanical testing.* New Orleans, Orthopaedic Research Society.

Domann, J. et al., 2011. The Analogue Spine Model: The First Anatomically and Mechanically Correct Synthetic Physical Model of the Lumbar Spine. *The Spine Journal,* 11(10), pp. 155-156.

Franceskides, C. et al., 2018. *Spinal motion segments: Concept for a subject specific analogue model,* Shrivenham: Cranfield Defence and Security.

Franceskides, C. et al., 2016. *Evaluation of bone excision on occipital area of simulated human skull.* Lyon, European Society of Biomechanics.

Friss, E. A., Pence, D. C., Graber, C. D. & Montoya, J. A., 2003. Mechanical Analogue Model of the Human Lumbar Spine: Development and Evaluation. In: M. N. Melkerson, S. L. Griffith & J. S. Kirkpatric, eds. *Spinal implants: are we evaluating them appropriately?.* STP1431 ed. West Conshohocken: ASTM International, p. 236.

GOM mbH, 2018. *Gom-Correlate.* [Online] Available at: https://www.gom-correlate.com/en/support.php [Accessed 2018].

Jaumard, N. V., Welch, W. C. & Winkelstein, B. A., 2011. Spinal Facet Joint Biomechanics and Mechanotransduction in Normal, Injury and Degenerative Conditions. *Journal of Biomechanical Engineering,* 133(7), pp. 071010-071041.

Lott, B. D., Reece, F. N. & Drott, J. H., 1980. Effect of Preconditioning on Bone Breaking Strength. *Poultry Science,* Volume 59, pp. 724-725.

Matmatch GmbH, 2., 2018. *Matmatch.* [Online] Available at: https://matmatch.com/ [Accessed 2018].

Newell, N. et al., 2017. Biomechanics of the human intervertebral disc: A review of testing techniques and results. *Journal of the Mechanical Behaviour of Biomedical Materials,* Volume 69, pp. 420-434.

Palanca, M., Marco, M., Ruspi, M. L. & Cristofolini, L., 2017. Full-field strain distribution in multi-vertebra spine segments: An in vitro application of digital image correlation. *Medical Engineering & Physics,* Volume 000, pp. 1-8.

Palanca, M., Tozzi, G. & Cristofolini, L., 2016. The use of digital image correlation in the biomechanical area: a review. *International Biomechanics,* 3(1), pp. 1-21.

Pal, G. P. & Routal, R. V., 1987. Transmission of weight through the lower thoracic and lumbar regions of the vertebral column in man. *Journal of Anatomy,* Volume 152, pp. 93-105.

Roberts, S. J., Smith, C. I., Millard, A. & Collins, M. J., 2002. The taphonomy of cooked bone: Characterising boiling and its physico-chemical effects. *Archaeometry,* 44(3), pp. 485-494.

Sawbones, 2012. *Biomechanical Spine Product Research.* [Online] Available at: http://www.sawbones.com/UserFiles/Documents/Product/BioSpine_info.pdf [Accessed February 2018].

Siebert, T., Becker, T. & Spiltthof, K., 2007. Error Estimations in Digital Image Correlation Technique. *Applied Mechanics and Materials,* 7(8), pp. 265-270.

Wang, T., Ball, J. R., Pelletier, M. H. & Walsh, W. R., 2014. Biomechanical evaluation of a biomimetic spinal construct. *Journal of Experimental Orthopaedics,* 1(3).

Wang, T., Ball, J. R., Pelletier, M. H. & Walsh, W. R., 2014. *Initial Experience with Synthetic Spinal Motion Segments: Biomechanical Assessment of High Cycle and Implant Performance.* New Orleans (LA, USA), ORS Annual Meeting.

Wilke, H. J., Krischack, S. & Claes, L. E., 1996. Formalin Fixation Strongly Influences Biomechanical Properties of the Spine. *Journal of Biomechanics,* 29(12), pp. 1629-1631.

Zioupos, P., Smith, C. & Yuehuei, A., 1999. Factors Affecting Mechanical Properties of Bone. In: A. Yuehuei & D. A. Robert, eds. *Mechanical Testing of Bone and the Bone-Implant Interface.* s.l.:CRC Press, pp. 65-85.

CHAPTER 6 PREFACE

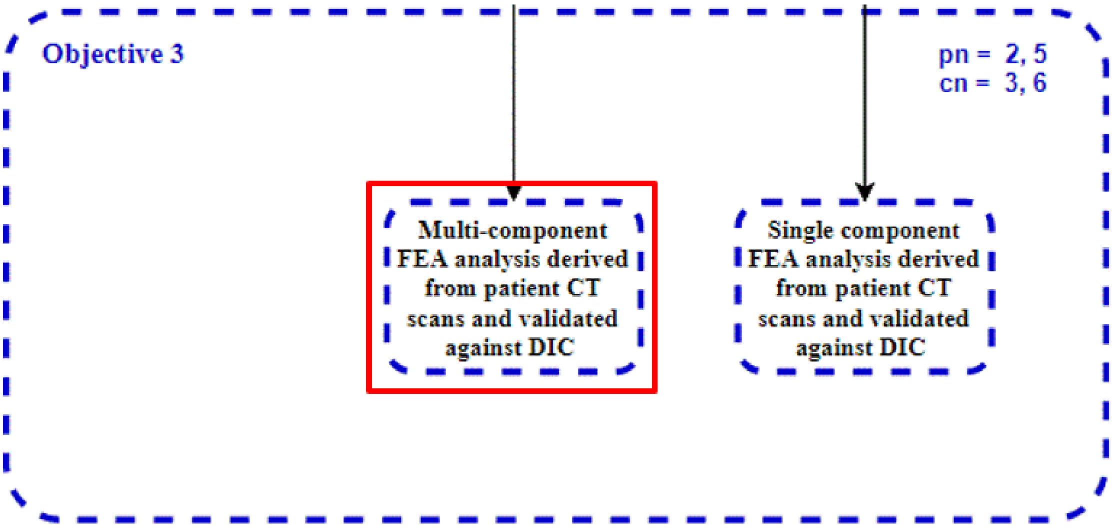

Chapter 5[7] (Paper 4) assessed the techniques developed in Chapters 3 and 4 in more detail, revealing the limitations and quantifying their effects. In addition, it highlighted the variation in the results caused by the addition of joints to the structure, and confirmed the agreement between the model and the original cadaveric specimens.

Finally, Chapter 6 (Paper 5) bridges the knowledge developed in Chapters 3 and 5 by validating a multiscale FEA model against its mechanical counterpart. In addition, the definition of material models is assessed by comparing the output of the FEA model to the empirical data derived from mechanical testing. This final piece of work aims to highlight the synergy among the new methods described in the thesis, namely DIC coupled with the mechanical test data and FEA, to bring a validated and complete body of work to conclusion.

---

[7] Work presented in SAFE US 2017 and ESB 2017 Conferences

6 MULTISCALE MODELLING AND TESTING OF A PORCINE LUMBAR SPINE MOTION SEGMENT ANALOGUE

Constantinos Franceskides[1*], Tobias-Akash Shanker[1], Michael Gibson[2], Peter Zioupos[1]

[1]*Musculoskeletal and Medicolegal research Group, Cranfield Forensic Institute, Centre for Defence Engineering, Cranfield University, Defence Academy of the UK, Shrivenham, SN6 8LA, UK*

[2]*Centre for Simulation & Analytics, Centre for Defence Engineering, Cranfield University, Defence Academy of the UK; Shrivenham, SN6 8LA, UK*

6.1 Abstract

Computed tomography and magnetic resonance imaging data could in principle be used to create patient-specific analogues and FEA models mimicking soft and hard tissue properties both anatomically and mechanically. However, there is still a gap between the perfect biofidelic analogue and its computational counterpart because *in silico* models are often too complex to realise, and real-life conditions are difficult to emulate using either computational or mechanical analogues. Here, we applied a multiscale approach to design and model porcine vertebral specimens. Manufactured ABS cores were compared under compressive loading with their biological counterparts using finite element modelling, while asserting the effect different material models have to the end result. Our results revealed the important design factors affecting the quality of the models, specifically that scanning resolution/fidelity and the thresholding technique have a direct proportional impact on model accuracy. Our data indicated good agreement between the physical and *in silico* models and confirmed that it is possible to model real-time objects and situations both physically and *in silico*. Although more work is required to model the more intricate parts of spinal motion segments such as the intervertebral discs, our method based on finite element analysis will allow the development of accurate, patient-specific spinal analogues for biomechanical testing.

Keywords Multiscale modelling · Lumbar · Digital image correlation · 3D printed analogue

6.2 Introduction

The combination of additive manufacturing with increasing computational power has introduced a new concept in the development of biomechanical and computational analogues, allowing the creation of robust *in silico* models that overcome the complex practical and ethical procedures concerning the use of cadavers. Finite element analysis (FEA) in particular has facilitated the characterisation and testing of different components of the musculoskeletal system (Grassi, et al., 2013). This evolution in computational and screening techniques has driven research towards complex and unknown territory (McDonald, et al., 2010) where bone macro-modelling is increasingly supplanted by highly-detailed and resource-heavy micro-scale models (Helgason, et al., 2016). The creation of biofidelic models, whether *in silico* or in real life, is more complex when investigating intricate geometries where the interactions between different subcomponents (such as soft and hard tissues) play a key role (Lee, et al., 2017). The reliability of such models depends heavily on how they are defined, interpreted and implemented for each application. These definitions are based on approximations and compromises limited by technical and resource constraints such as 3D printing resolution, scanning capability and the trade-off between computational speed and accuracy.

In spine biomechanics, motion segment analogues have been produced with varying levels of success [(Barr, et al., 2014), (Campbell, et al., 2010)]. Outsourcing the development of custom analogues requires several months of lead time and involves prohibitive costs, which limits their accessibility. These analogues are produced mostly for demonstration and training purposes, and as such do not fully simulate the mechanical behaviour of the natural parts they represent. Biofidelic copies of vertebrae and spine motion segments have been validated by quasi-static compression loading *in vitro* (Franceskides, et al., 2017). The 3D-printed analogues were created using readily available and off-the-shelf materials with known mechanical properties, namely acrylonitrile butadiene styrene (ABS) for the vertebral body and a two-part liquid polyurethane rubber system for the intervertebral disc (IVD) and the superior and inferior process ligaments.

The potential of FEA for the modelling and validation of 3D-printed spinal analogues under quasi-static loading (0.01 mm/s) can be investigated using a bottom-up approach instead of the top-down strategy applied in other multiscale studies (Hambli, 2013). This would allow us to determine the lowest fidelity needed to provide an effective method for the validation of the physical model, thus reducing the costs and lead time for a patient-specific FEA solution. A biofidelic finite element model must be fed with material properties in order to calculate accurate stresses and strains. The assignment of these properties at the micro-scale requires some form of observation or measurement at this level, which usually involves a surrogate physical variable such as the micro-CT greyscale (GS). This is dependent on the linear attenuation coefficient of the material, which is linked to the material density.

In order to generate a material model for ABS over a wide applicable range (micro to macro) there needs to be a discernible variation in the average GS values between samples. Here we achieved this in three steps by testing specimens with (1) longitudinal holes in solid cores (longitudinal cores); (2) solid, high-density and low-density filled cores (transverse cores); and (3) artificial vertebral cores (AVCs) with varying threshold levels. The most accurate material model was selected and applied to higher-scale segments: (1) an artificial vertebral body (AVB); and (2) an artificial motion segment (AMS), as described in our previous work (Franceskides, et al., 2017). We investigated the best practices for generating an FEA model of a physical analogue suitable for multiscale analysis, ultimately aiming to facilitate the development of patient-specific bone analogues which can be used in orthopaedic and biomechanical applications.

6.3 Methodology

6.3.1 Outline

Main objective within this body of work was to ascertain the difference material models have to the efficacy of the computational results.

Different material models were created, some more complex than others, and these were then compared between them and the experimental data. For the more simple, regular components, cores were created, printed and scanned in an effort to ensure as true representation in the mechanical testing as in the computational models. Biological components were also scanned, with cores created from their internal structure. These were also printed and rescanned for similar reasons as outlined above.

6.3.2 Sample preparation

All samples were printed using a fused deposition modelling (FDM) UPrintSE printer (Stratasys Inc., Eden Prairie, MN, USA), based on computer aided design (CAD) geometry samples at 100 µm, a scale that achieves mechanically accurate 3D-printed replicas of biological objects (Franceskides, et al., 2018). Tool paths for 3D printing were generated using CatalystEX v4.5 (Stratasys Inc.).

The cores with longitudinal holes (Figure 6-1A) were created using SolidWorks 2018 SP1 (Dassault Systèmes SolidWorks Corporation, Vélizy-Villacoublay, France). For these samples, the diameter of the hole was kept constant at 2 mm but the number of holes varied (0, 1, 3, 5 or 7).

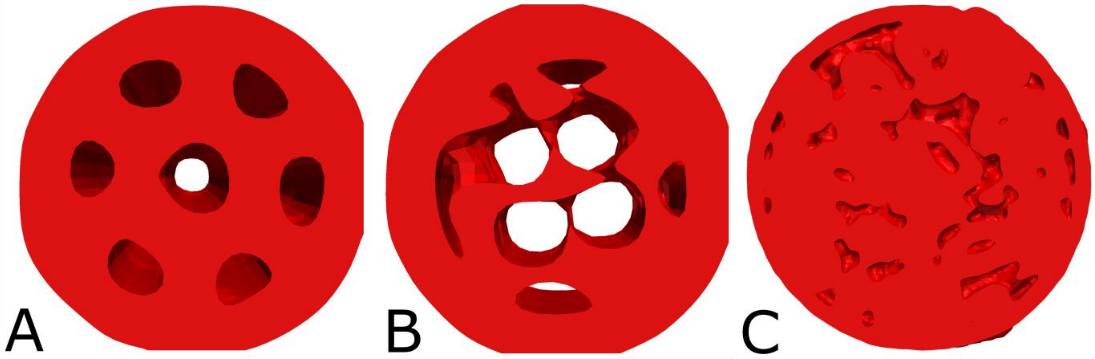

Figure 6-1 Examples of (A) longitudinal, (B) transverse and (C) artificial vertebral cores.

The transverse cores with varying fill distribution (Figure 6-1B) were created by modelling a solid cylinder and using CatalysEX to select three different default fills: solid, high density or low density. Using these settings, the external structure was printed as a solid whereas the density of the internal structure was varied by controlling the amount of fill, achieving a more even density variation throughout the cylinder (particularly in the *x* and *y* planes) compared to the longitudinal cores. Both the longitudinal and transverse cores were 9 mm in diameter and 25 mm long to maintain comparability between test results. The data from the longitudinal and transverse cores were pooled (LTCs) for broader density variation and to improve the population size in comparison to the AVCs.

The AVCs were generated by segmenting micro-CT scans from two cadaveric porcine motion segments (real motion segments, named RMS4 and RMS5) obtained in our previous studies ((Franceskides, et al., 2018), (Franceskides, et al., 2018)). These were derived from two porcine vertebrae at levels L1–L2 and T12–L1, respectively (Figure 6-1C). The cores were taken from a cylindrical region of interest, 9 mm in diameter and aligned with the axis of loading, from the central portion of the top and bottom vertebrae. The lengths were limited by the total vertebral height without including the endplates, such that the AVCs were shorter than the longitudinal and transverse cores. Core density was varied by controlling the amount of bone thresholded compared to the baseline. Models with a threshold GS value of ±20 in relation to the baseline were generated in addition to the standard upper/lower peak thresholding procedure. Figure 6-2 shows an example of the segmentation. A thin shell of solid ABS was added to the edge of the cores as shown in blue to prevent tool path generation errors in the now discontinuous samples.

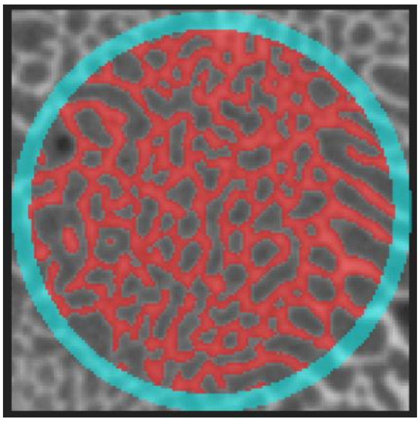

Figure 6-2 Artificial vertebral core segmentation with outer shell.

The AVCs were bathed, prior to scanning, in a Support Cleaning Apparatus (PADT Inc., Tempe, AZ, USA). This ensured that all the internal support was removed without damaging or affecting the rest of the structure. Once all the support was removed, samples were scanned at the same resolution and settings as for the longitudinal and transverse cores.

AVB samples were based on micro-CT image stacks obtained from six porcine vertebral bodies. The entire vertebral body was sectioned, removing the endplates, vertebral arch and pedicles.

The AMS analogue was based on RMS4 and was created using the same method as the AVB samples with one exception: IVD and facet joints were introduced that fused the top and bottom vertebral bodies.

The IVD and intra-facet cartilage (area between facet joints) were formed from PT Flex 85 liquid rubber of Shore A hardness 85 (Polytek Development Corp., Easton, PA, USA). The two-part rubber was mixed and then injected into a cast built around the IVD superior and inferior endplates and the superior and inferior articular processes, using Sugru mouldable glue (FormFormForm Ltd, London, UK). Accurate IVD thickness (based on CT reconstructions) was ensured by placing struts equal in height to the IVD (also produced using PT Flex 85) at three points on the endplates.

Once curing was complete, the Sugru mould was removed entirely, allowing component to further cure between the Sugru-silicone interface.

Finally, Castrol White Contrast Paint 710 (2386) non-strippable aerosol was used to apply the high-contrast background evenly over the model surface.

Figure 6-3 shows the completed sample following the injection of the IVD and facet ligaments and the white contrast application.

Figure 6-3 Artificial motion segment surface model and finished sample.

. These were scanned using a CT H225 cone beam μCT scanner (Nikon Metrology UK Ltd, Tring, UK) operated at 80 kV and 65 μA. Noise reduction and beam hardening were achieved using CT Pro 3D (Nikon Metrology UK Ltd). The geometric magnification produced a voxel dimension of 26 μm for all the cores, 55 μm for the AVBs and 89 μm for the AMS experiment.

In turn, Figure 6-4 shows all the analogues we tested

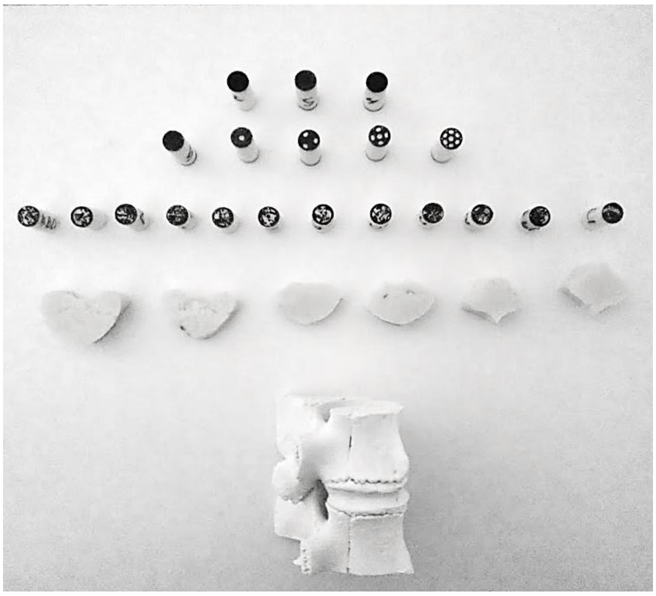

Figure 6-4 Porcine spinal analogues. From the top, the image shows the 3 transverse cores, 5 longitudinal cores, 12 AVC cores, 6 vertebral bodies and finally a complete motion segment.

The data generated during the scans were used for finite element modelling and morphometric analysis. ImageJ (Schneider, et al., 2012) with the BoneJ (Doube, et al., 2010) plugin was used to calculate the GS values of the ABS peak and air peak as well as the volume fraction, degree of anisotropy and mean GS through the entire cylinder. Table 6-1 shows the volume fraction and weight of the LTC samples.

Table 6-1 Volume fraction and weight of the longitudinal and transverse cores (LTCs).

	Samples	**Volume fraction**	**Weight (g)**
1	Solid	0.999	1.507
2	0 Holes	0.998	1.503
3	1 Hole	0.916	1.386
4	High density	0.907	1.301

5	3 Holes	0.843	1.290
6	5 Holes	0.773	1.168
7	7 Holes	0.736	1.062
8	Low Density	0.624	1.006

Table 6-2 shows the allocation of cores from the original specimens, highlighting parameters such as the volume fraction, weight, volume and length.

Table 6-2 Properties of artificial vertebral cores.

Motion segment	**Vertebral body**	**Core section**	**Volume fraction**	**Mass (g)**	**Volume (mm^3)**	**Length (mm)**
RMS_4	RVB4_T	4BN	0.787	1.05	1059.22	20.61
		4BO	0.568	0.83	802.082	20.27
		4BU	0.929	1.23	1217.84	20.52
	RVB4_B	4TN	0.836	1.10	1066.75	19.87
		4TO	0.76	0.99	978.78	19.90
		4TU	0.92	1.21	1183.93	19.86
RMS_5	RVB5_T	5BN	0.715	0.88	842.64	18.00
		5BO	0.594	0.76	727.21	17.98
		5BU	0.817	1.00	972.45	17.99
	RVB5_B	5TN	0.722	0.89	872.24	17.35
		5TO	0.696	0.83	795.44	17.05
		5TU	0.83	0.96	916.46	17.37

6.3.3 Mechanical testing

All analogues were tested under compression in a Dartec Series HC25 servo-hydraulic testing machine (Dartec Ltd, Stourbridge, UK) with a 9610 controller running on Workshop 96 (Dartec Ltd). The tests were conducted from rest to plastic failure (or force limit of the load cell, whichever came first) under crosshead displacement control at 0.01 mm/s. The forces were logged using a 5-kN load cell (Sensotec, RDP Electronics Ltd, Wolverhampton, UK). The core specimens were located in the endcaps. The bottom endcap was fixed whereas the top endcap featured a self-levelling platen (Figure 6-5).

Figure 6-5 Mechanical testing setup with the top spherical joint endcap platen and the bottom fixed endcap platen.

In the AMS experiment, the loading was delivered using a flat, spherical-joint, self-levelling platen at the top and a fixed, flat platen at the base, whereas the AVBs were fixed between an endcap, spherical-joint platen at the top and a fixed-endcap platen at the base.

6.3.4 Finite element model

The CT images were segmented using Simpleware ScanIP M-2017.06-SP2 (Synopsys Inc., Mountain View, CA, USA). CT scans were resampled to 100 μm for consistency between meshes. The outer surface of all samples was identified using standard thresholding techniques and filled to create a homogenous structure. The meshes were generated using quadratic 10-node tetrahedral elements in the *FE-Free* meshing routine of Simpleware ScanIP at the coarsest setting (–50) to reduce the computational cost of the models as much as possible, allowing analysis on less capable machines often found in a clinical environment. The average GS air peak and the measured apparent density (Adams, 2017) were used to draw a linear relationship between the GS and apparent density (Figure 6-6).

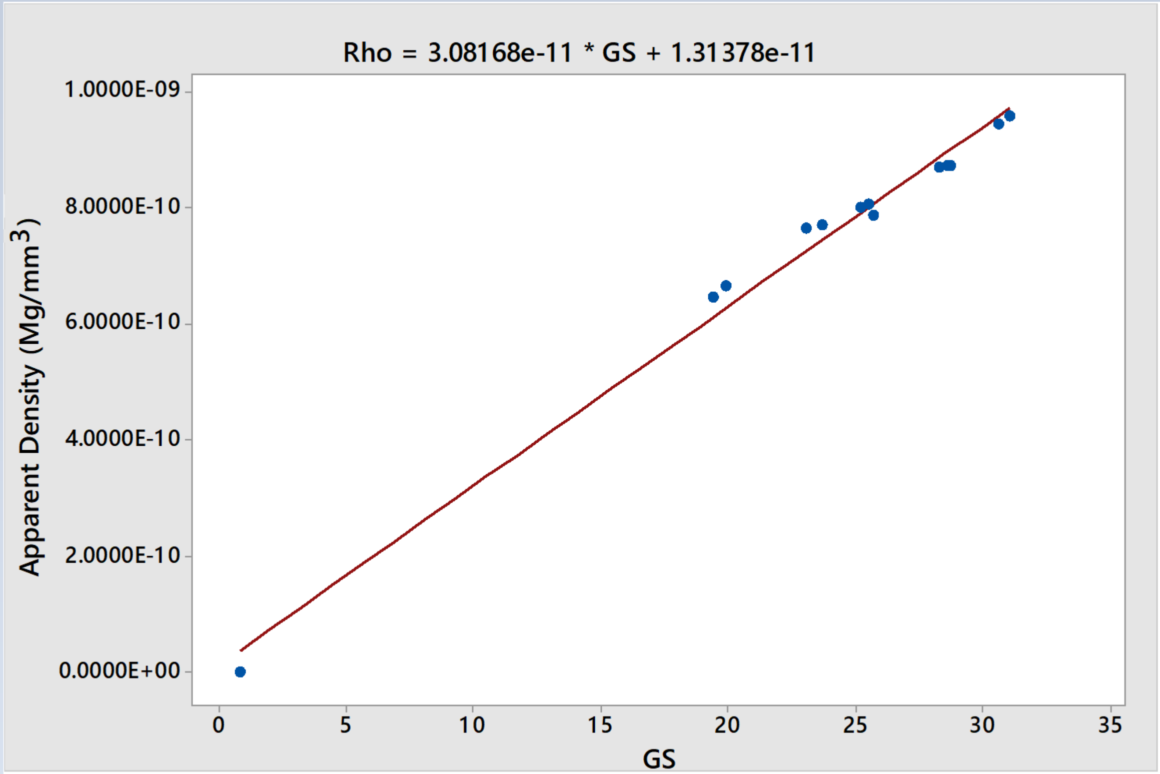

Figure 6-6 Artificial core apparent density plotted against grey scale (GS).

The relationship between density and elastic modulus was described using a fitted power law curve (Figure 6-7) similar to that reported for trabecular bone samples (Keaveney & Hayes, 1993).

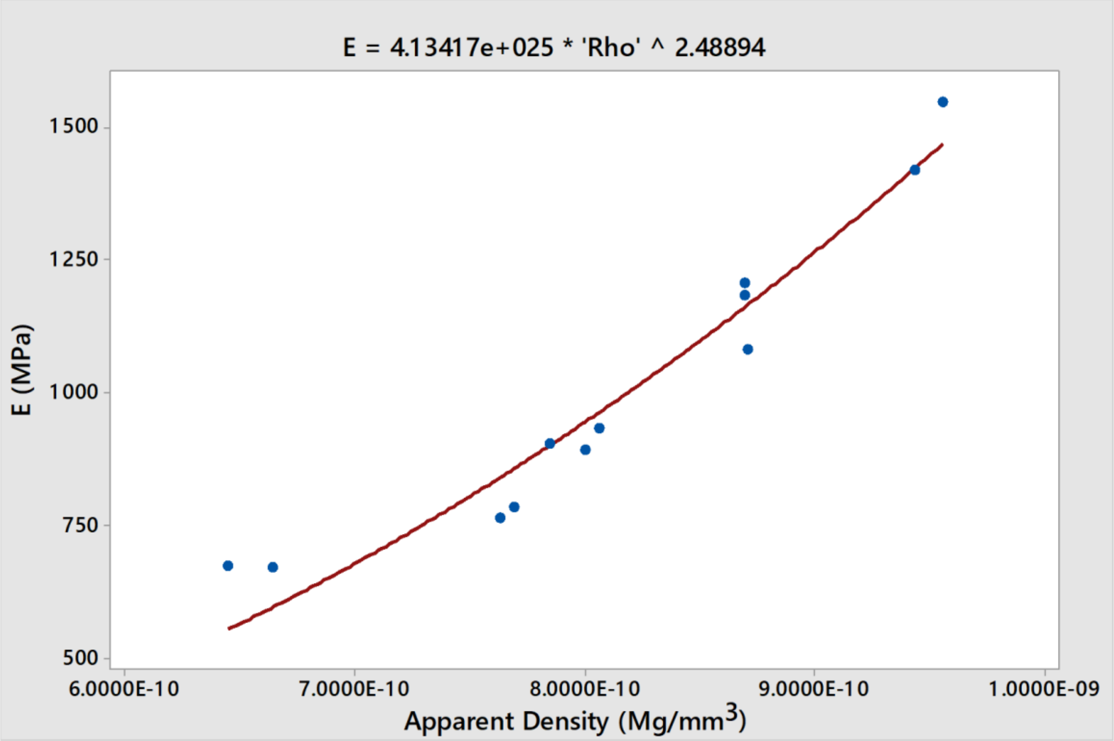

Figure 6-7 Artificial core elastic modulus plotted against apparent density.

This was done twice, once for the LTC and again for the AVC samples. A Poisson’s ratio of 0.35 [(Rodríguez, et al., 2001), (Dreisharf, et al., 2014)] was applied to complete the linear elastic model for the bone analogues. The AMS included an additional analogue two-part rubber IVD modelled with an elastic modulus of 2.5 MPa and a Poisson’s ratio of 0.49, a value at the limit for linear elastic materials in ANSYS and more representative of the nucleus pulposus and the annulus ground substance than the inner and outer fibrous structures (Kuo, et al., 2010). Two material models were created, one (MLC) based purely on the ABS idealised longitudinal cores and another (MT-DLS) on the AVCs. Their relationships and material properties are compared in Table 6-3.

Table 6-3 ANSYS mechanical properties of idealised and artificial vertebral cores (AVCs). ABS = acrylonitrile butadiene styrene; IVD = intervertebral disc.

Material type	**GS-density relationship (Mg/mm^3)**	**Elastic modulus (MPa)**	**Poisson ratio**
ABS (idealised geometry)	$(3.098 \times 10^{-11} * GS) - (7.15 \times 10^{-12})$	$1.244e19*\rho^{1.752}$	0.35
ABS (AVCs)	$(3.082 \times 10^{-11} * GS) + (1.31 \times 10^{-11})$	$4.135e25*\rho^{2.489}$	0.35
IVD	N/A	2.5	0.49

The models generated for all cores (LTCs and AVCs) comprised ~15,000 elements and were analysed using ANSYS APDL v15.0 (ANSYS Inc., Canonsburg, PA, USA) with an implicit solver. The top face was coupled to replicate the effects of a platen and displaced by 1 mm, whereas the bottom face of each specimen was fixed in all directions. The nodal reaction forces on the top face were computed to provide a stiffness measurement for validation against the mechanical testing.

6.4 Results and discussion

Accurate patient-specific finite element models and their analogues are needed in the fields of forensic and injury biomechanics as well as orthopaedics. Micro-CT data were used to develop analogue models of porcine spinal motion segments and subsequent FEA models. These were then tested in a similar manner to compare their stiffness and reaction forces. Clinical CT scanning is currently conducted at 300–500 µm (Burghardt, et al., 2011) which is a much lower resolution than the image segmentation used for the FEA in this study (100 µm). Our scans produced a more accurate FEA model because there were more data on which to base the model. The discrepancy between *in vivo* and *in vitro* CT scanning resolution could be a limiting factor for the clinical application of this model.

The arithmetic mean and standard deviations for the morphological results of the samples are shown in Table 6-4**.**

Table 6-4 Comparison of morphometric data for artificial vertebral cores (AVCs) and longitudinal and transverse cores (LTCs) with asterisks indicating significant differences.

	LTC		AVC		AVC Sub	
	Mean	**Std. Dev**	**Mean**	**Std. Dev**	**Mean**	**Std. Dev**
Length (mm)	25.15*	0.13*	18.89*	1.32*	18.95*	1.33*
Volume fraction	0.855	0.12	0.76	0.11	0.77	0.05
D_{app} (Mg/mm^3)	7.96E-10	1.07E-10	8.12E-10	9.27E-11	8.12E-10	3.71E-11
Degree of Anisotropy	0.99*	0.02*	0.31*	0.10*	0.31*	0.03*

To compare the morphometry with that of porcine trabecular bone, the four AVCs thresholded using the standard method (4BN, 4TN, 5BN, 5TN) were subsampled (AVC-Sub), and two-sample t-tests were used to calculate significant differences in relation to LTCs ($\alpha = 0.05$). The AVC and AVC-Sub samples featured virtually indistinguishable means, therefore in this context they could be used interchangeably. Length was consistent for the LTCs but there was greater variation in the AVC and AVC-Sub samples. The volume fraction was 8% higher on average for the LTCs but showed greater variance than AVC and AVC-Sub. The apparent density of the two models was similar, and showed inter-specimen correlation when normalised against volume fraction (6.76 x 10^{-10} LTC, 6.21 x 10^{-10} AVC). The LTC dataset was mostly anisotropic (close to 1) whereas the AVC dataset showed a much more orthotropic construction (0.305). Figure 6-8 shows the variance in the experimental elastic modulus for the different vertebral bodies and its dependence on the thresholding method, revealing a nonlinear relationship between the –20 and +20 GS.

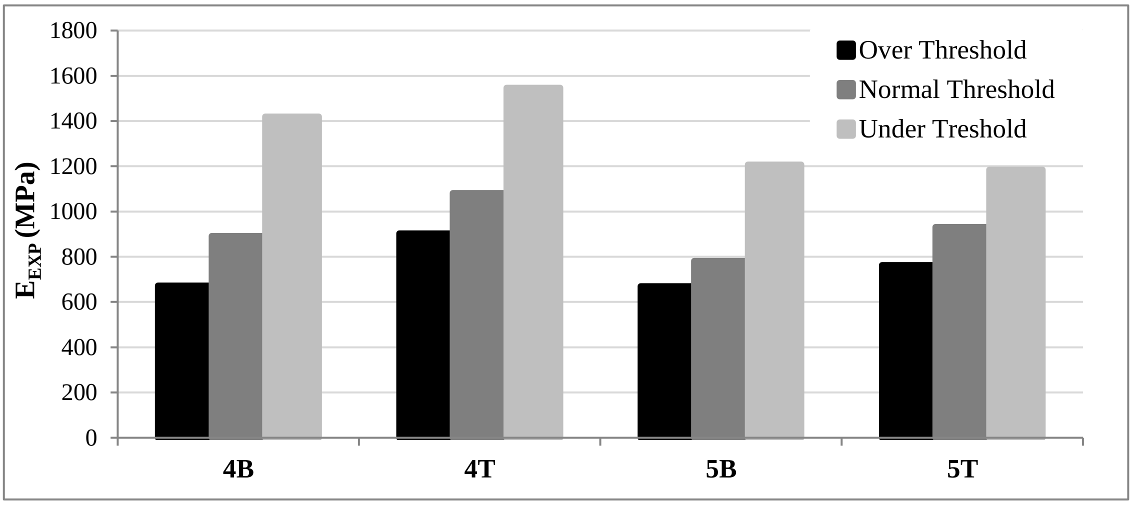

Figure 6-8 Experimentally obtained stiffness (E_{EXP}) with varying thresholds.

The morphometric data shown in Table 6-4 reveal several trends. The AVC and AVC-Sub data have similar arithmetic means but the AVC-Sub data have a much smaller standard deviation. This is expected because the population has been reduced from 12 to 4 but is segmented in the same manner, reducing the morphological variance. It also shows the different thresholding methods have a linear effect on morphological measurements. This is in contrast to the nonlinear mechanical relationship between the thresholding techniques (Figure 6-8).

The apparent density is controlled by the threshold value applied during segmentation. Our model shows a nonlinear relationship between apparent density and experimental elastic modulus, which is reflected in the power exponent in the fitted material model

($\rho_{app}^{2.489}$, R^2=0.9441) which is in the range of previously reported bone FEA models ($\rho_{app}^{1.49}$- ρ_{app}^{3}) (Helgason, et al., 2016).

The degree of anisotropy for the LTCs was close to 1 ± 0.016 (mean ±SD), whereas the AVCs showed a lower degree of anisotropy (0.305 ± 0.0925). This is similar to previously reported porcine vertebral anisotropy values of 0.321 ± 0.067 (Zapata-Cornelio, et al., 2017). There was no significant difference in apparent density between the LTC and AVC samples (two-sample t-test, $p = 0.754$) and when normalised against volume fraction the mean values were much closer (6.76×10^{-10} LTC, 6.21×10^{-10} AVC) showing that there is little variance in the 3D-printing procedure which could affect the mechanical results. Furthermore, no significant differences in volume fraction were observed between the cores. Therefore, both sets had a similar spread of volume fractions, indicating that other morphological properties affect the mechanical response and model characteristics.

Bone has a higher elastic modulus than ABS (10–20 GPa vs 3 GPa) so more material is needed to achieve a mechanically comparable model (Franceskides, et al., 2018). As previously recommended (Laffosse, et al., 2010), we measured the bone volume divided by the total volume (BV/TV) of porcine vertebrae in the range 0.30–0.40, whereas the cores used in this study were 0.80 ± 0.12 overall and the AVBs were 0.82 ± 0.98. Given the lower elastic modulus of ABS, higher BV/TV values are necessary in bone analogues and were therefore adjusted so that the models achieved a similar stiffness upon loading (Franceskides et al. 2018).

The *in silico* and experimental stiffness results for the longitudinal and transverse cores showed good agreement. We obtained two computational stiffness values, one using model MT-DLS and the other using model MLC (Table 6-5).

Table 6-5 Longitudinal and transverse core stiffness results. K = stiffness. Exp = experimental value. FEA = finite element analysis value. MT-DLS and MLC are material models.

Sample	Volume fraction	Weight (g)	K_{EXP} (kN/mm)	$K_{FEA\ (MT\text{-}DLS)}$ (kN/mm)	$K_{FEA\ (MLC)}$ (kN/mm)
Solid	0.999	1.507	3.917	3.710	4.978
0 Holes	0.998	1.503	3.084	2.909	4.997
1 Hole	0.916	1.386	3.569	3.339	4.036
High density	0.907	1.301	3.113	3.020	3.947
3 Holes	0.843	1.290	2.623	2.262	4.587
5 Holes	0.773	1.168	4.044	3.945	4.167
7 Holes	0.736	1.062	2.975	2.818	3.311
Low density	0.624	1.006	2.294	1.692	2.482

Model MT-DLS predicted the stiffness with a variance of 8.56% (under-prediction) whereas model MLC over-predicted the stiffness, with an average variance of 28.29%.

Figure 6-9 compares the computed stiffness values of the two material models against the experimental values for the longitudinal cores.

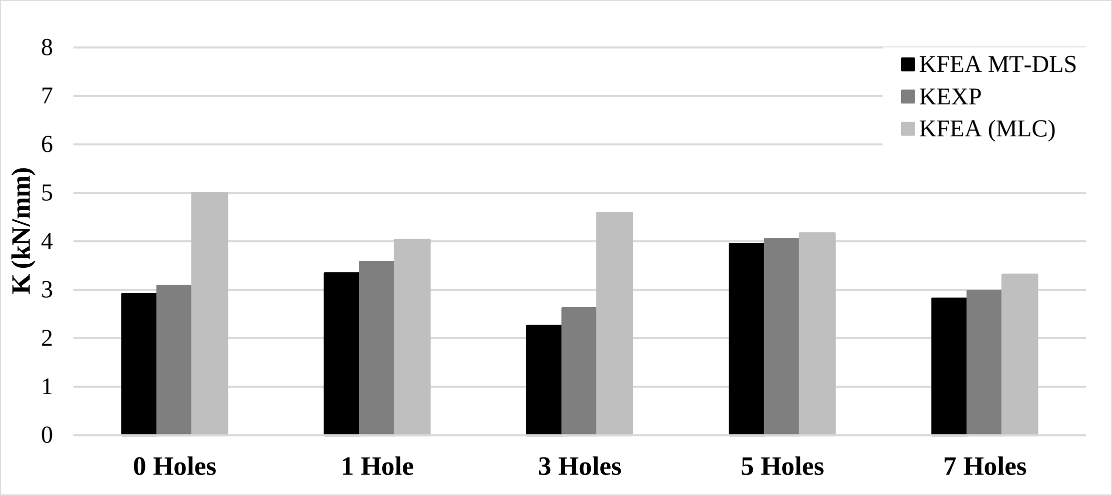

Figure 6-9 Longitudinal core MT-DLS and MLC material models. FEA-derived stiffness (K_{FEA}) plotted against experimentally determined stiffness (K_{EXP}).

Likewise, Figure 6-10 shows the comparative stiffness values of the transverse cores.

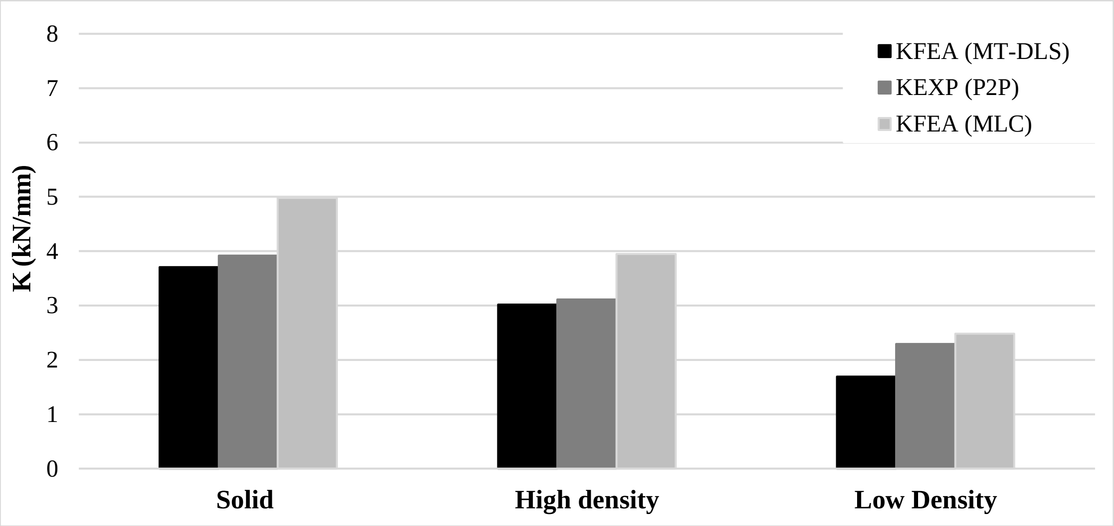

Figure 6-10 Transverse core MT-DLS and MLC material models. FEA-derived stiffness (K_{FEA}) plotted against experimentally determined stiffness (K_{EXP}).

Table 6-6 summarises the stiffness results for AVCs (using the data from Figure 6-9 and Figure 6-10) and shows a 3.09% average over-prediction of stiffness when comparing the MT-DLS material model to the experimental data.

Table 6-6 Artificial vertebral core stiffness results. BV/TV = bone volume divided by the total volume. K = stiffness. Exp = experimental value. FEA = finite element analysis value. MT-DLS and MLC are material models (T=Top, B=Bottom, N=Normal, O = Over, U = Under).

Core	BV/TV	K_{EXP} (kN/mm)	$K_{FEA\ (MT\text{-}DLS)}$ (kN/mm)	$K_{FEA\ (MLC)}$ (kN/mm)
4BN	0.787	2.725	2.879	4.525
4BO	0.568	2.313	2.172	2.821
4BU	0.929	4.635	5.467	6.973
4TN	0.836	3.59	3.636	5.253
4TO	0.76	2.947	3.029	4.71
4TU	0.92	5.127	4.948	6.314
5BN	0.715	2.79	2.973	4.773
5BO	0.594	2.496	2.538	5.364
5BU	0.817	4.268	4.276	6.107
5TN	0.722	3.474	3.433	5.435
5TO	0.696	2.898	3.276	5.128
5TU	0.83	4.5	4.701	6.28

A similar tendency was observed with the MLC material model, albeit with a much larger average variance of 34.53%.

Based on the comparative analysis of the stiffness values, the MLC model consistently underperformed compared to the MT-DLC model, possibly reflecting the fact that the

MLC model was based on fewer samples (eight in total, with five showing very distinct transverse morphologies).

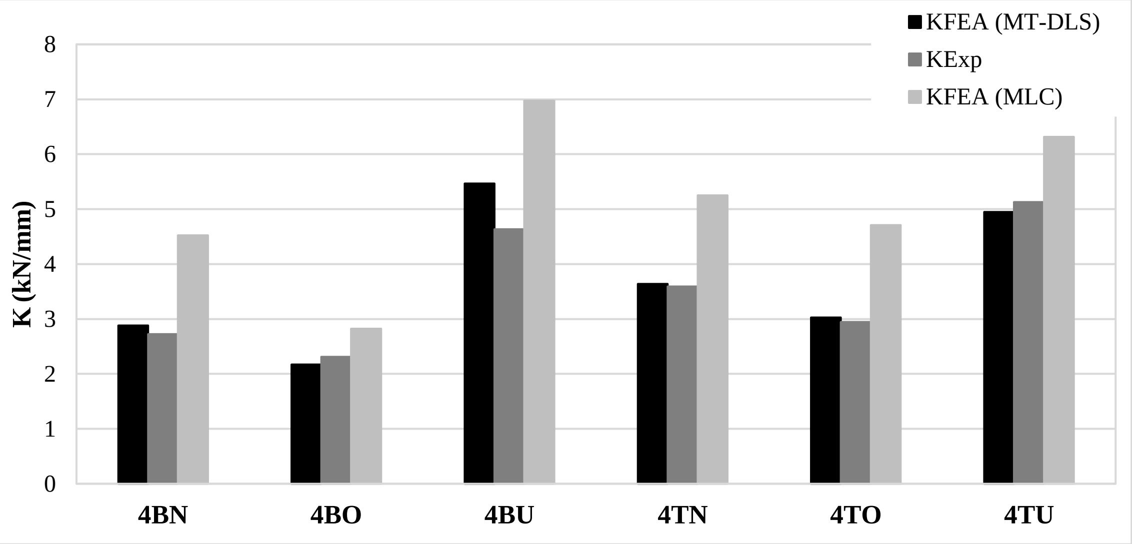

Figure 6-11: AVC4 core MT-DLS and MLC material models. FEA-derived stiffness (K_{FEA}) plotted against experimentally determined stiffness (K_{EXP}).

In contrast, the MT-DLC model was derived from 12 points obtained from accurate replicas of the 3D printed structure, with greater variation of anisotropy.

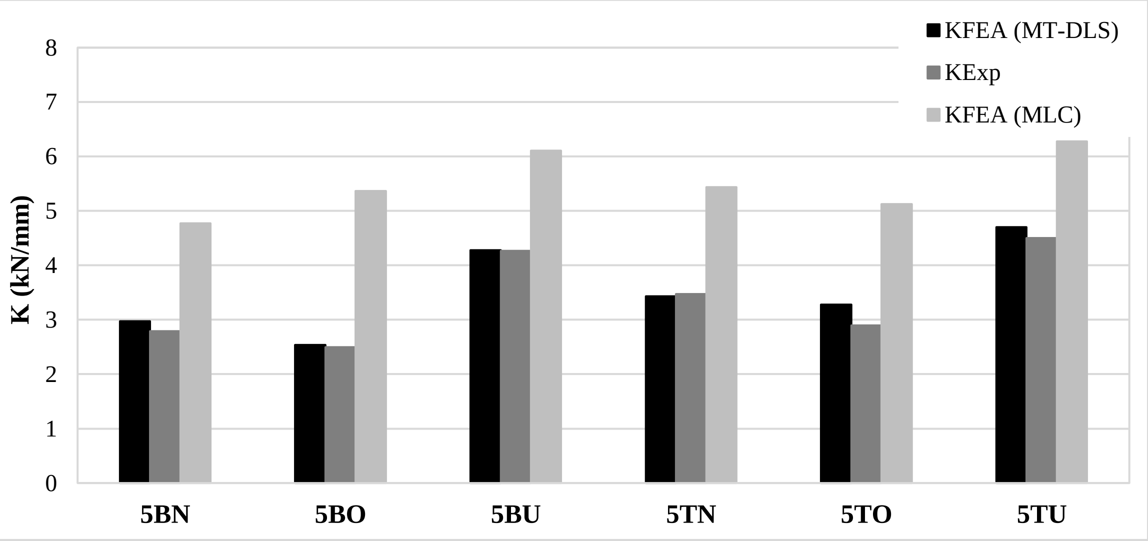

Figure 6-12 AVC5 core MT-DLS and MLC material models. FEA-derived stiffness (K_{FEA}) plotted against experimentally determined stiffness (K_{EXP}).

Figure 6-11 and Figure 6-12 compare the computed stiffness of the two material models against the experimental values for the cores created using RMS4 and RMS5, respectively. Table 6-7 and Figure 6-13 show morphometric and mechanical testing data from the AVBs using the MT-DLS material model.

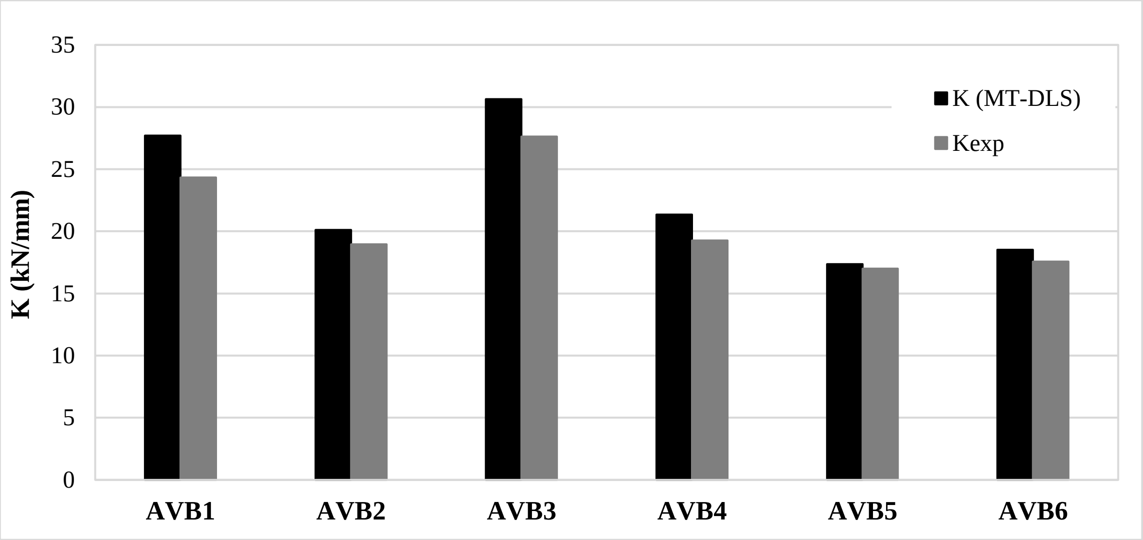

Figure 6-13 Artificial vertebral bodies. FEA-derived stiffness (K_{FEA}) plotted against experimentally determined stiffness (K_{EXP}).

The average stiffness varied by 7.46% compared to the experimental data (under-prediction).

Table 6-7 Artificial vertebral body morphometric data and experimental results. BV/TV = bone volume divided by the total volume. K = stiffness. Exp = experimental value. MT-DLS is a material model.

Body	mass (g)	BV/TV	V (mm^3)	Rho(Homo)	K_{EXP}	$K_{(MT-DLS)}$
AVB1	5.94	0.83	6.67E+03	8.91E-10	24.35	29.70
AVB2	3.28	0.74	3.94E+03	8.34E-10	18.95	30.11
AVB3	3.05	0.85	3.13E+03	9.72E-10	27.62	34.65
AVB4	3.97	0.82	4.30E+03	9.21E-10	19.23	23.34

AVB5	3.25	0.83	3.62E+03	8.97E-10	17.00	17.37
AVB6	4.14	0.85	4.61E+03	8.98E-10	17.56	18.53

The MT-DLS material model agreed well with the experimental dataset, providing confidence to then test the material model further on the AMS. No further tests were conducted with the MLC model due to its relative inaccuracy compared to the MT-DLS model.

The reaction forces recorded for the AMS analogue are compared to the corresponding FEA model tested using the MT-DLC material model in Figure 6-14.

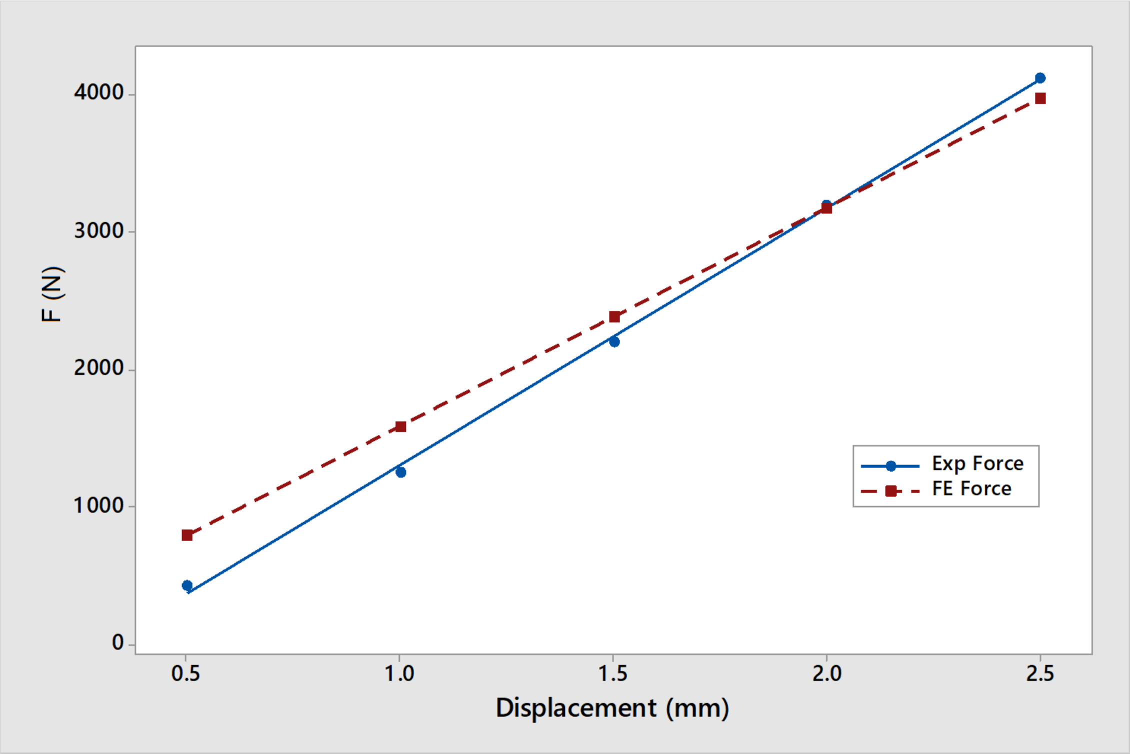

Figure 6-14 Motion segment stiffnesses. Comparison of experimental and computational techniques.

The AMS stiffness results also showed good agreement between the experimental and *in silico* data, with stiffness values of 1866.5 N/mm and 1588.2 N/mm respectively.

This is a variance of 14.9%, with a better agreement within the range 1.5–2.5 mm, reflecting the likelihood that stiffness is dependent on geometry.

The IVD properties played a greater role in determining the overall stiffness response of the motion segment than expected, both for cadaveric and analogue samples, as suggested in earlier reports (Zander, et al., 2017). This is because vertebral bodies are orders of magnitude stiffer than the IVDs and associated soft-tissue ligaments, leading the IVDs to deform more readily and fail earlier under compressive loading than the vertebral bodies. This is an important finding and highlights a greater need for accurate IVD and soft tissue replication in analogues and the models based on them. When generating the AMS finite element model, the IVD and facet ligaments were created using the faded disc boundary, which may have overestimated or underestimated the motion segment stiffness depending on how the soft tissue was reconstructed, leading to the differences in the observed stiffness. Overall, the results of this study indicate good agreement between the physical and *in silico* model, confirming that it is possible to transform real-time musculoskeletal data into both physical and *in silico* analogues, offering a range of opportunities for scientists, practitioners and manufacturers in terms of implant design and applications.

6.5 Conclusions

We have shown that it is possible to produce biofidelic spine motion segments in both analogue and digital (*in silico*) forms. There is still some distance to cover with regards to modelling spinal motion segments, and in particular actual cadaveric discs. The scanning equipment in this study was used at a higher resolution than current clinical CT scans, and to achieve this resolution in practice would require the exposure of patients to much higher levels of radiation than currently advisable. There is promising new research into CT dose reduction, which theoretically allows the retrieval of much higher spatial resolutions *in vivo* without harm to patients (Kitchen, et al., 2017).

The lack of a clear framework for validation, verification and sensitivity analysis (Jones & Wilcox, 2008) make the case for further studies into the definition of accurate replicas in conjunction with finite element models, paying special attention to the segmentation of soft tissues in the spine because this has a substantial effect on the biomechanical response of the analogues. The creation of an accurate analogue means that tests involving many different procedures and devices will become more compatible and feasible due to the lack of intra-specimen variability and biohazard risks, thus making rapid prototyping an attractive alternative for *in vitro* spine biomechanical testing. For cases where the biomechanical response of the spine is of paramount importance, the synthetic spine and associated methods tested here have proven reliable under compressive loading.

6.6 Acknowledgements

We acknowledge the work, skill and expertise provided by Karl Norris in the mechanical workshop at Cranfield University. Ethical approval was granted by the Cranfield University Research and Ethics Committee (CURES). This paper is dedicated to Dr Mike Gibson, whose untimely death is a great loss to us all.

6.7 References

Adams, G. J., 2017. *Quality Factors at the Material and Structural Level that affect the Toughness of Human Cancellous Bone,* Cranfield, Bedfordshire: Cranfield University.

Barr, J. R., Wang, T., Pelletire, M. H. & Walsh, W. R., 2014. *Initial Experience with Synthetic Spinal Motion Segments: Biomechanical.* s.l., Orthopaedic Research Society.

Burghardt, A. J., Link, T. M. & Majumdar, S., 2011. High-resolution computed tomography for clinical imaging of bone microarchitecture. *Clinical orthopaedics and related research,* 469(8), pp. 2179-2193.

Campbell, J., Imsdahl, S. & Ching, R., 2010. *Evaluation of a synthetic L2-L5 spine model for biomechanical testing.* New Orleans, Orthopaedic Research Society.

Doube, M. et al., 2010. BoneJ: Free and extensible bone image analysis in ImageJ. *Bone,* 47(6), pp. 1076-1079.

Dreisharf, M. et al., 2014. Comparison of eight published static finite element models of the intact lumbar spine: predictive power of models improves when combined together. *Journal of Biomechanics,* 47(8), pp. 1757-1766.

Franceskides, C. et al., 2017. *3D printing, the future of cost effective biomechanical testing.* Zeist, The Nederlands, SAFE EUROPE.

Franceskides, C. et al., 2018. *Spinal motion segments: Concept for a subject specific analogue model,* Shrivenham: Cranfield Defence and Security.

Franceskides, C. et al., 2018. *Spinal motion segments: Tuning and optimisation towards a biofidelic result,* Shrivenham: Cranfield Defence and Security.

Grassi, L. et al., 2013. Experimental validation of finite element model for proximal composite femur using optical measurements. *Journal of the Mechanical Behaviour of Biomedical Materials,* Volume 21, pp. 86-94.

Hambli, R., 2013. Micro-CT finite element model and experimental validation of trabecular bone damage and fracture. *Bone,* 56(2), pp. 363-374.

Helgason, B. et al., 2016. The influence of the modulus-density relationship and the material mapping method on the simulated mechanical response of the proximal femur in side-ways fall loading configuration. *Medical Engineering & Physics,* 38(7), pp. 679-689.

Jones, A. C. & Wilcox, R. K., 2008. Finite element analysis of the spine: Towards a framework of verification, validation and sensitivity analysis. *Medical Engineering & Physics,* 30(10), pp. 1287-1304.

Keaveney, T. M. & Hayes, W. C., 1993. A 20-year perspective on the mechanical properties of trabecular bone. *Journal of Biomechanical Engineering,* 115(4b), pp. 534-542.

Kitchen, M. et al., 2017. CT dose reduction factors in the thousands using X-ray phase contrast. *Nature Scientific Reports,* 7(15953).

Kuo, C. S. et al., 2010. Biomechanical analysis of the lumbar spine on facet joint force and intradiscal pressure--a finite element study. *BMC Musculoskeletal Disorders,* Volume 11, pp. 151-163.

Laffosse, J. M. et al., 2010. Micro-computed tomography evaluation of vertebral end-plate trabecular bone changes in a porcine asymmetric vertebral tether. *Journal of orthopaedic research: official publication of the Orthopaedic Research Society,* 28(2), pp. 232-240.

Lee, C. et al., 2017. Development and validation of a subject-specific finite element model of the functional spinal unit to predict vertebral strength. *Proceedings of the Institution of Mechanical Engineers. Part H, Journal of engineering in medicine,* Volume 231, pp. 821-830.

McDonald, K., Little, J., Pearcy, M. & Adam, C., 2010. Development of a multi-scale finite element model of the osteoporotic lumbar vertebral body for the investigation of apparent level vertebra mechanics and micro-level trabecular mechanics. *Medical Engineering & Physics,* 32(6), pp. 653-661.

Rodríguez, J. F., Thomas, J. P. & Renaud, J. E., 2001. Mechanical behaviour of acrylonitrile butadiene styrene (ABS) fused deposition materials. Experimental investigation. *Rapid Prototyping,* 7(3), pp. 148-158.

Schneider, C., Rasband, W. & Eliceiri, K., 2012. NIH Image to ImageJ: 25 years of image analysis. *Nature Methods,* 9(5), pp. 671-675.

Zander, T. et al., 2017. Impact of material and morphological parameters on the mechanical response of the lumbar spine - A finite element sensitivity study. *Journal of Biomechanics*, 28(53), pp. 185-190.

Zapata-Cornelio, F. Y. et al., 2017. Methodology to Produce Specimen-Specific Models of Vertebrae: Application to Different Species. *Annals of Biomedical Engineering,* 45(10), pp. 2451-2460.

7 OVERALL DISCUSSION

The overall aim of the research described in this thesis was to assess the feasibility of creating a patient-specific spinal motion segment analogue with a quick turnaround and an inexpensive manufacturing process, while achieving both anatomical and biomechanical accuracy under uniaxial compression. In addition, the analogue was compared to its computational model counterpart in an effort to provide another level of validation. We also considered the suitability of 3D printing as a manufacturing method and DIC as a data acquisition technique. Key elements drawn from the various papers presented in this thesis are discussed below.

7.1.1 Pre-CT

De-fleshing of all samples was preferred because it made the soft tissue borders of the motion segments more prominent given that the IVD and associated ligaments are not well-visualised by CT due to the much higher GS contrast of the bone. Scalpels have been used in several studies (Leeper, 2015), and this was an effective method for de-fleshing the motion segments, whereas for VB-only samples, a hot bath proved equally effective, but much faster because more than one sample could be treated at the same time. Excessive heating of two samples affected their overall strength when compared to other vertebrae from the same spine. These findings are in line with previous reports (Roberts, et al., 2002). Freeze-thaw cycles can also potentially affect the mechanical response of the samples (Wilke, et al., 1998).

7.1.2 Post-CT and pre-printing

The accuracy of the analogue (both anatomically and mechanically) depends on post-CT processing. Throughout the research described herein, close attention was paid to the most widely reported thresholding techniques. The midpoint between the background and bone peaks in the histogram was used in all cases. However, the choice of threshold can vary from user to user, and it can result in differences that are larger than the experimental differences themselves [(Campbell & Sophocleous, 2014), (Dufresne, 1998)]. Another aspect considered was the scanning of samples in a relatively short time window, as this may cause variations: in particular, shading correction can have significant effect on the final scanning output (Marchant, et al., 2008).

7.1.3 CT to 3D printing

During the manufacturing process, software glitches and bugs were detected, especially when preparing the toolpaths for higher-resolution prints. Altering the printing resolution (and thus analogue fidelity) and the removal of unnecessary complexity (such as voids, islands and structures that could not be physically printed), made the handling of the files smoother. This was attributed to several factors, including the software being outdated, inter-software handling (from ScanIp to Catalyst EX) or even simply the ability to handle large datasets.

Prior to manufacturing, and due to the conflicting literature relating to the compressive properties of 3D printed components [(Cantrell, et al., 2016), (Zou, et al., 2016)], we investigated the factors contributing to variable performance. Therefore, all samples were printed with the same layer orientation. Other sources of variance could include the printing nozzle diameter, rate of feed, and deposition temperature. All these factors would affect the coherence, shape and fill resolutions.

Some FDM printers use supports, including the printer used during this research project. We therefore considered the effects of the support on the mechanical responses of the analogue but did not observe any adverse effects.

The BV/TV ratio of the ABS analogue needed to be almost four times higher than that of the cadaveric samples in order to achieve similar mechanical properties (inverse ratio compared to the elastic modulus). This was achieved by increasing the density of internal structures within the VBs.

7.1.4 Digital image correlation

As several studies before have proven, DIC offers an accurate method to obtain full-field strain and displacement data under non-contact conditions (Palanca, et al., 2017). Other studies have gone as far as validating commercial patient-specific implants using FEA models confirmed by DIC analysis (Sutradhar, et al., 2014).

The ABS-printed specimens were coated with high-contrast white media, which is not possible with cadaveric specimens due to the potential for interactions between the paint and soft tissues. Instead, a speckle pattern was applied directly to the cadaveric material as previously recommended (Palanca, et al., 2017).

The major factors causing variability in the computed strains and displacements were the computational-facet size and point distance, as previously reported (Amiot, et al., 2013). Furthermore, we tested different point distance to computational-facet size ratios, and the most accurate strain calculations were obtained using the manufacturer's recommended ratio.

Some data could not be analysed due to the major deformation of the IVD, which resulted in the delamination of the contrast media. This was only observed in the final recorded images.

Dead weights revealed no evidence of pseudo-strains, given enough time for the sample to reach equilibrium. The DIC data were validated by testing a PVC core using a clip-on strain gauge.

7.1.5 IVD simulant

The most important variable defining the response of the motion segment was the nature of the IVD simulant, which contributed most of the variance between the real motion segment and the ABS analogue. Two different rubber compositions were tested differing solely in their Shore A hardness values. The better biofidelic response was achieved by the stiffer mixture, with a Shore A hardness of 85. The effects of voids formed during the moulding process could not be quantified.

7.1.6 Facet ligament effects in loading

We found that facet joints must be connected in the ABS analogues to achieve a response that more closely resembles that of the biological samples. The same rubber compositions described above were compared, and again the superior material was achieved by the stiffer material with a Shore A hardness of 85.

One limitation we observed was that the ABS analogue deformed to a greater extent than the cadaveric sample, especially near to the facet joints. Although no bursting or edge delamination was observed on the facet joint, we cannot rule out the possibility of contact between the superior and inferior facets.

7.1.7 Tuning techniques and effects

A number of tests were conducted to determine the lowest satisfactory scanning resolution, the best thresholding techniques and the most accurate data acquisition method.

As mentioned above, DIC has consistently provided good data as long as the speckle pattern, point distance to computational-facet size ratio, lighting contrast and lens configuration are optimised. From our data, we confidently deduce that for this methodology to provide an acceptable analogue, high-resolution scans are necessary. Furthermore, re-sampling from a higher to a lower resolution scan provides much better results than scanning directly at a lower resolution. This is most likely because of the averaging algorithms used in ScanIP when merging voxels and their associated GS values.

7.1.8 Analogue performance

As mentioned above, the performance of the motion segment analogue is highly dependent on the presence of facet joints and the correct selection of IVD simulant. The data revealed good agreement both in terms of overall stiffness and individual component displacements and strains. Furthermore, the methodology described in this thesis is clearly able to detect changes in sample morphology. This was observed for the two samples that were left in the de-fleshing bath for a prolonged time, which may have introduced nano-scale variations as previously suggested (Roberts 2002).

7.1.9 Multiscale approach to FEA modelling

Our results highlighted that a bottom-up approach to multiscale modelling is preferable, especially when the internal structure of the VB is intricately detailed. In addition, the greater the number of data points used to create the material model, the closer the performance of the computed model matches that of the physical model. When an anisotropic material such as bone is replicated by 3D printing, the dataset used for the material model must follow similar if not identical tendencies in terms of material directionality.

CONCLUSIONS

We have undertaken a series of experimental and numerical studies which have facilitated the development of an accurate vertebral body and motion segment analogue based on CT scans of biological specimens.

The conclusions to the work described in this thesis are summarised below in relation to the three objectives defined in the introductory chapter.

Objective 1: Investigate and conduct mechanical testing and data acquisition by DIC on single-component 3D-printed samples derived from CT data (Chapters 1, 3 and 4)

We confidently conclude that:

- The methodology outlined in Chapters 2, 4 and 5 produced accurate and effective test-ready components from CT scan data.
- The methods we used produced a simple analogue within the elastic regions for quasi-static axial compressive loading with less apparent variability between samples than the cadaveric originals, thus improving our ability to build accurate patient-specific models for biomechanical testing.
- Successful testing in both dynamic and quasi-static states was conducted with no adverse effects.
- DIC data acquisition was successful, with only minor errors due to the high-contrast coating causing delamination in some of the samples.
- DIC analysis achieved accurate mapping of strain propagation and highlighted areas of strain concentration.
- DIC data errors were strongly dependent on the equipment settings.
- The manufacturing capability and biofidelity of both the anatomical and biomechanical aspects of the analogues were highly dependent on the scanning resolution, the thresholding techniques, the capabilities of the 3D printer, and post-scanning data processing.

Objective 2: Develop multicomponent 3D-printed analogues derived from CT data, validated by DIC and compressive mechanical testing (Chapters 3 and 4).

- The overall response of the analogue agreed well with the biological counterpart if broken down to its constituent parts.
- The VB performed better than the IVD.
- Much of the loading and displacement was absorbed by the IVD, in agreement with previous results (Fagan, et al., 2002).
- The IVD was much more compliant than the VB, but did not conform to the anticipated values of stiffness and load dissipation.
- From the different consistencies of rubber compounds tested, a Shore A hardness of 85 was found to be the most suitable material.
- Facet joints must be present to achieve a more realistic response when using the methods we developed.
- The IVD is more difficult to manufacture than the VB due to the specific cast required for each sample as well as the individual height spacers. This reduces the ease of fabrication, but 3D printers capable of multi-material printing could overcome this limitation.

Objective 3: Develop an FEA model validated against mechanical tests on single and multi-component 3D printed analogues derived from patient CT data (Chapters 2 and 5)

- Computer models depend heavily on the inputs selected by the operator.
- Results obtained from the single-component FEA, and the comparison of DIC and FEA testing methods, indicated strong agreement between the two approaches.
- The maximum stress concentration areas identified by FEA correlated with their mechanical counterparts. Similar trends between the two methods were also observed when looking at the displacement data.
- The multiscale study confirmed that it is possible to produce biofidelic spine motion segments as both physical analogues and digital (*in silico*) models. However, there is still some distance to cover with regards to modelling spinal motion segments and cadaveric IVDs.

- The greatest limitation was the high-resolution of scanning required. Recent research suggests that CT dose-reduction may be possible, which would allow our FEA models to achieve the *in vivo* spatial resolutions required for accurate performance testing without exposing patients to high levels of radiation during data collection (Kitchen, et al., 2017).

Although these conclusions are based solely on patient-specific results, the data and derived models can be used as the basis for further research into the effect of invasive surgery, not only in the context of the skull and the spine but also on the rest of the musculoskeletal system. More interdisciplinary research is needed to benefit from the considerable synergies offered by classical biomechanics and computer modelling.

We currently lack a clear framework for model verification, validation, and sensitivity analysis (Jones & Wilcox, 2008). These issues should be addressed paying attention to the soft tissues in the spine because these have a substantial effect on the biomechanical response of the analogues.

We have come a long way towards developing a patient-specific model, taking into account the progress required to move from the early research on this topic (Fagan, et al., 2002) to where we currently stand [(Xu, et al., 2016), (Lee, et al., 2017)]. It is only a matter of time before computational models will surpass any imaginable capability of mechanical models, but until then more work is required to bridge the gap between these two disciplines.

The findings reported in this thesis lead us to the overall conclusion that, as computational and manufacturing capabilities increase, patient-specific models and their corresponding analogues will soon be within reach and could eventually find their place in the clinic.

FUTURE WORK

This research has identified further potential areas of study which are listed below:

- More research is required in the field of compound CT-MRI data, because the softer, less grey scale intense tissue and its associated boundaries are difficult to define. This would facilitate the identification of joints and ligaments.
- More work is required to understand the effect the ligaments surrounding the motion segments, and to develop suitable manufacturing, attachment and testing methods. This will help to increase the accuracy of analogues.
- A greater effort is required to determine the lowest scanning resolution that can still produce accurate analogues, and the optimal post-scanning data processing methods. This will ensure that patients are exposed to the minimum amount of radiation and that the models can be readily deployed in the clinic.
- An element-coarsening procedure should be applied to determine the coarsest compatible mesh setting, to help reduce computation times.
- The multi-material printing capabilities of advanced 3D printers should be exploited to create more sophisticated analogues.
- The methods described herein should be applied to more complex loading scenarios as well as larger structures or even assemblies, such as coupled motion segments.

Should some or all of these recommendations for future work be carried out and be deemed successful, patient-specific 3D printed analogues will be much easier to manufacture and will become more accessible. This would allow earlier preventative measures, and would facilitate surgical interventions and enhance our understanding of the corresponding effects. The manufacture of tailored prosthetics would also become more economical, helping to enhance the post-surgery quality of life for more patients.

REFERENCES

Analysis & Design Phoenix Technologies, 2010. SCA User Manual, Rev1a., Tempe, USA: PADT, Inc.

Abitpol, J.-J., 2018. Kyphoplasty, Vertebroplasty, Vertebral Augmentation Implant: Treatments for Spinal Compression Fractures, Montclair, NJ, USA: Spine Universe.

Adams, G. J., 2017. Quality Factors at the Material and Structural Level that affect the Toughness of Human Cancellous Bone, Cranfield, Bedfordshire: Cranfield University.

Adams, M., 2004. Biomechanics of back pain. Acupuncture in Medicine, 22(4), p. 178.

Amiot, F. et al., 2013. Assessment of digital image correlation measurement accuracy in the ultimate error regime: main results of a collaborative benchmark. Strain, 49(6), pp. 483-496.

Anderson, A. L. et al., 2009. The effect of posterior thoracic spine anatomical structures on motion segment flexion stiffness. Spine, 34(5), pp. 441-446.

Asgharpour, Z. et al., 2014. The validation and application of a finite element human head model for frontal skull fracture analysis. Journal of the mechanical behavior of biomedical materials, Volume 33, pp. 16-23.

ASTM, 2015. Standard Test Methods for Spinal Implant Constructs in a Vertebrectomy Model, West Conshohocken (PA, USA): ASTM International.

Barr, J. R., Wang, T., Pelletire, M. H. & Walsh, W. R., 2014. Initial Experience with Synthetic Spinal Motion Segments: Biomechanical. s.l., Orthopaedic Research Society.

Benjamin, D. J., 2014. The efficacy of surgical treatment of cancer – 20 years later. Medical Hypotheses, 82(4), pp. 412-420.

Bevill, G. & Keaveny, T., 2009. Trabecular bone strength predictions using finite element analysis of micro-scale images at limited spatial resolution. Bone, 44(4), pp. 579-584.

Boruah, S. et al., 2013. Response of Human Skull Bone to Dynamic Compressive Loading. Gothenburg (Sweden), IRCOBI.

Boruah, S. et al., 2017. Influence of bone microstructure on the mechanical properties of skull cortical bone – A combined experimental and computational approach. Journal of the Mechanical Behaviour of Biomedical Materials, Volume 65, pp. 688-704.

Buckens, C. F., de Jong, P. A., Mali, W. P. & Verhaar, H. J., 2014. Prevalent vertebral fractures on chest CT: higher risk for future hip fracture. Journal of bone and mineral research, 29(2), pp. 392-398.

Burghardt, A. J., Link, T. M. & Majumdar, S., 2011. High-resolution computed tomography for clinical imaging of bone microarchitecture. Clinical orthopaedics and related research, 469(8), pp. 2179-2193.

Busscher, I. et al., 2010. In Vitro Biomechanical Characteristics of the Spine: A Comparison Between Human and Porcine Spinal Segments. Spine, 35(2), pp. 35-42.

Camisa, W., Leasure, J. & Buckley, J., 2014. Biomechanical Validation of a Synthetic Lumbar Spine. The Spine Journal, 14(11), pp. 129-130.

Campbell, G. M. & Sophocleous, A., 2014. Quantitative analysis of bone and soft tissue by micro-computed tomography: applications to ex vivo and in vivo studies. International Bone and Mineral Society, Volume 3, p. 564.

Campbell, J., Imsdahl, S. & Ching, R., 2010. Evaluation of a synthetic L2-L5 spine model for biomechanical testing. New Orleans, Orthopaedic Research Society.

Cantrell, J. et al., 2016. Experimental Characterization of the Mechanical Properties of 3D-Printed ABS and Polycarbonate Parts. Advancement of Optical Methods in Experimental Mechanics, Volume 3, pp. 89-105.

Clark, C., Morgan, C., Sonstegard, D. & Matthews, L., 1977. The effect of biopsy-hole shape and size on bone strength. The Journal of Bone & Joint Surgery, 59(2), pp. 213-217.

Costi, J., Hearn, T. & Fazzalari, N., 2002. The effect of hydration on the stiffness of intervertebral discs in an ovine model. Clinical Biomechanics, 17(6), pp. 446-455.

Croft, P. et al., 1993. The prevalence of chronic widespread pain in the general population. The Journal of Rheumatology, 20(4), pp. 710-713.

Currey, J. D., 2002. Bones: Structure and Mechanics. 2006 ed. Woodstock, UK: Princeton University Press.

Dath, R., Ebinesan, A. D., Porter, K. M. & Miles, A. W., 2007. Anatomical measurements of porcine lumbar vertebrae. Clinical Biomechanics, Volume 22, pp. 607-613.

Dehn, T. & Boeree, N., 2007. Degenerative Disc Disease: Disc Replacement. Annals of The Royal College of Surgeons of England, 89(1), p. 6.

Deyo, R. A. & Weinstein, J. N., 2001. Low Back Pain. The New England Journal of Medicine, 344(5), pp. 363-370.

Domann, J. et al., 2011. The Analogue Spine Model: The First Anatomically and Mechanically Correct Synthetic Physical Model of the Lumbar Spine. The Spine Journal, 11(10), pp. 155-156.

Domann, J. P., 2011. Development and Validation of an Analogue Lumbar Spine Model and its Integral Components, Kansas: University of Kansas.

Domann, J. P., 2011. Development and Validation of an Analogue Lumbar Spine Model and its Integral Components, Lawrence, KS, US: University of Kansas.

Doube, M. et al., 2010. BoneJ: Free and extensible bone image analysis in ImageJ. Bone, 47(6), pp. 1076-1079.

Dreisharf, M. et al., 2014. Comparison of eight published static finite element models of the intact lumbar spine: predictive power of models improves when combined together. Journal of Biomechanics, 47(8), pp. 1757-1766.

Dufresne, T., 1998. Segmentation techniques for analysis of bone by three-dimensional computed tomographic imaging. Technol Health Care, 6(5), pp. 351-359.

Eidelson, S. G., 2018. Laminotomy versus Laminectomy, Montclair, NJ. USA: Spine Universe.

Ensign, W. et al., 2000. A survey of self-reported injuries among special boat operatiors, San Diego, CA, USA: Naval Health Research Center.

Errani, C. et al., 2013. Current Concepts in the Biopsy of Musculoskeletal Tumours. The Scientific World Journal, Volume 2013, p. 7.

Fagan, M., Julian, S., Siddall, D. & Mohsen, A. M., 2002. Patient-specific spine models. Part 1: Finite element analysis of the lumbar intervertebral disc - A material sensitivity study. Proceedings of the Institution of Mechanical Engineers Part H Journal of Engineering in Medicine, Volume 216, pp. 299-314.

Falland-Cheung, L. et al., 2017. Investigation of the elastic modulus, tensile and flexural strength of five skull simulant materials for impact testing of a forensic skin/skull/brain model. Journal of the Mechanical Behaviour of Biomedical Materials, Volume 68, pp. 303-307.

Ferguson, S. & Steffen, T., 2003. Biomechanics of the aging spine. European Spine Journal, 12(2), pp. 97-103.

Franceskides, C., 2017. 3D Printing - The future of cost effective biomechanical testing. Zeist, The Netherlands, SAFE EUROPE.

Franceskides, C. et al., 2017. 3D printing, the future of cost effective biomechanical testing. Zeist, The Netherlands, SAFE EUROPE.

Franceskides, C. et al., 2018. Spinal motion segments: Concept for a subject specific analogue model, Shrivenham: Cranfield Defence and Security.

Franceskides, C. et al., 2018. Spinal motion segments: Tuning and optimisation towards a biofidelic result, Shrivenham: Cranfield Defence and Security.

Franceskides, C. et al., 2017. Impact of lesion excision on 3D printed human skull. Materials Today COMMS.

Franceskides, C. et al., 2016. Evaluation of bone excision on occipital area of simulated human skull. Lyon, European Society of Biomechanics.

Friss, E. A., Pence, D. C., Graber, C. D. & Montoya, J. A., 2003. Mechanical Analogue Model of the Human Lumbar Spine: Development and Evaluation. In: M. N. Melkerson, S. L. Griffith & J. S. Kirkpatric, eds. Spinal implants: are we evaluating them appropriately?. STP1431 ed. West Conshohocken: ASTM International, p. 236.

Gallagher, K. M., Howarth, S. J. & Callaghan, J. P., 2010. Effects of anterior shear displacement rate on the structural properties of the porcine cervical spine. Journal of Biomechanical Engineering, Volume 132, pp. 1149-1154.

Galloway, A., 1999. Broken bones, anthropological analysis of blunt force trauma. s.l.:Charles C Thomas.

Garcia-Gonzalez, D. et al., 2017. On the mechanical behaviour of PEEK and HA cranial implants under impact loading. Journal of the Mechanical Behaviour of Biomedical Materials, Volume 69, pp. 342-354.

Gefen, A. & Epstein, Y., 2014. The Mechanobiology and Mechanophysiology of Military-Related Injuries. 1 ed. s.l.:Springer.

Gerace, L. et al., 1994. Skeletal differences between black and white men and their relevance to body composition estimates. American Journal of Human Biology, 6(2), pp. 255-262.

Gibson, M., Franceskides, C. & Zioupos, P., 2016. Simulated Impact Response of a 3-D Printed Skull, with an Ellipsoidal Excision, using Finite Element Analysis. Lyon, European Society of Biomechanics.

GOM mbH, 2018. Gom-Correlate. [Online] Available at: https://www.gom-correlate.com/en/support.php[Accessed 2018].

Grassi, L. et al., 2013. Experimental validation of finite element model for proximal composite femur using optical measurements. Journal of the Mechanical Behaviour of Biomedical Materials, Volume 21, pp. 86-94.

Hambli, R., 2013. Micro-CT finite element model and experimental validation of trabecular bone damage and fracture. Bone, 56(2), pp. 363-374.

Hangai, M. et al., 2008. Factors associated with lumbar intervertebral disc degeneration in the elderly. The Spine Journal, 8(5), pp. 732-740.

Harrington, B., 2014. Study of human head simulant's dynamic response to blast wave, s.l.: Cranfield University, Defence Academy.

Helgason, B. et al., 2016. The influence of the modulus-density relationship and the material mapping method on the simulated mechanical response of the proximal femur in side-ways fall loading configuration. Medical Engineering & Physics, 38(7), pp. 679-689.

Hisley, D., Gurganus, J. & Drysdale, A., 2010. Experimental Methodology using Digital Image Correlation to Assess Ballistic Helmet Blunt Trauma. Journal of Applied Mechanics, Volume 78.

Holsgrove, T. P., Harinderjit, S. G., Miles, A. W. & Ghenduzzi, S., 2015. The dynamic, six-axis stiffness matrix testing of porcine spinal specimens. The Spine Journal, 15(1), pp. 176-184.

Hongo, M. et al., 2008. Effect of multiple freeze-thaw cycles on intervertebral dynamic motion characteristics in the porcine lumbar spine. Journal of Biomechanics, 41(4), pp. 916-920.

Howarth, S. J., 2011. Mechanical response of the porcine cervical spine to acute and repetitive anterior-posterior shear, Waterloo, Ontario: University of Waterloo.

Inglis, S., 2016. 3D Printing in the NHS and healthcare sciences. IPEM SCOPE - ISSN 0964-9565, 25(4), pp. 10-13.

International Organization for Standardization, 1997. Mechanical vibration and shock -- Evaluation of human exposure to whole-body vibration -- Part 1: General requirements, Geneva: International Organization for Standardization.

Jaumard, N. V., Welch, W. C. & Winkelstein, B. A., 2011. Spinal Facet Joint Biomechanics and Mechanotransduction in Normal, Injury and Degenerative Conditions. Journal of Biomechanical Engineering, 133(7), pp. 071010-071041.

Jhawar, B. S., Fuchs, C. S., Colditz, G. A. & Stampfer, M. J., 2006. Cardiovascular risk factors for physician-diagnosed lumbar disc herniation. The Spine Journal, 6(5), pp. 684-691.

Jones, A. C. & Wilcox, R. K., 2008. Finite element analysis of the spine: Towards a framework of verification, validation and sensitivity analysis. Medical Engineering & Physics, 30(10), pp. 1287-1304.

Jones, M. et al., 2017. Development and validation of a physical model to investigate the biomechanics of infant head impact. Forensic Science International, Volume 276, pp. 111-119.

Keaveney, T. M. & Hayes, W. C., 1993. A 20-year perspective on the mechanical properties of trabecular bone. Journal of Biomechanical Engineering, 115(4b), pp. 534-542.

Kitchen, M. et al., 2017. CT dose reduction factors in the thousands using X-ray phase contrast. Nature Scientific Reports, 7(15953).

Knott, L. & Bailey, A. J., 1998. Collagen cross-links in mineralizing tissues: a review of their chemistry, function and clinical relevance. Bone, 22(3), pp. 181-187.

Konstantinou, K. & Dunn, K. M., 2008. Sciatica: Review of Epidemiological Studies and Prevalence Estimates. Spine, 33(22), pp. 2464-2472.

Kuo, C. S. et al., 2010. Biomechanical analysis of the lumbar spine on facet joint force and intradiscal pressure--a finite element study. BMC Musculoskeletal Disorders, Volume 11, pp. 151-163.

Laffosse, J. M. et al., 2010. Micro-computed tomography evaluation of vertebral end-plate trabecular bone changes in a porcine asymmetric vertebral tether. Journal of orthopaedic research: official publication of the Orthopaedic Research Society, 28(2), pp. 232-240.

Landis, W. J., 1995. The strength of calcified tissue depends in part on the molecular structure and organization of its constituent mineral crystals in their organic matrix. Bone, 16(5), pp. 533-544.

Lecompte, D. et al., 2006. Quality assessment of speckle patterns for digital image correlation. Optics and Lasers in Engineering, 44(11), p. 1132–1145.

Lee, C. et al., 2017. Development and validation of a subject-specific finite element model of the functional spinal unit to predict vertebral strength. Proceedings of the Institution of Mechanical Engineers. Part H, Journal of engineering in medicine, Volume 231, pp. 821-830.

Lee, C.-H.et al., 2017. Development and validation of a subject-specific finite element model of the functional spinal unit to predict vertebral strength. Proceedings of the Institution of Mechanical Engineers, Part H, 231(9), pp. 821-830.

Leeper, B. J., 2015. Evaluation of current methods of soft tissue removal from bone, Pittsburgh, PA, USA: Kenneth P. Dietrich School of Arts and Sciences, University of Pittsburgh.

Leone, A., 2007. Lumbar intervertebral instability: A Review. Radiology, 245(1), pp. 62-77.

Lorenz, M., Patwardhan, A. & Vanderby, R., 1983. Load-bearing characteristics of lumbar facets in normal and surgically altered spinal segments. Spine, 8(2), pp. 122-130.

Lott, B. D., Reece, F. N. & Drott, J. H., 1980. Effect of Preconditioning on Bone Breaking Strength. Poultry Science, Volume 59, pp. 724-725.

Magadia, W. et al., 2016. Cancer survival in England: Patients diagnosed between 2010 and 2014 and followed up to 2015, s.l.: Office for National Statistics.

Marchant, T. E. et al., 2008. Shading correction algorithm for improvement of cone beam CT images in radiotherapy. Physics in Medicine & Biology, 53(20), pp. 5719-5733.

Marine Accident Investigation, 2009. Report on the investigation of injury to a passenger on board the RIB, Celtic Pioneer, Bristol Channel, Southampton, UK: Marine Accident Investigation Branch.

Martin, R. B. & Burr, D. B., 1989. Structure function and adaptation of compact bone. American Journal of Physical Anthropology, 82(1), pp. 116-117.

Matmatch GmbH, 2., 2018. Matmatch. [Online] Available at: https://matmatch.com/

[Accessed 2018].

Mayfield Clinic, 2018. Mayfield Certified Health Info Materials, Cincinnati, OH, USA: Mayfield Clinic.

McAfee, P. C. et al., 1988. The biomechanical and histomorphometric properties of anterior lumbar fusions: a canine model. Journal of spinal disorders, 1(2), pp. 101-110.

McDonald, K., Little, J., Pearcy, M. & Adam, C., 2010. Development of a multi-scale finite element model of the osteoporotic lumbar vertebral body for the investigation of apparent level vertebra mechanics and micro-level trabecular mechanics. Medical Engineering & Physics, 32(6), pp. 653-661.

McLain, R. F., Yerby, S. A. & Moseley, T. A., 2002. Comparative morphometry of L4 vertebrae: comparison of large animal models for the human lumbar spine. Spine, 27(8), pp. 200-206.

Michael, A., Orteu, J. & Schreier, W., 2009. Digital Image Correlation. In: Image correlationfor shape, motion and deformation measurements. Springer-Verlag: Springer, pp. 1-37.

Monea, A. G. et al., 2013. The relation between mechanical impact parameters and most frequent bicycle related head injuries. Journal of the Mechanical Behaviour of Biomedical Materials, Volume 33, pp. 3-15.

National Centre for the Replacement, Refinement and Reduction of Animas in Research, 2017. [Online] Available at: https://www.nc3rs.org.uk/the-3rs[Accessed 11 2017].

National Institutes of Health, 2017. Statistics at a Glance: The Burden of Cancer in the United States, s.l.: National Cancer Institute.

Newell, N. et al., 2017. Biomechanics of the human intervertebral disc: A review of testing techniques and results. Journal of the Mechanical Behaviour of Biomedical Materials, Volume 69, pp. 420-434.

Newman, L. V. & Williams, J. G., 1978. The Impact Behaviour of ABS Over a Range of Temperatures. Polymer engineering and science, 18(11), pp. 893-899.

NHS Digital, 2016. Hospital Episode Statistics. [Online] Available at: http://content.digital.nhs.uk/hes[Accessed 2016].

Office of Crash Worthiness Standards, 1997. www.unece.org. [Online] Available at: https://www.unece.org/fileadmin/DAM/trans/doc/2009/wp29/HIII_50th_Male_Drawings.pdf[Accessed 2016].

Özkaya, N., Nordin, M., Goldsheyder, D. & Leger, D., 2017. Fundamentals of Biomechanics - Equilibrium, Motion, and Deformation. 3rd ed. Cham, Switzerland: Springer International Publishing.

Palanca, M., Marco, M., Ruspi, M. L. & Cristofolini, L., 2017. Full-field strain distribution in multi-vertebra spine segments: An in vitro application of digital image correlation. Medical Engineering & Physics, Volume 000, pp. 1-8.

Palanca, M., Tozzi, G. & Cristofolini, L., 2015. The use of digital image correlation in the biomechanical area: a review. International Biomechanics, 3(1), pp. 1-21.

Palanca, M., Tozzi, G. & Cristofolini, L., 2016. The use of digital image correlation in the biomechanical area: a review. International Biomechanics, 3(1), pp. 1-21.

Pal, G. P. & Routal, R. V., 1987. Transmission of weight through the lower thoracic and lumbar regions of the vertebral column in man. Journal of Anatomy, Volume 152, pp. 93-105.

Pan, B., Lu, Z. & Xie, H., 2010. Mean intensity gradient: An effective global parameter for quality assessment of the speckle patterns used in digital image correlation. Optics and Lasers in Engineering, 48(4), p. 469–477.

Pinnoji, P. K. & Mahajan, P., 2007. Finite element modelling of helmeted head impact under frontal loading. Sādhanā, 32(4), pp. 445-458.

Rahmoun, J. et al., 2014. Characterization and micromechanical modelling of the human cranial bone elastic properties. Mechanics Research Communications, Volume 60, pp. 07-14.

Resnick, D. K., Weller, S. J. & Benzel, E. C., 1997. Biomechanics of the thoracolumbar spine. Neurosurgery clinics of North America, 8(4), pp. 455-469.

Rissanen, P., 1964. Comparison of pathologic changes in intervertebral discs and interspinous ligaments of the lower part of the lumbar spine in the light of autopsy findings. Acta Orthopaedica, 34(1), pp. 54-65.

Roberts, S. J., Smith, C. I., Millard, A. & Collins, M. J., 2002. The taphonomy of cooked bone: Characterising boiling and its physico-chemical effects. Archaeometry, 44(3), pp. 485-494.

Rodríguez, J. F., Thomas, J. P. & Renaud, J. E., 2001. Mechanical behaviour of acrylonitrile butadiene styrene (ABS) fused deposition materials. Experimental investigation. Rapid Prototyping, 7(3), pp. 148-158.

Sawbones, 2012. Biomechanical Spine Product Research. [Online] Available at: http://www.sawbones.com/UserFiles/Documents/Product/BioSpine_info.pdf[Accessed February 2018].

Schneider, C., Rasband, W. & Eliceiri, K., 2012. NIH Image to ImageJ: 25 years of image analysis. Nature Methods, 9(5), pp. 671-675.

Sharma, M., Langrana, N. A. & Rodriquez, J., 1995. Role fo ligaments and facets in lumbar spinal stability. Spine, 20(8), pp. 887-900.

Shirazi-Adi, A. & Drouin, G., 1987. Load-bearing role of facets in a lumbar segment under sagittal plane loadings. Journal of Biomechanics, 20(6), pp. 601-613.

Shore, A. F. & Shore, C. P., 1930. Apparatus for measuring the hardness of materials. US, Patent No. US1770045 (A) — 1930-07-08.

Siebert, T., Becker, T. & Spiltthof, K., 2007. Error Estimations in Digital Image Correlation Technique. Applied Mechanics and Materials, 7(8), pp. 265-270.

Silva, M. J., Wang, C., Keaveny, T. M. & Hayes, W. C., 1994. Direct and computed tomography thickness measurements of the human, lumbar vertebral shell and endplate. Bone, 15(4), pp. 409-414.

Smeathers, J. E. & Joanes, D. N., 1988. Dynamic compressive properties of human lumbar intervertebral joints: a comparison between fresh and thawed specimens. J Biomech, 21(5), pp. 425-433.

Smit, T. H., 2002. The use of a quadruped as an in vivo model for the study of the spine – biomechanical considerations. European Spine Journal, Volume 11, pp. 137-144.

Stratasys, 2015. ABSplus-P430. [Online] Available at:http://usglobalimages.stratasys.com/Main/Files/Material_Spec_Sheets/MSS_FDM_ABSplusP430.pdf[Accessed 06 12 2017].

Sutradhar, A., Park, J., Carrau, D. & Miller , M., 2014. Experimental validation of 3D printed patient-specific implants using digital image correlation and finite element analysis. Computers in Biology and Medicine, Volume 52, pp. 8-17.

Sutradhar, A., Park, J., Carrau, D. & Miller, M. J., 2014. Experimental validation of 3D printed patient-specific implants using digital image correlation and finite element analysis. Computers in Biology and Medicine, Volume 52, pp. 8-17.

Taimela, S., Kujala, M. U., Salminen, J. J. & Vijanen, T., 1997. The prevalence of low back pain among children and adolescents. A nationwide, cohort-based questionnaire survey in Finland. Spine, 22(10), pp. 1132-1138.

U.S. Army Medical Research Acquisition Activity, 2014. Notice for Ballistic Load Sensing Headform System. [Online] Available at: www.fbo.gov/index[Accessed 2014].

Vassolera, J. M. & Fancelloa, E. A., 2012. Error analysis of the digital image correlation method. Asociación Argentina de Mecánica Computacional, Volume XXIX, pp. 6149-6161.

Verhulp, E., Van Rietbergen, B., Müller, R. & Huiskes, R., 2008. Micro-finite element simulation of trabecular-bone post-yield behaviour – effects of material model, element size and type. Computer Methods in Biomechanics and Biomedical Engineering, 11(4), pp. 389-395.

Viquet-Carrin, S., Garnero, P. & Delmas, P. D., 2006. The role of collagen in bone strength. Osteoporosis International, 17(3), pp. 319-336.

Vogt, M. T., Hanscom, B., Lauerman, W. C. & Kang, J. D., 2002. Influence of Smoking on the Health Status of Spinal Patients. Spine, 27(3), pp. 313-319.

Wang, T., Ball, J. R., Pelletier, M. H. & Walsh, W. R., 2014. Biomechanical evaluation of a biomimetic spinal construct. Journal of Experimental Orthopaedics, 1(3).

Wang, T., Ball, J. R., Pelletier, M. H. & Walsh, W. R., 2014. Initial Experience with Synthetic Spinal Motion Segments: Biomechanical Assessment of High Cycle and Implant Performance. New Orleans (LA, USA), ORS Annual Meeting.

Wilke, H. J., Jungkunz, B., Wenger, K. & Claes, L. E., 1998. Spinal segment range of motion as a function of in vitro test conditions: effects of exposure period, accumulated cycles, angular-deformation rate, and moisture condition. The Anatomical Record, 251(1), pp. 15-19.

Wilke, H. J., Kettler, A. & Claes, L. E., 1997. Are sheep spines a valid biomechanical model for human spines?. Spine, 15(22), pp. 2365-2374.

Wilke, H. J., Krischack, S. & Claes, L. E., 1996. Formalin Fixation Strongly Influences Biomechanical Properties of the Spine. Journal of Biomechanics, 29(12), pp. 1629-1631.

Wilke, H. J., Krischak, S. T., Wenger, K. H. & Claes, L. E., 1997. Load-displacement properties of the thoracolumbar calf spine: experimental results and comparison to known human data. European Spine Journal, 6(2), pp. 129-137.

Wilke, H. J., Wenger, K. & Claes, L. E., 1998. Testing criteria for spinal implants: Recommendations for the standardization of in vitro stability testing of spinal implants. European Spina Journal, 7(2), pp. 148-154.

Xu, M., Yang, J., Lieberman, I. H. & Haddas, R., 2016. Lumbar spine finite element model for healthy subjects: development and validation. Computer Methods in Biomechanics and Biomedical Engineering, 20(1), pp. 1-15.

Yingling, V. R., Callaghan, J. P. & McGill, S. M., 1997. dynamic loading affects the mechanical properties and failure site of porcine spines. Clinical Biomechanics, Volume 12, pp. 301-305.

Zander, T. et al., 2017. Impact of material and morphological parameters on the mechanical response of the lumbar spine - A finite element sensitivity study. Journal of Biomechanics, 28(53), pp. 185-190.

Zapata-Cornelio, F. Y. et al., 2017. Methodology to Produce Specimen-Specific Models of Vertebrae: Application to Different Species. Annals of Biomedical Engineering, 45(10), pp. 2451-2460.

Zengin, A. et al., 2016. Ethnic differences in bone geometry between White, Black and South Asian men in the UK. Bone, Volume 91, pp. 180-185.

Zioupos, P., Cook, R. B. & Hutchinson, J. R., 2008. Some basic relationships between density values in cancellous and cortical bone. Journal of Biomechanics, 41(9), pp. 1961-1968.

Zioupos, P., Smith, C. & Yuehuei, A., 1999. Factors Affecting Mechanical Properties of Bone. In: A. Yuehuei & D. A. Robert, eds. Mechanical Testing of Bone and the Bone-Implant Interface. s.l.:CRC Press, pp. 65-85.

Zou, R. et al., 2016. Isotropic and anisotropic elasticity and yielding of 3D printed material. Composites Part B: Engineering, Volume 99, pp. 506-513.

APPENDICES

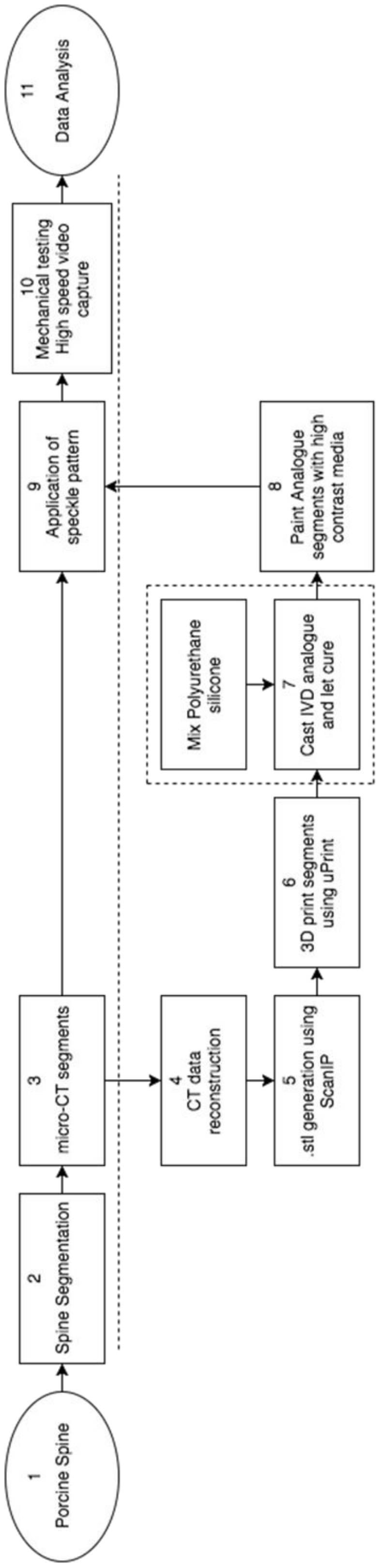
1
Porcine Spine
2
Spine Segmentation
3
micro-CT segments
4
CT data reconstruction
5
.stl generation using ScanIP
6
3D print segments using uPrint
Mix Polyurethane silicone
7
Cast IVD analogue and let cure
8
Paint Analogue segments with high contrast media
9
Application of speckle pattern
10
Mechanical testing
High speed video capture
11
Data Analysis

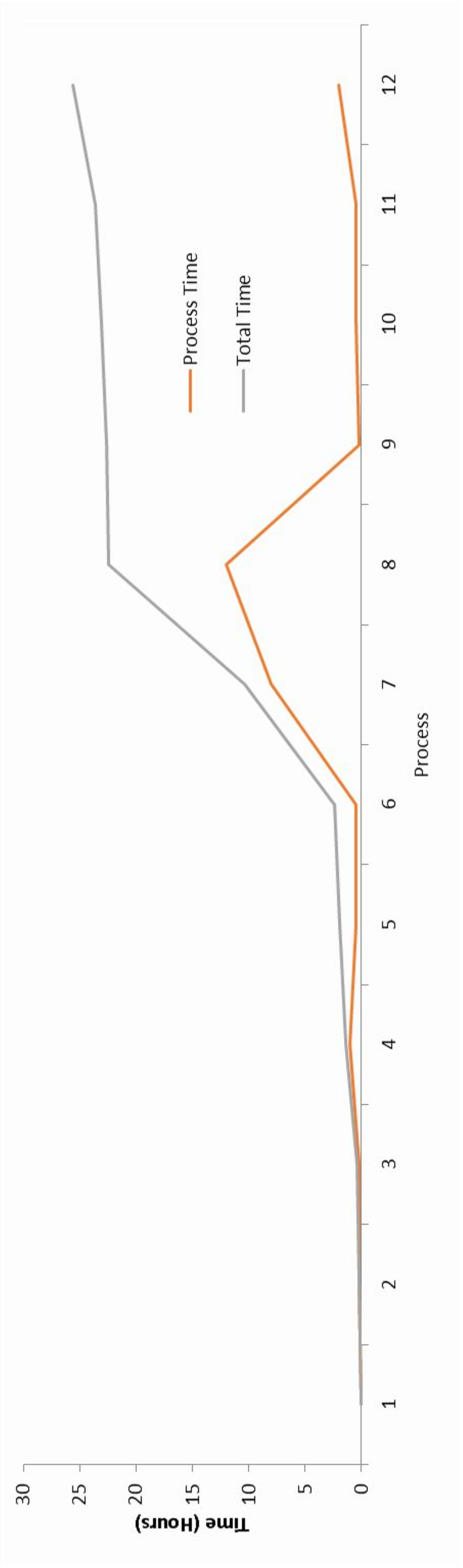
Time (Hours)
0
5
10
15
20
25
30
Process
1
2
3
4
5
6
7
8
9
10
11
12
Process Time
Total Time